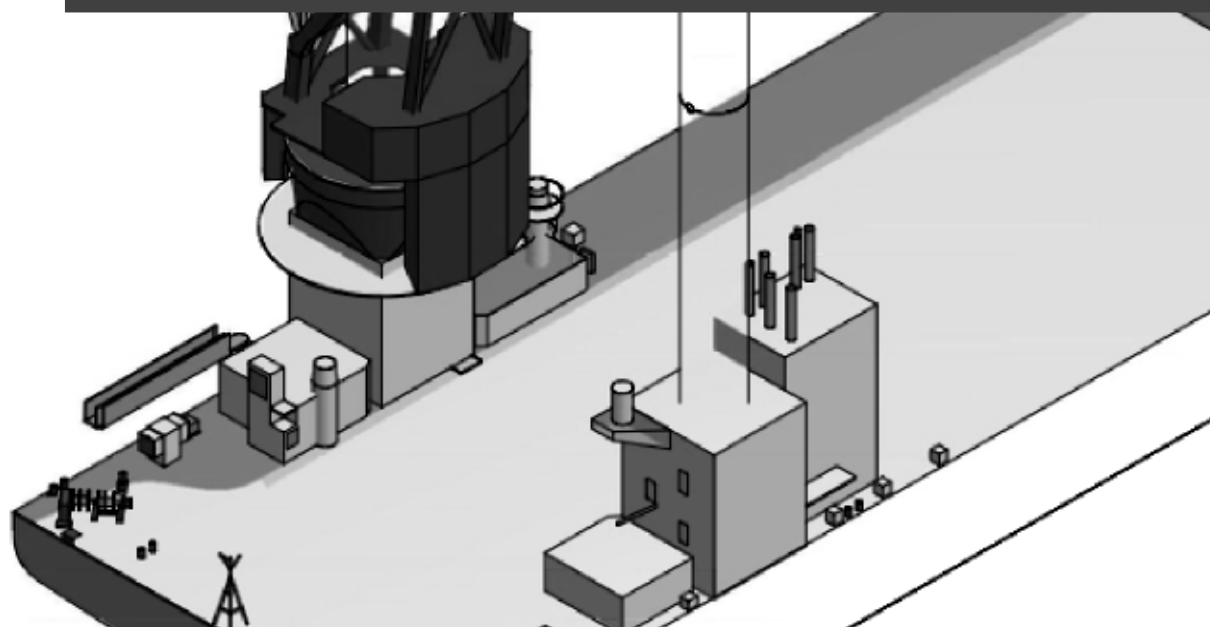


Single Blade Installation for Large Wind Turbines in Extreme Wind Conditions

A QUASI-STEADY AEROELASTIC STUDY IN HIGH WIND SPEEDS UNDER DIFFERENT INFLOW ANGLES

L. Kuijken

February 2, 2015



SIEMENS



Single Blade Installation for Large Wind Turbines in Extreme Wind Conditions

A Quasi-Steady Aeroelastic Study in High Wind Speeds under Different Inflow Angles

MASTER OF SCIENCE THESIS

For obtaining the degree of Master of Science in Engineering Wind Energy at Technical University of Denmark and in Aerospace Engineering at Delft University of Technology.

L. Kuijken

February 2, 2015

European Wind Energy Master - EWEM
DUWIND - Delft University of Technology
DTU Wind Energy - Denmark Technical University



Risø DTU



Copyright © L. Kuijken
All rights reserved.

EUROPEAN WIND ENERGY MASTER - EWEM
OF
ROTORDESIGN TRACK

The undersigned hereby certify that they have read and recommend to the European Wind Energy Master - EWEM for acceptance a thesis entitled "**Single Blade Installation for Large Wind Turbines in Extreme Wind Conditions**" by **L. Kuijken** in partial fulfillment of the requirements for the degree of **Master of Science**.

Dated: February 2, 2015

Professor:

Prof.dr. G.J.W. van Bussel of Delft University of Technology

Supervisor:

dr.ir. M. Gaunaa of Denmark Technical University

Supervisor:

dr.ir. A.H. van Zuijlen of Delft University of Technology

Supervisor:

ir. E.J. Soons of Siemens Wind Power

Summary

Energy demand from wind greatly increases, as such more remote sites need to be explored in order to find good wind resources. These remote sites are driving the industry further offshore and therefore into extreme wind and sea conditions. This push towards extreme conditions requires technological advancements concerning the wind turbine loads, power production and installation. The levelised cost of wind energy is strongly dependent on the capital expenditures and thus on the installation and logistics of erecting a wind turbine offshore. Improving the robustness of the installation to higher wind velocity and turbulence will increase the weather window and therefore drastically decrease the levelised cost of energy (LCoE). This thesis will focus on one particular technique of wind turbine installation: Horizontal Single Blade Mounting (HSBM).

HSBM is a wind turbine blade lifting technique performed by Siemens Wind Power (SWP). This technique is currently limited to low wind speeds, which contradicts the fact that the industry is targeting high wind speed offshore sites. This technical problem is the basis of the thesis study.

This thesis study will answer three research questions in order to improve future lifting methods. In a nutshell these questions are: **one**, *how to model the aerodynamic forces and dynamic behaviour of a hoisted wind turbine blade?*, **two**, *what are the critical parameters affecting the blade response?* and **three**, *how can single blade mounting be improved for higher wind speeds?*.

The *first* research question is answered with an aeroelastic model in HAWC2. The engineering basis of this model, *the crossflow principle*, is verified with a computational fluid dynamic analysis in ANSYS Fluent. Subsequently, with the aeroelastic model the *second* research question is answered by performing a transient simulation and studying three criteria. These are, the mean loading on the blade, the standard deviation of the loading and the displacement of the root. The results lead to the following key parameters affecting blade response in HSBM: wind velocity, turbulence, inflow angle, blade geometry, yoke mass and cable configuration. The *third* research questions is answered by providing recommendations based on the previously mentioned parameters. According to these three research questions the thesis study will be summarised.

1. How to model the aerodynamic forces and dynamic behaviour of a hoisted wind turbine blade in different inflow angles?

The following reasoning leads to the answer of research question one.

Computational fluid dynamics has been chosen in order to test the validity of the crossflow principle, based on several reasons. First, the crossflow is expected to fail due to three-dimensional effects of the flow over the blade. Additionally CFD is understood to be the only well-documented simulation method to model three-dimensional flow with proven accuracy. Secondly, there are simple engineering methods capable of determining the forces on a yawed wing however they are not capable of handling yaw angles above 40° and fail to model the effect of large twist and prebend in the blade. Finally, from the scientific paper of [Sørensen and Michelsen \[39\]](#) is it learned that 3D RANS CFD is an accurate way to model the drag dependency of large non-rotating wind turbine blades.

CFD computations are done in a steady-state, due to the fact that many cases need to be calculated and thus minimal computational expense is required. Therefore, comparison cannot be done with the transient aeroelastic HAWC2 model and an additional model is developed referred to as the *aerodynamic model*. The aerodynamic model will purely simulate the blade clamped in its centre of gravity with 10 [m/s] wind velocity and varying pitch and yaw angles, providing a similar situation as in the *CFD model* to ensure accurate comparison. The aerodynamic model is verified with a similar HAWC2 model by [Gaunaa et al. \[12\]](#) and a comparable GH Bladed model by [Wang et al. \[46\]](#). The model shows that the forces on the *straight blade* exactly scale with the square cosine of the yaw angle corresponding to the crossflow principle. Finally, it is assessed that the loading scales quadratically with windspeed and the standard deviation linearly with the turbulence intensity which is analytically confirmed.

Furthermore, similar to the CFD models used by [Sørensen and Michelsen \[39\]](#) and [Uranga et al. \[45\]](#) a 3D steady-state RANS CFD model with third order accurate discretisation in Fluent is developed to compare the mean forces and moments from the crossflow based HAWC2 model. Consisting of approximately 8 million hexahedral elements, a $y+$ value of 0.024 and a mesh independency study using the richardson extrapolation below 1%, the grid is considered adequate for this research purpose. The results are verified with the paper by [Wang et al. \[47\]](#) on stationary blade computations with steady CFD and the two aforementioned peer reviewed research papers. Results match to such an extent that the author is confident that the CFD model is accurate.

The comparison between the *aerodynamic model* and the *CFD model* clearly indicates deviation in the results for the lift in pitch angle 0°, rolling moment for pitch -90° and 0° and spanwise force for both pitch angles. The results for the drag force, yawing moment and pitching moment agree satisfactory, however the loading is systematically underestimated by the aerodynamic model for yaw angles of ±30° and ±40°. These discrepancies are investigated by studying the CFD streamline pattern over several airfoil sections and it is perceived that strong separation bubbles and large wakes are generated when introducing a yawed inflow. Especially in the cases for $+20 < \text{yaw} < +60$ and blade stations close to the root, the vortex structure behind the blade is remarkably larger. This indicates the presence of strong three-dimensional effects over the blade. A further investigation into the streamline pattern in chordwise and spanwise direction pointed out

that the region of negative wall shear stress, hence flow reversal, increases with larger yaw angles, however reaches a saturation point and decreases when yaw increases above 40° . This effect is caused by the growing spanwise crossflow over the blade when increasing the yaw angle leading to destabilisation of the chordwise flow and ultimately earlier transition and separation. This phenomena leads to a higher drag force for increasing yaw which is also observed and demonstrated by Uranga et al. [45]. The basis of HAWC2 lies in the computation of the force based on 2D force coefficients and limits the model to predict the rising drag force induced by earlier separation and thus leads to the underprediction of the forces.

Finally, as the limitations and accuracy of the crossflow principle and thereby the HAWC2 model are determined, the validity of the *aeroelastic model* is assessed. The error in the lift prediction of HAWC2 is neglected versus the +100 ton mass of the blade yoke combination. Furthermore, the model will only be used for sensitivity checks of several key parameters, instead of determining absolute values. The *aeroelastic model* is verified with the generalised engineering model by Gaunaa et al. [12] by comparing the cable tension in the tacklines.

2. What are the critical parameters affecting the blade response?

Following the findings with respect to research question one, the second research question will now be discussed.

In order to define the installation constraints and influencing parameters the following hoisting criteria are set: mean loading, standard deviation of the loading and displacement of the root. These criteria lead to the answer of the second research question.

It is identified that with zero yaw, the root moves into the wind and the tip out of the wind. Increasing the yaw angle towards the root, i.e. air flowing from root to tip, changes the sign of the displacement, thus the root moves out of the wind and the tip into the wind. Rotating the inflow towards the tip, i.e. air flowing from tip to root, initially increases the root displacement into the wind, however decreases when yaw increases towards 60° . Moreover, it is noted that with yawing towards the root higher fluctuating movement of the blade are observed than with yawing towards the tip. Finally, it is remarkable that for pitch -45° , strong unsteady displacement of the root arises.

The influence of the wind conditions is defined for different pitch and yaw angles. This study and other studies point out that the mean forces on the blade, and thus the standard deviation, scale quadratically with the incoming windspeed, which is similar in the *aeroelastic model*. Proceeding given this observation, learns that both the root displacement as well as the tackline forces scale quadratically with the windspeed. Furthermore, the standard deviation of the loading scales linear with the turbulence intensity and it is expected to also hold for the tackline forces. Additionally, the impact of the turbulence intensity on the displacement of the root grows to such an extent that beyond 10% turbulence the displacement of the root is completely dominated by the turbulence intensity and not the windspeed. Note that the force fluctuations caused by vortex shedding cannot be modelled by the *aeroelastic model*.

The influence of the blade orientation and geometry is evaluated. Using the CFD model, the effect of the Gurney flap is studied. This indicated that changing the blade geome-

try by adding a trailing edge device substantially increases the size of the wake in zero pitch inevitably leading to large loading on the blade and presumably also the standard deviation.

Finally, the influence of the setup of the hoisting method is investigated. Adding mass to the yoke stabilises the blade installation, since the root displacement fluctuates less with a yoke mass 77 tons, relative to the baseline 57 tons. Furthermore, raising the point where the wires split decreases the mean root displacement and fluctuation. Additionally, maximising the distance between the tacklines reduces the root displacement.

3. How can single blade mounting be improved for higher wind speeds?

Answering the final research question is done for the parameters: pitch, yoke mass and cable configuration, since these parameters can be defined in the design of the blade lifting procedure. It is recommended to avoid the blade orientation of 45° pitch, since this subjects the largest forces in the tacklines and causes chaotic displacement of the root. It is recommended to hoist the blade with 90° pitch as it is judged that installation would be most predictable in this orientation. Furthermore, it is recommended to increase the yoke mass to the point where its weight does not exceed the maximum allowable tension in the wires and maximum loading of the crane including the safety margin. Finally, it is recommended to increase the distance between the CoG and the point where the vertical hoisting wire split into two as well as the angle between the two wires, in order to decrease the root displacement and fluctuation.

This thesis study has contributed aerodynamic understanding of a highly twisted and prebend wind turbine blades in extreme inflow angles and installation stability to the body of knowledge by developing an aeroelastic model capable of simulating the loads and movement of a hoisted blade and verifying the underlying principle by high-fidelity computational fluid dynamic analysis.

Acknowledgements

It was already 2013 that I started thinking about the thesis. Although the thought of "having to do" a master thesis completely "by myself" sounded utterly uncomfortable since the start of this study, I actually felt ready to start with this personal master piece. One year latter, I look back on a year in which I have learned many things, both important as well as silly: Supervisors who have lots of more experience actually are often right :) Always reread everything you programmed and wrote during the *Ballmer peak*. You can only care for someone, when you take care of yourself. Family is the most important of all. The year 2014 was a very intense year and I wouldn't have enjoyed it and brought this thesis to a successful end without the help of my dear family, friends and supervisors.

First, I would like to take this opportunity to acknowledge my supervisors, Mac Gaunaa, Sander van Zuijen and Ernst Soons, who have contributed to the successful completion of this master thesis. The many Skype calls with Mac were always fun, no meeting went by without a joke or two (straight blade or non-homosexual blade?). These hours were very valuable; a source of enlightening ideas, solutions to issues and new problems to be investigated. The times I thought: "okay, my results are rubbish, I will never graduate...", Sander would have replied within the hour to provide me with an explanation (*how could I not think of this myself*) and I was up and running again in no time. At Siemens in The Hague, Ernst was always willing to help me out. His kind interest in how I was doing throughout the whole year was always very comforting. I also want to acknowledge prof. Gerard van Bussel for his input and advise during the last phase of the thesis as member of my graduation committee. I would like to thank Frederik Zahle from DTU Wind Energy for his help with the meshing of the CFD domain and Anders Yde from DTU for his help with the HAWC2 code.

During those moments that I was in need of some exercise, it was always a great pleasure to get the blood pumping in those many exciting football table matches. Sometimes I felt relaxed after a match, other times it just got me more worked up, mostly depended on whether I was winning or not ;) I want to thank everyone at Siemens for the support and great time. The year 2014 was an intense year, both personal as well as study related. I want to thank my friends from Wispo, EWEM, 1-0 repers and of course my wonderful roommates for their support, beers and good times during my thesis. I lost the GAME!

A few people deserve a special thanks for their unlimited time they spend in listening to my thesis troubles and discussing every silly question I could think of. Whether it was the middle of the night or a very earlier morning and I encountered the most bizarre errors and bugs, Christopher was there to answer every question I could throw at him through every medium I could think of! I want to thank Dieter for the good moments of reviewing all the wonderful and annoying aspects of our thesis over the delight of many delicious coffees or beers or both. The moments that I thought that I truly had a unique issue or epiphany it was Bram who would send me he "just" had the most unique issue or epiphany, which ended up to be identical :) Bram thank you for all the good conversations in which we would *go back to the basics* (inevitable leading back to freshman year questions such as "what is lift actually?"). And by the way Bram, thank you for the miscellaneous ramifications you kindly provided the single-to-last day before printing this document.. ;) Christopher, Dieter and Bram, thank you for being one of my best friends and reminding me that "*The pain will be a distant memory, but the pride will remain.*" -Bear Grylls".

Much can change in one year, in fact, much can change in one day. This is also the general feeling which I started to understand the past year. If this is concerning my thesis or personal life, much can change in one day, meaning that good things come and go, on large and small scale. I consider it good to feel and acknowledge this, as it will help to put things in perspective and focus on the beautiful things. However there are always those days where you think that the current events are out of control and you can't seem to see the forest for the trees. I am grateful to have a family who are easily able to help me clear out the clouds in those days. I would like to thank my lovely family and girlfriend for their support throughout this year, my complete study and all the years before.

I want to thank Sita, my girlfriend, for all the times she kept listening to me telling her I really did not want to bother her with my thesis nonsense, while I would have been giving a monologue for more than an hour! I am happy that she always was there to point me to the fact that I should also "enjoy" the thesis :) She showed me that making sure to enjoy every day is the only real *sustainable* way of working. I want to thank Ida for the unbelievable dedication of reading my report for two straight days (and giving me tons of extra work btw) ;) More so I'd like to thank her for the fact that she was always there for me, whenever, wherever. Ida, thank you for being the best sister! I loved to go home to my parents and although sometimes I got in just before midnight and left just before sunrise, they were a tremendous boost of energy and happiness. I want to thank my mother for being so astonishingly strong throughout this tough year and making sure I would also think about myself :) I'd like to thank my dad for his inexhaustible care and delicious earlier morning eggs. There is absolutely nothing better to start the day than by receiving such love!

"Want het leven moet je vieren, nooit een beetje maar volop!"

Contents

Summary	v
Acknowledgements	ix
List of Figures	xvi
List of Tables	xvii
Nomenclature	xviii
1 Introduction	1
1.1 Background	1
1.2 Research	2
1.3 Outline	2
2 Research Introduction	3
2.1 Horizontal Single Blade Mounting	3
2.2 Research Question & Objectives	4
2.3 State of the Art Analysis	6
2.3.1 Calculation of Hoisting Forces on Wind Turbine Blades	6
2.3.2 Aerodynamic and Aeroelastic Behaviour of Single Blade Installation	7
2.3.3 Drag Prediction for Blades at High Angle of Attack Using CFD .	7
2.4 Methodology	8
2.4.1 Work Breakdown	8
2.4.2 Reference Frame & Angle Definition	9
2.4.3 Numerical Set-up	10
2.4.4 Limitations & Assumptions	13

3 Theoretical Background	15
3.1 Dynamics	15
3.1.1 Degrees of Freedom	16
3.1.2 Multibody Dynamics	17
3.1.3 Timoshenko Beam Elements	18
3.2 Aerodynamics	18
3.2.1 Basic Lift & Drag Theory	19
3.2.2 Mean Forces & Moments	21
3.2.3 Crossflow & Streamwise Flow	22
3.2.4 Flow Separation	26
3.2.5 Standard Deviation of Forces & Moments	26
3.2.6 Mann Turbulence Model	28
3.3 Computational Fluid Dynamics	28
3.3.1 Navier-Stokes Equations	29
3.3.2 Solving the Navier-Stokes Equations	31
3.3.3 Numerical Methods	33
3.4 Summary	36
4 Aerodynamic Model	37
4.1 HAWC2 Setup	37
4.2 The DTU 10MW Blade	38
4.3 Model Setup	40
4.4 Straight Blade	41
4.5 Results & Discussion	42
4.5.1 Forces & Moments on the Blade	42
4.5.2 Comparison with Crossflow principle & Straight Blade	44
4.5.3 Standard Deviation	45
4.6 Verification	46
4.7 Summary	48
5 Computational Fluid Dynamic Model	49
5.1 ANSYS Fluent	49
5.2 Mesh Study	50
5.2.1 Richardson Extrapolation	51
5.3 Solver Setup	52
5.3.1 Turbulence Model	52
5.3.2 Boundary Conditions	53
5.3.3 Solver Settings	55
5.3.4 Convergency Criteria	57
5.4 Results & Discussion	58
5.4.1 Forces & Moments	59
5.4.2 Wake Visualisation	61

5.4.3	Streamline Comparison	62
5.4.4	Crossflow & Flow Separation	66
5.4.5	Standard Deviation	67
5.4.6	Gurney Flap	69
5.5	Verification	71
5.6	Summary	72
6	Aeroelastic Model	75
6.1	Model Setup	75
6.1.1	Dynamic Stall	77
6.1.2	Cable Properties	77
6.1.3	Blade Deformation	77
6.2	Results & Discussion	78
6.2.1	Forces & Cable Tension	79
6.2.2	Root Displacement	79
6.3	Verification	80
6.4	Validity Check	81
6.5	Summary	82
7	Parameter Study	83
7.1	Hoisting Criteria	83
7.2	Influence of Blade Orientation & Geometry	84
7.2.1	Pitch, Yaw & Forces	84
7.2.2	Pitch, Yaw & Root Displacement	85
7.2.3	Blade Geometry & Mean Forces	88
7.3	Influence of Wind Condition	89
7.3.1	Windspeed & Tackline Forces	89
7.3.2	Turbulence Intensity & Root Displacement	90
7.3.3	Gusts & Root Displacement	90
7.4	Influence of Hoisting Method	91
7.4.1	Δ Point & Root Displacement	92
7.4.2	Yoke Mass & Root Displacement	94
7.5	Hoisting Recommendations	95
8	Conclusions & Recommendations	97
8.1	Conclusions	98
8.2	Recommendations	100
References		103
A	HAWC2 Input Files	108
B	Aerodynamic Layout	115
C	Profile Coefficients	117

List of Figures

2.1	Different Blade Mounting Techniques	4
2.2	Technical Drawing of Horizontal Single Blade Mounting	5
2.3	Work Breakdown Structure	9
2.4	Reference Frame of the HSBM System	10
2.5	Global Angle Definition for Yaw and Pitch	10
2.6	Flowchart of the Numerical Set-up & the Three Research Questions	11
3.1	Simplified Illustration of HSBM System	16
3.2	Illustration of a Multibody System [26]	17
3.3	Graphical Explanation of a Timoshenko Beam Element	18
3.4	Basics Illustration of Lift, L Drag, D and Pressure Contour	19
3.5	Lift and Drag Forces under Pitch Angle $\eta = 45$ and Yaw Angle $\theta = 30$. .	21
3.6	The Crossflow Principle by Hoerner	23
3.7	Visualisation of the Crossflow Principle in the case of HSBM	24
3.8	Illustration Flow Reversal and Separation Bubble	26
3.9	CFD Finite Volume Grid Example	34
3.10	Illustration of the $y+$ value [21]	35
3.11	Visualisation of the applicability of Wall Function [20]	35
4.1	The FFA-W3-xxx airfoil series and Structural Twist Visualisation	39
4.2	3D Visualisation of the DTU 10MW Blade	39
4.3	Detailed View of the Root Showing the Gurney flap	39
4.4	The C_l - and C_d -coefficients for several Blade Stations	40
4.5	Illustration of the Reference Frame in HAWC2	41
4.6	Representation of the Blade Length and Prebend	42
4.7	Mean and Standard Deviation of Forces F_x and F_y for varying η and θ with $TI = 0.05$	43

4.8	Mean and Standard Deviation of Force F_z and Moment M_x for varying η and θ with TI = 0.05	43
4.9	Mean and Standard Deviation of Moments M_y and M_z for varying η and θ with TI = 0.05	44
4.10	F_x and F_y Comparison with the Crossflow Principle, \cos^2 , and the Straight Blade	45
4.11	F_z and M_x Comparison with the Crossflow Principle, \cos^2 , and the Straight Blade	45
4.12	M_y and M_z Comparison with the Crossflow Principle, \cos^2 , and the Straight Blade	46
4.13	Mean & Standard Deviation of the Forces for Different TI at $\eta = \theta = 0$	46
4.14	Forces Scale Quadratically with the Windspeed	47
5.1	Indication of the Mesh Density of G1, note the Length Scale	51
5.2	Richardson Extrapolation for Suitable Grid Determination	52
5.3	Velocity Inlet and Pressure Outlet of the Domain	53
5.4	Reference Frame and Inflow Definition in CFD Model	54
5.5	Visual Comparison of BC with 45° offset and Reference Case	55
5.6	CFD Best Practice and Example of Converged Forces	58
5.7	Several CFD Convergence Criteria incl. Mass Imbalance	59
5.8	CFD to HAWC2 Comparison of F_z and F_y for $-90 < \theta < 90$ and $\eta = -90, 0$	60
5.9	CFD to HAWC2 Comparison of F_x and M_x for $-90 < \theta < 90$ and $\eta = -90, 0$	60
5.10	CFD to HAWC2 Comparison of M_y and M_z for $-90 < \theta < 90$ and $\eta = -90, 0$	61
5.11	Distance from the Root to the point where the Drag acts, R_{drag}	62
5.12	Visualisation of the Wake in Airfoil Plane	62
5.13	Visualisation of the Wake in Spanwise Plane	63
5.14	Visualisation of the Streamlines	63
5.15	64
5.16	Streamline Velocities at Different Blade Stations with $\theta = \eta = 0$	64
5.17	Streamline Velocities for $\pm\theta$ at Blade Stations 2.2 and 12.2 [m] with $\eta = 0$	65
5.18	Streamline Velocities for $\pm\theta$ at Blade Stations 22.2 and 32.2 [m] with $\eta = 0$	65
5.19	Crossflow and Wall Shear Stress Indicating Flow Separation for $\eta = 0$ with $\theta = 0$ (upper) and $\theta = 20$ (lower)	66
5.20	Crossflow and Wall Shear Stress Indicating Flow Separation for $\eta = 0$ with $\theta = 40$ (upper) and $\theta = 60$ (lower)	67
5.21	Instantaneous Iso-surfaces of the q-criterion for $\theta = 0$ (northwest), $\theta = -20$ (northeast), $\theta = -40$ (southwest) and $\theta = -60$ (southeast)	67
5.22	Mean Forces & Standard Deviation from Transient Simulation and Simplified Method	68
5.23	Mean and Standard Deviation of F_x and F_y for $-90 < \theta < 90$	69
5.24	Mean and Standard Deviation of F_z and M_x for $-90 < \theta < 90$	69
5.25	Mean and Standard Deviation of M_y and M_z for $-90 < \theta < 90$	70

5.26 Effect of a Gurney Flap on the Wake Structure in $\eta = \theta = 0$	70
5.27 Normalised Drag Force Comparison with Wang et al. [47] and Uranga et al. [45]	72
5.28 Normalised Lift and Span Comparison with Wang et al. [47] and Uranga et al. [45]	72
6.1 Representation of the HSBM system in HAWC2	76
6.2 "Animation.exe" Image	76
6.3 Different Wind Velocities & Turbulence Intensities	78
6.4 F_z & Cable Tension for Different Windspeed at $\eta = \theta = 0$ with 57 ton Yoke	79
6.5 Root Displacement for different Windspeed at $\eta = \theta = 0$ with 57 ton Yoke	80
6.6 Quadratic Scaling of the Forces F_z and F_y with the Windspeed	81
6.7 Quadratic Scaling of the Tackline Force and the Root Displacement δ . .	81
7.1 Contour plot of F_x and F_y for $-90 < \theta < 90$ and $-90 < \eta < 90$	84
7.2 Contour plot of F_z and M_x for $-90 < \theta < 90$ and $-90 < \eta < 90$	85
7.3 Contour plot M_y and M_z for $-90 < \theta < 90$ and $-90 < \eta < 90$	86
7.4 δ for $\theta < 0$, with $\eta = 0$, 15 [m/s] Wind, 57 [ton] Yoke & 1% TI	86
7.5 δ for $\theta > 0$, with $\eta = 0$, 15 [m/s] Wind, 57 [ton] Yoke & 1% TI	87
7.6 δ for different η , with $\theta = 0$, 15 [m/s] Wind, 57 [ton] Yoke & 1% TI	87
7.7 δ for $\theta > 0$, with $\eta = -90$, 15 [m/s] Wind, 57 [ton] Yoke & 1% TI	88
7.8 δ for $\theta < 0$, with $\eta = -90$, 15 [m/s] Wind, 57 [ton] Yoke & 1% TI	88
7.9 Influence of TI on the Tackline Tension for different Wind velocities at $\eta = \theta = 0$	89
7.10 Influence of TI on δ at $\eta = \theta = 0$ for 10 [m/s] Wind	90
7.11 Influence of TI on δ at $\eta =$ and $\theta = -90$ for 15 [m/s] Wind	91
7.12 Forces & Root Displacement for Gusts A is 2 and 5 at $\eta = \theta = 0$	91
7.13 Definition of Δ point, Cable Lengths & Angles	92
7.14 Force Equilibrium of the Blade-Cable System	93
7.15 Influence of Δ , ξ and h on δ , for 10 [m/s] and 57 [ton] Yoke	94
7.16 Influence of Yoke Mass on Root Displacement for 10 [m/s] Wind & 1% TI	95
A.1 Simulation and Craneboom main_body Module	109
A.2 Cable 1 and 2 main_body Module	110
A.3 Blade main_body Module	111
A.4 Orientation Module	112
A.5 Constraint Module	113
A.6 Wind Module	114
A.7 Aero and Output Module	114

List of Tables

5.1	Various Parameters Indicating Mesh Quality	50
5.2	Percentage Difference between the Grids and Extrapolated $F_{z,\infty}$ and $F_{y,\infty}$	52
5.3	Flow Direction Cases and Corresponding Inflow Angles	54
5.4	The $y+$ value for the three different grids	56
5.5	Comparison of Turb. Models, Discretisation Schemes and P-V-Coupling for $\theta = \eta = 0$ at 10 [m/s] wind	56
5.6	Comparison of HAWC2 based DES and ANSYS Fluent LES performed by the author for $\theta = 0$ and $\eta = -90$	57
5.7	C_D of the DTU 10MW blade and several flat plates and other wind turbine blades	73
7.1	Different Configurations of the Single Blade Hoisting System	93

Nomenclature

Latin Symbols

\bar{F}	Mean Force	[kN]
\bar{M}	Mean Moment	[kNm]
\bar{U}	Mean Velocity	[$\frac{m}{s}$]
A	Area	[m^2]
A	Gust Amplitude	[$\frac{m}{s}$]
c	Chord Line	[m]
C_D	Three Dimensional Drag Coefficient	[–]
C_d	Two Dimensional Drag Coefficient	[–]
C_L	Three Dimensional Lift Coefficient	[–]
C_l	Two Dimensional Lift Coefficient	[–]
C_m	Two Dimensional Moment Coefficient	[–]
D	Drag Force	[kN]
F	Force	[kN]
f	Frequency	[Hz]
F_x	Force in x - or spanwise direction	[kN]
F_y	Force in y -direction	[kN]
F_z	Force in z -direction or minus Lift	[kN]
h	Richardson's Mesh Spacing	[–]
k	Turbulent Kinetic Energy	[$\frac{m^2}{s^2}$]
L	Length Scale	[m]
L	Lift Force	[kN]

M	Mach Number	[–]
M	Moment	[kNm]
M_x	Moment around x -axis or Pitching	[kNm]
M_y	Moment around y -axis or Rolling	[kNm]
M_z	Moment around z -axis or Yawing	[kNm]
p	Pressure	[$\frac{N}{m^2}$]
p	Richardson's Order of Discretisation	[–]
q	Dynamic Pressure	[$\frac{N}{m^2}$]
R	Blade Station or Airfoil Section from the Root	[m]
r	Richardson's Refinement Ratio	[–]
Re	Reynolds Number	[–]
St	Strouhal Number	[–]
t	Time	[s]
TI	Turbulent Intensity	[–]
U_∞	Undisturbed Incoming Velocity	[$\frac{m}{s}$]
$y+$	Dimensionless Wall Distance	[–]

Greek Symbols

α	Angle of Attack	[°]
δ	Root Displacement	[m]
η	Pitch Angle: around the x -axis	[°]
λ	Heat Conductivity	[$\frac{W}{mK}$]
μ	Dynamic Viscosity	[$\frac{kg}{m \cdot s}$]
ν	Kinematic Viscosity	[$\frac{m^2}{s}$]
ν	Roll Angle: around the y -axis	[°]
ω	Specific Turbulence Dissipation	[$\frac{1}{s}$]
ϕ	Tackline Angle in Horizontal Plane	[°]
ψ	Tackline Angle in Vertical Plane	[°]
ρ	Air Density	[$\frac{kg}{m^3}$]
σ	Standard Deviation	[–]
θ	Yaw Angle: around the z -axis	[°]
ε	Turbulence Dissipation	[$\frac{m^2}{s^3}$]
ξ	Angle between CoG and Diagonal Hoisting Cable	[°]
ξ	Structural Pitch Angle	[°]
ζ	Rotation of the CoG	[°]

Abbreviations

<i>2D</i>	Two-Dimensional
<i>3D</i>	Three-Dimensional
<i>AR</i>	Aspect Ratio
<i>AoA</i>	Angle of Attack
<i>BC</i>	Boundary Condition
<i>BEM</i>	Blade Element Momentum
<i>CDS</i>	Central Differencing Scheme
<i>CFD</i>	Computational Fluid Dynamics
<i>CoG</i>	Centre of Gravity
<i>DES</i>	Detached Eddy Simulation
<i>DNS</i>	Direct Numerical Simulation
<i>DoF</i>	Degree of Freedom
<i>DTU</i>	Denmark Technical University
<i>HAWC2</i>	Horizontal Axis Wind turbine simulation Code 2nd generation
<i>HSBM</i>	Horizontal Single Blade Mounting
<i>LCoE</i>	Levelised Cost of Energy
<i>LES</i>	Large Eddy Simulation
<i>MBD</i>	Multibody Dynamics
<i>NS</i>	Navier-Stokes
<i>QUICK</i>	Quadratic Upwind Interpolation for Convective Kinetics
<i>RANS</i>	Reynolds Averaged Navier-Stokes
<i>SIMPLE</i>	Semi-Implicit Method for Pressure-Linked Equations
<i>std</i>	Standard Deviation
<i>SWP</i>	Siemens Wind Power
<i>UDS</i>	Upwind Differencing Scheme

Chapter 1

Introduction

This thesis study is about the prediction of the aerodynamic loads and forces on a horizontally orientated wind turbine rotor blade being assembled in offshore conditions in order to improve the future installation methods. The study was carried out in cooperation with Siemens Wind Power. The aim of the investigation is to gain better understanding in the aerodynamic effects around the rotor blade in horizontal position and use this information to predict the effects on the complete installation system and procedure. This research project will lead to more knowledge about the wind turbine assembly procedure and possible solutions in order to raise the current maximum wind speed during installation and thereby increasing the allowable weather window and consequently lower the levelised cost of energy (LCoE) of offshore wind.

1.1 Background

The subject of the thesis concerns the construction of a Siemens 6MW offshore wind turbine with a blade length of 75 meters. The study particularly focuses on the assembly of the blade to the hub of the wind turbine. Due to weather conditions and safety regulations Siemens is limited to a maximum wind speed, approximately 10 [m/s] for single blade installation. In the North Sea this comes down to an installation window of roughly two months in the summer or even less when higher wind speed regions offshore are explored. For horizontal single blade mounting (HSBM) Siemens wants to be able to install in wind velocity up to 14 [m/s], which will increase the installation window to several months throughout the year. HSBM has not yet been performed for the Siemens 6MW turbine. In addition, wind turbine installation in wind velocity up to 14 [m/s] has not been done before and is challenging technical boundaries with respect to the weather limit. At the same time installation needs to be quicker than before while turbine sizes and weights increase.

1.2 Research

The challenges mentioned above call for a detailed investigation into improvements to the installation method and the full impact thereof. In this thesis study the aerodynamic effects of the wind speed under different weather and installation conditions will be investigated by means of aeroelastic simulation with HAWC2 [16, 18]. The results will be validated with a computational fluid dynamic analysis in ANSYS Fluent by means of comparing the mean forces and moments on the blade during installation. Both software and models will be thoroughly explained and discussed in this report. Moreover it is investigated how the aerodynamic loads can be reduced and the installation more controlled by studying the influence of different wind conditions and hoisting methods. These key aspects of the installation will be tested by means of a parameter study.

1.3 Outline

In Chapter 2 an introduction to the conducted research is given, including current installation methods, their shortcomings and the state of the art concerning scientific papers and academic research. Chapter 2 will also state and explain the three research questions and justify the chosen methodology. A thorough theoretical background in the fields of dynamics and aerodynamics is given in Chapter 3, providing the reader with the desired knowledge to understand the technical issues and models discussed. The main body of this research is broken down into three Chapters: 4, 5 and 6, which presents and discusses the three numerical models developed in this thesis study. All three chapters are consistently built up with an introduction, model setup, results & discussion, verification and a summary.

Chapter 4 provides the explanation and method of the static *aerodynamic model* designed to compute the mean loading on the blade during installation. Furthermore, the model will be verified with research papers discussed earlier in the state of the art analysis, in Section 2.3. In Chapter 5 the previous designed model will be verified with the *CFD model* by determining the validity of the engineering basis of the *aerodynamic model*. Following, in Chapter 6 the actual horizontal single blade lifting will be simulated over time with the *aeroelastic model* and the prior obtained knowledge of the validity of the engineering basis. In Chapter 7 the *aeroelastic model* will then be used to determine key parameters affecting the stability of the HSBM system by means of a sensitivity check. Chapter 7 will conclude with recommendations on possible solutions for installation in higher wind velocities and discuss the accuracy of the results obtained. Finally, conclusions on the complete research are drawn and recommendations for future investigation are given in Chapter 8.

Chapter 2

Research Introduction

In the following Chapter 2, an introduction to the research is given consisting of single blade mounting within Siemens Wind Power as well as other standards in the industry. The research problem will be stated in Section 2.2 and subsequently from that problem statement the research questions will be deduced. Furthermore, the current state of the art regarding scientific research is reviewed, which will later be used to justify the chosen methodology and as verification purpose. Finally, in Section 2.4, the methodology including experimental set-up, reference frame definition and assumptions will be discussed.

2.1 Horizontal Single Blade Mounting

In the industry a broad spectrum of wind turbine installation techniques are currently performed of which the three most common techniques are discussed briefly in this section.

The first and least commonly used technique is the "*bunny ear*" method, where two blades, hub and nacelle are preassembled at the port, resembling a bunny's head. This method requires four lifts at the site: the bunny ears, the third blade and the tower consisting of two pieces. Advantages are the few amount of lifts at the site, on the other hand the nacelle, hub and blades combination needs to be preassembled leading to a larger required deck space.

The second technique is the full rotor lift, in Figure 2.1(c), and is commonly used both on- and offshore. The hub and three blades are preassembled and transported in one piece to the site where four lifts are needed to install the turbine: rotor, nacelle and two tower pieces. The few lifts and small required deck space are advantageous, the downsides are the complexity of the assembly and the alignment of the hub to the nacelle.

Finally the most used method, the single blade lifting, can be operated in varying orientations: horizontal, tilted and vertical. Horizontal, in Figure 2.1(a), and vertical lifting require the hub to rotate in order to assemble each blade, while tilted lifting, in Figure 2.1(b), can be done with a fixed hub. The latter is favourable for direct-drive turbines

since no gearbox is present to provide the large moment to rotate. Horizontal lifting is preferred over vertical lifting since no rotation is needed as the blades are horizontally stored on the vessel. Furthermore, the tilted lifting requires a longer boom crane since the blade needs to be lifted higher than hub height which becomes more challenging with the increasing wind turbine size. Figure 2.1 gives an impression of three of the discussed techniques.



Figure 2.1: Different Blade Mounting Techniques

Siemens WP is capable of executing all mentioned techniques. The blade or rotor is lifted with a crane from the installation vessel up to the hub height where the jointing and assembling is done. All installation methods include a jack-up rig, with the crane on one of its legs. A technical drawing of the hoisting procedure is presented in Figure 2.2. In case of HSBM, the blades are lifted up horizontally leading-edge down from the vessel storage rack. Horizontal tacklines run from the yoke, which is holding the blade, to the crane in order to rotate the blade appropriately. The blade is guided and controlled by the guide wires which run along the crane boom and are connected to the traversing system. The cables are under tension and are able to compensate for wind gust disturbances.

The overall objective of the traverse system is to transmit the tackline force to the crane structure using a guide wire. The top and bottom traverse system are clamped to the crane boom and hold the guide wires. The guide wires are attached to the tacklines which in turn are fixed to the blade yoke. The tacklines are under tension and ensured to remain horizontal and attached to the blade yoke under a 90° angle for optimal control. If the tackline force attacks only in one guide wire, the crane structure will be subjected to bending moment and torque, which is undesired and should be avoided. This brief explanation should give the reader relevant insight into the HSBM technique. Now that the current blade installation process is understood, the problem statement can be defined and from that the research questions derived.

2.2 Research Question & Objectives

In reality, the wide variation of methods which are being performed nowadays are all limited to 10 [m/s] wind velocity, constraining the installation considerably. In spite of the profound research in wind energy, thorough understanding of the aerodynamic effects on a non-rotating blade during installation and its effect on the hoisting system is yet to be determined. This problem statement is the driver for conducting this thesis research

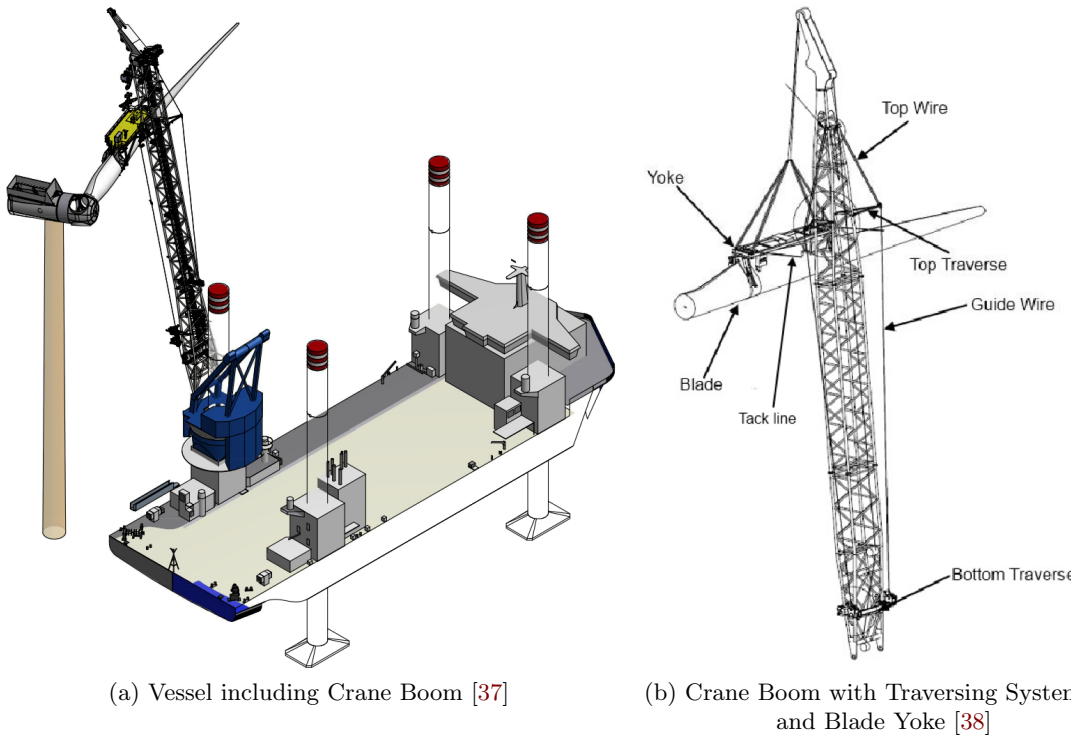


Figure 2.2: Technical Drawing of Horizontal Single Blade Mounting

and could lead to improved understanding of the key parameters and crucial aspects of wind turbine installation. From this problem statement the following research objective is deduced.

The research objective is to improve the robustness of wind turbine blade installation for extreme wind conditions, by investigating the aerodynamic forces around a non-rotating blade in various orientations, by means of numerical modelling. The research question is a threefold:

1. *How to model the aerodynamic forces and dynamic behaviour of a hoisted wind turbine blade in different inflow angles?*
2. *What are the critical parameters affecting the blade response e.g. orientation, turbulence and gusts?*
3. *How can single blade mounting be improved for higher wind speeds?*

The aim of this thesis, finding a solution for the single blade installation in high wind speeds for large MW wind turbine blades, will be achieved by carrying out the following five main tasks: 1) Computing the aerodynamic forces on a blade in hoisting orientation. 2) Validate the obtained results with a high-fidelity model. 3) Determine the motion of the blade due to these forces. 4) Conduct a parameter study to determine the crucial variables of the system based on the motion of the blade. 5) Test the system to indicate the influence of key parameters using a sensitivity study. The first task will be carried

out in Chapter 4 with the *aerodynamic model* following by the second task in Chapter 5 by the *CFD model*. Afterwards the third task is discussed in Chapter 6 with the help of the with the *aeroelastic model*. The fourth and fifth tasks are carried out in Chapter 7 by means of a parameter study.

2.3 State of the Art Analysis

As the project aim and objective has been defined, a literature study is conducted into the current knowledge and scientific research as well as into a broad range of relevant peer reviewed papers. This literature study has been done prior to this thesis by Kuijken [17], however the three most relevant scientific papers done by research institutes and universities are reviewed in the following sections. These articles will provide the reader with the required information to better understand the previously defined research questions and motivation for the chosen methodology. The first papers by Wang et al. [46] and Gaunaa et al. [12] specifically focus on wind turbine installation and are the fundement of this research, and will be discussed in Section 2.3.1 and Section 2.3.2 respectively. The last paper, in Section 2.3.3 by Sørensen and Michelsen [39], provides the relevant knowledge to motivate the numerical method used.

2.3.1 Calculation of Hoisting Forces on Wind Turbine Blades

Research has been done, by Wang et al. [46], into the assembly and hoisting process of a wind turbine rotor in an open wind environment in order to improve the hoisting safety, efficiency and quality. In this investigation the hoisting forces of a 83.5 meter diameter 1.5 MW wind turbine are computed in a three-dimensional coordinate system for different orientations, using the *GH Bladed 3.81* software. The experiments are done at different hub heights and for roll angles between 0° and 180° , yaw angles between 0° and 360° and pitch angles between -90° and 90° . In theory, the loads should be kept steady to avoid violent swinging and flapping of the blade. However due to gusts and wind direction changes, the loads can not be kept constant throughout the whole process. For simplification the computations are done in steady wind speed and for one turbulent case. The accelerations of the blade caused by the wind loading are not discussed. The maximum and minimum forces per blade orientation are presented in order to provide companies with the best option for lifting the blade. In addition, the hoisting forces and distribution along the height increment are calculated and summarised. In a second paper Wang et al. [47] determines the hoisting forces on a 38.5 meter wind turbine blade in multiple positions using steady-state computational fluid dynamics. Computational fluid dynamics (CFD) is a numerical calculation method of the Navier-Stokes equations and is thoroughly explained in Section 3.3.1. A total of 252 hoisting forces are computed for all different orientations and the maximum and minimum forces with the corresponding pitch angle, roll angle and yaw angle are obtained. Due to the complexity of the wind conditions, only steady wind conditions are used and the hoisting forces in particular positions of the blade are computed accurately.

These two research articles, calculating the hoisting forces either using engineering models or computational fluid dynamics, are one of few papers focusing solely on the hoisting of a wind turbine blade and are therefore relevant papers for this thesis study. Nevertheless these investigations do not or barely take into account turbulence nor the dynamic effect of the hoisting forces on the blade. However the research paper states that this is of importance and recommends determining the dynamic effects for future research. As the safety and possibility of hoisting in certain wind conditions mainly depend on the oscillation and movement of the blade rather than only the mean forces, thus frequency and blade rotations should be included in this investigation. However these two research papers provide valuable data which will be used in order to verify and compare the results obtained in this thesis study.

2.3.2 Aerodynamic and Aeroelastic Behaviour of Single Blade Installation

Recently [Gaunaa et al. \[12\]](#) investigated the aerodynamic and aeroelastic behaviour of a single wind turbine blade lifted during installation. The calculations were done on a 86.37 meter long blade, weighing nearly 42 tonnes, with a maximum chord of 6.2 meters. The blade is taken from the openly available specifications of the DTU 10MW Reference Wind Turbine by [Bak et al. \[5\]](#). Three models are developed in this research, an engineering model, a generalised aeroelastic model and a HAWC2 aeroelastic model, a simulation code developed at DTU Wind Energy [\[19\]](#). The engineering model is capable of returning an analytical relation that allows to scale the aerodynamic loads as function of key site parameters: wind speed, turbulence intensity and blade orientation. The generalised aeroelastic model of the single blade installation system consists of the stiff blade, yoke and cables and estimate the tacklines forces. The aerodynamic load predictions from the engineering model have proved to be in excellent agreement with HAWC2 results, and combined with a generalised model of the yoke tackline system allow to quickly obtain a prediction of the forces the tackline systems will have to counteract. [Gaunaa et al. \[12\]](#) provides a general scaling of the mean aerodynamic forces and its standard deviation for a large range of different yaw and pitch inflow angles. It is concluded that the highest aerodynamic loads, and hence tackline tensions, are reported for blade pitch angles where the drag prevails ($30^\circ < \text{pitch} < 150^\circ$), and for wind directions perpendicular to the blade span axis.

2.3.3 Drag Prediction for Blades at High Angle of Attack Using CFD

The blade needs to be able to be lifted in all possible orientations. This leads to two distinct problems: large crossflow and large angles of attack. Normally, when working with typical aeroelastic design codes, computations for these situations are based on the Blade Element Momentum (BEM) or lifting line methods, both relying on airfoil tables of lift and drag. As very little data exist for airfoils at very high angles of attack (above 40 degrees) and knowledge of eventual 3D effects are limited, these computations become very uncertain. In 2004 [Sørensen and Michelsen \[39\]](#) demonstrated that state of the art three-dimensional computational fluid dynamics codes are capable of predicting the correct dependency of the integrated drag of a flat plate placed perpendicular to the flow.

The CFD computations were first done on a flat plate in order to validate the code with existing experimental data from Hoerner [13]. From this, it is evident that CFD is capable of predicting the drag coefficient for the plates in very good agreement with measured values. The deviation is below 2% for all different aspect ratio cases. In the second step Sørensen and Michelsen [39] investigated the drag distribution of wind turbine blades parked at 90 degrees to the oncoming flow. In the study for four wind turbine blades, integrated drag value between 1.16 and 1.32 was found, in good agreement with existing full scale measurements on other wind turbine blade geometries. Additionally the drag in the root region was approaching the value found for cylinders of aspect ratio below 10, which may be quite realistic.

2.4 Methodology

The methodology for this thesis investigation is based upon the previous discussed research papers in Section 2.3 and the research questions in Section 2.2. First from the research questions, a work breakdown will be discussed and presented in Section 2.4.1. Following the reference frame will be defined in Section 2.4.2. The three scientific papers are the fundament of the chosen numerical setup and will be elaborated in Section 2.4.3. Finally, the limitations and assumptions will be pointed out and discussed in Section 2.4.4.

Studying all the different procedures of blade lifting and assembly before starting to analyse data is important in order to establish a global view on the current industry standards. The next step is gaining understanding in the possible aerodynamic forces on the rotor blade and the effects on the complete system. Global knowledge of the possible effects on a wind turbine blade in these extreme orientations will provide the framework to justify the outcome and results which will later be obtained. After the simulation by means of numerical models based on basic lift theory, the results will be validated by a high-fidelity model. The advantages of the basic numerical model is the low computational cost compared to the assumed accuracy, on the contrary the high-fidelity model will provide higher accuracy at the cost of computational effort. This high-fidelity model will be based on more complex aerodynamic theory and provide more detailed and accurate information. The model will be verified with peer reviewed research papers and the input needed for this model will be obtained from validated numerical data provided by DTU Wind Energy. With the forces and moments of the blade as outcome, time depending simulation will be computed and inspected for feasibility by verification. The limiting factors of the blade hoisting process are examined, e.g. maximum displacement, forces and fluctuations, and will provide a set of criteria that must be met by the blade installation system.

2.4.1 Work Breakdown

From the literature review conducted prior to this thesis by Kuijken [17] it is seen that little scientific research has been done on the hoisting procedure and on the aerodynamic loads of an extremely yawed and pitched blade. These scientific aspects need to be assessed and embedded in a research plan that includes clear thesis objectives. In Figure

2.3 the work breakdown structure is illustrated. The work is divided in six pillars which are consequently divided into sub packages.

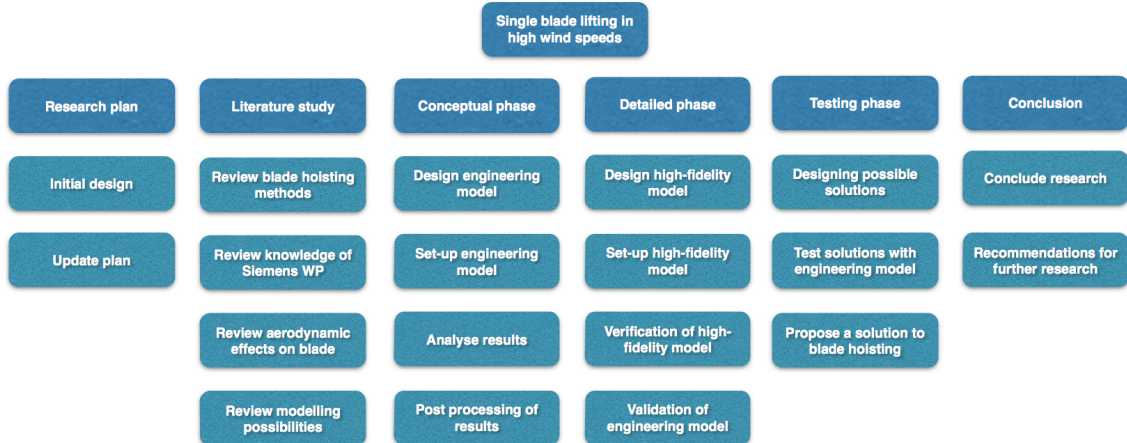


Figure 2.3: Work Breakdown Structure

The thesis research consists of six phases or pillars; the first is drafting a research plan and secondly conducting a literature study covering all relevant topics. Afterwards, in the conceptual and third phase the basic model is created and the first results are obtained and analysed. The fourth and largest phase starts with designing a high-fidelity model and verifying it with research data. The verified high-fidelity model will be used to validate the basic lift model for extreme blade orientations. Possible solutions to increase the allowable hoisting wind speed are conceived and tested in the fifth phase where ultimately hoisting recommendations are proposed. Finally, the research is concluded and recommendation are made for further studies.

2.4.2 Reference Frame & Angle Definition

Before the numerical setup can be explained the angles should be clearly defined. The global reference frame can be seen in Figure 2.4. The z -axis is defined normal to the ground pointing positive downwards, the x -axis points positive along the blade towards the tip and the y -axis points according to the righthand rule. The angles are defined as seen in Figure 2.5, zero degrees pitch, η , i.e. rotation around the x -axis, is defined when the airfoil chord line at zero twist is parallel with ground. Zero degrees yaw, θ , i.e. rotation around the z -axis, is defined when the inflow is perpendicular to the blade length. Finally, zero roll, hence rotation around the y -axis, ν , is defined when the span, tip to root, of the blade is parallel with the ground. In this study ν will always be considered zero. Figure 2.4 clearly indicates the incoming velocity, U_∞ , for $\eta = \nu = 0$ and $\theta = -45$. The pitch and yaw angle, η and θ respectively, are subdivided in angle regions according to Figure 2.5. Note that positive pitch η is rotating the blade positive around the x -axis, i.e. increasing the angle of attack. The positive yaw θ is rotating the wind vector negative around the y -axis, such that $\theta = -90$ is flow from tip to root.

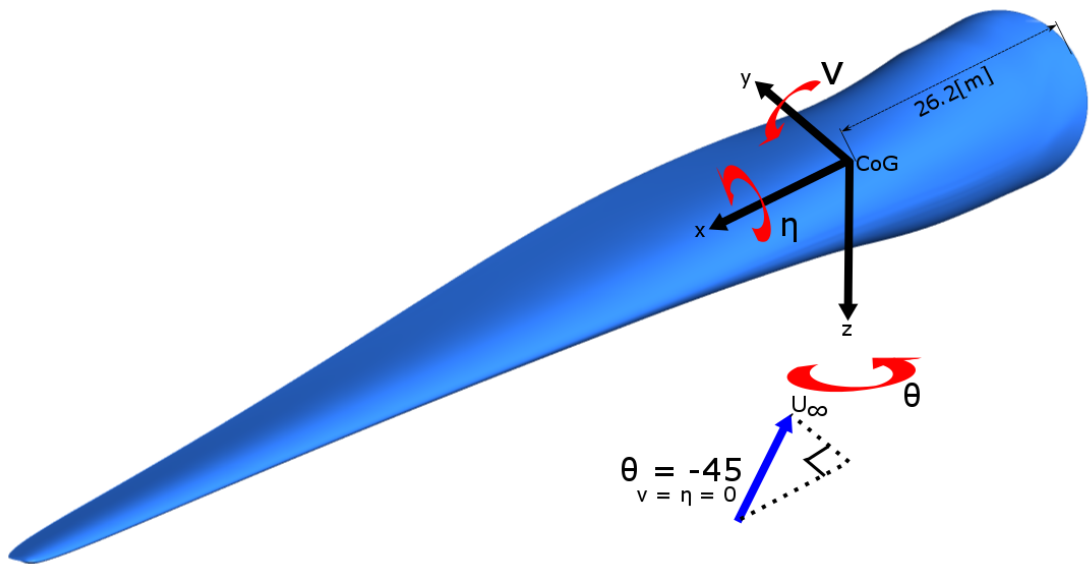
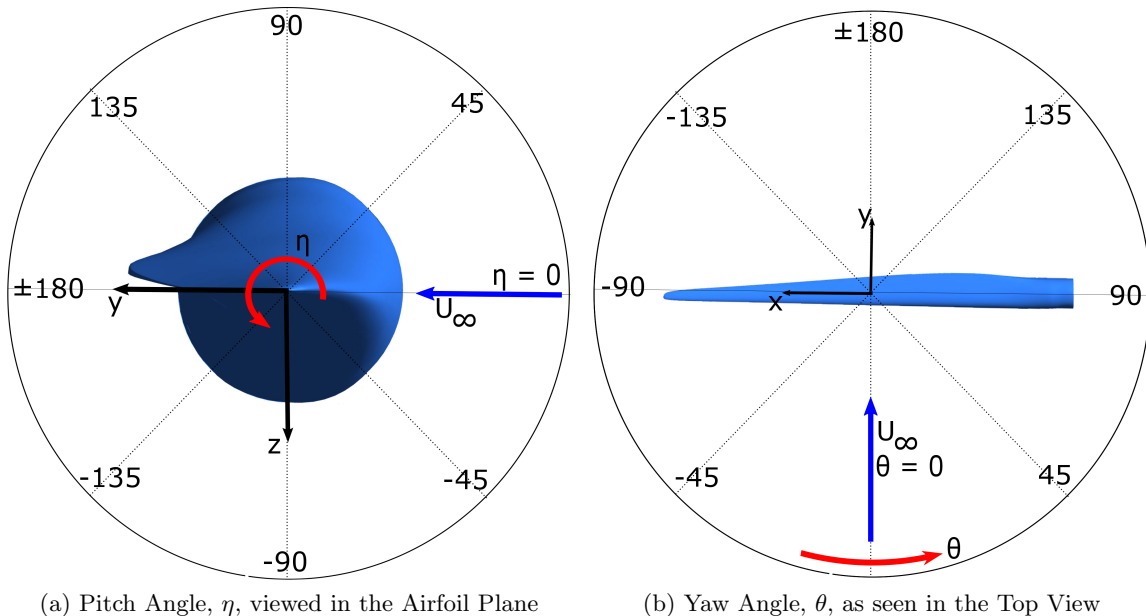


Figure 2.4: Reference Frame of the HSBM System



(a) Pitch Angle, η , viewed in the Airfoil Plane

(b) Yaw Angle, θ , as seen in the Top View

Figure 2.5: Global Angle Definition for Yaw and Pitch

2.4.3 Numerical Set-up

The numerical set-up will be discussed according to the three research questions: **1.** *How to model the aerodynamic forces and dynamic behaviour of a hoisted blade?*, **2.** *What are the critical parameters affecting the blade response?* and **3.** *How can single blade mounting be improved for higher wind speeds?*

In order to answer the first research question, theory from research topics on dynamics

and aerodynamics must be known. In particular it must be known what the aerodynamic forces are on the blade and how they affect the dynamic system. The integrated theoretical background on dynamics and aerodynamics is elaborated on in Chapter 3.

Aerodynamic forces on blades were covered by the research papers of Gaunaa et al. [12] and Wang et al. [46] and are discussed in Section 2.3. These are solely steady-state, meaning the blade is modelled as if it would be clamped and no cable dynamics nor aeroelastic coupling is taken into account. The coupling between the dynamic behaviour of the blade/cable system and the aerodynamic loads is highly complicated and requires the need of an aeroelastic model. The code HAWC2 by DTU Wind Energy[19] will be used as aeroelastic model, refer to Chapter 6 for details on this model. Besides an aeroelastic model, a CFD model and aerodynamic model will be developed.

The following flowchart in Figure 2.6 illustrates the numerical set-up of the thesis and used references for verification purposes. The number in the left upper corner indicates for which research question the model or output is needed.

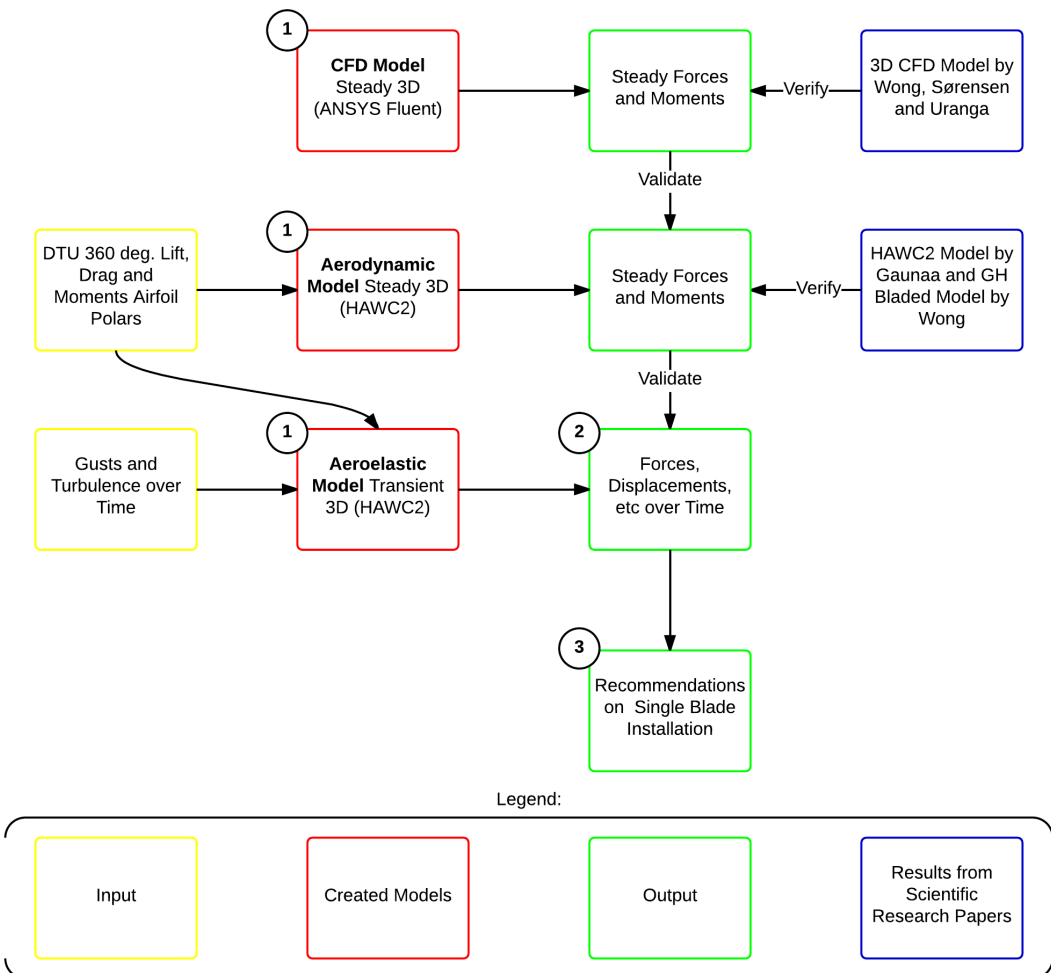


Figure 2.6: Flowchart of the Numerical Set-up & the Three Research Questions

The Aeroelastic Model

Firstly, from the research objective, providing recommendations on single blade installation; the forces, displacements and cable tension over time are needed, hence the *aeroelastic model* is developed. This aeroelastic model in HAWC2 will use accurate input data from DTU Wind Energy in order to predict the lift, drag and moments on the blade from the airfoil coefficients; C_l , C_d and C_m respectively. Airfoil coefficients are dimensionless coefficients that relate the force (e.g. lift) generated by a lifting body to the density of the fluid, its velocity, the inflow angle and an associated reference area. These coefficient are determined for sections along the blade span (i.e. airfoil section) and can be calculated using the thin airfoil theory, by Abbott and Von Doenhoff [3], calculated numerically or determined from wind tunnel tests.

In this particular situation coefficients for 360 degree around the airfoil are needed since the blade might be lifted in all possible orientations. Since such an enormous blade could not fit in a wind tunnel and thin airfoil theory is not accurate for large inflow angles, the coefficients are created from transient large eddy 3D CFD analysis for a range of 360 degrees by DTU Wind Energy. Note that specifications on different methods of computational fluid dynamics will be explained later in Section 3.3. Furthermore, also gusts and turbulence as function of time will be an input to the *aeroelastic model* in order to investigate the influence of unsteadiness on the system. Specification of the *aeroelastic model* can be read in Chapter 6. In the flowchart in Figure 2.6 the initial input to the models are outlined in yellow, whereas the created models are indicated in red.

The CFD Model

Secondly, the HAWC2 code however is based on the crossflow principle, later discussed in Section 3.2.3, which limits the accuracy in yaw angles θ , where the error is maximum for $\pm 90^\circ$. In order to validate the forces calculated by the HAWC2 code a high-fidelity *CFD model* is created. Although simulating the full aeroelastic effects of the HSBM system would require the use of Fluid Structure Interaction (FSI), which is highly computational expensive, CFD is the most suitable approach. Moreover the research paper by Sørensen and Michelsen [39] indicated the good capabilities of 3D CFD in predicting the drag forces. In addition, Gaunaa et al. [12] recommend the use of 3D CFD to verify the validity of its HAWC2 model. Specification of the *CFD model* can be read in Chapter 5.

The Aerodynamic Model

Thirdly, it must be ensured that the validation is done with similar conditions, since the *aeroelastic model* is transient (time-dependent) and the *CFD model* steady-state. Therefore a third model is developed, the *aerodynamic model*, also with the HAWC2 code and thus with similar capabilities and limitations, i.e. the crossflow principle. The *aerodynamic model* will be 3D and steady-state and solely calculates the forces and moments on the blade as if it would be clamped. A more elaborate description on this model is found in Chapter 4.

Both the *CFD model* as well as the *aerodynamic model* will deliver the forces on the blade in all direction based on 3D steady-state calculations. As already discussed, the simple

basis of the crossflow principle in the *aerodynamic model* will likely contain an error in the forces for large yaw angles θ . However due to its computationally cheap nature, this model will be able to generate results with very high resolution, 5° , while the *CFD model* needs more time to compute, such that less cases can be calculated leading to a lower resolution. Nevertheless, the more complex CFD model will be able to simulate more aerodynamic effects leading to the higher accuracy, which is used for validation of the aerodynamic model.

Verification

Fourthly, in blue the scientific research papers for verification purposes are illustrated. In Section 2.3 the research done by [Gaunaa et al. \[12\]](#) was presented. The HAWC2 code of [Gaunaa et al. \[12\]](#) will be used to verify the results from the *aerodynamic model* created in this thesis study. The GH Bladed model developed by [Wang et al. \[46\]](#), although on a different blade, will be used to verify the results from the *aerodynamic model* by means of trends and extrema of the forces. Similarly the 3D CFD results by [Wang et al. \[47\]](#), [Sørensen and Michelsen \[39\]](#) and [Uranga et al. \[45\]](#) will be used to verify the trends of the *CFD model*.

The Output

Finally, having verified the steady forces and moments on the blade, a judgement can be made on the accuracy and validity of the *aeroelastic model* answering the first research question. Thereupon the output (green) from the aeroelastic model will provide the answer to the second question, **2. what are the critical parameters affecting the blade response?**. This is done by conducting a parameter study to investigate the influence and sensitivity of certain variables and parameters. Followed a set of criteria for this model can be defined to determine the critical parameters. Knowing the critical parameters affecting the blade response and the limitations of the *aeroelastic model* the final phase can kick-off.

In the final phase, the third research question is answered, **3. how can single blade mounting be improved for higher wind speeds?**. The criteria which the HSBM system must satisfy are used to determine favourable and unbearable blade orientations and hoisting methods. The sensitivity of various variables together with the knowledge of the static forces, recommendations can be made to improve the current HSBM system.

2.4.4 Limitations & Assumptions

Before embarking upon the simulation and modelling of the aeroelastic system, the assumptions and limitations are set out in order to judge the validity of the research.

The assumptions of the research are summarised as follows:

- The DTU Wind Energy airfoil data based upon detached eddy simulation is accurate.

- Comparison of mean forces between the CFD model and the aerodynamic model will indicate the validity of the crossflow principle.
- The crane dynamic deformation and cable elongation is assumed to be negligible.
- The blade is assumed stiff, due to the fact that the dynamic movement of the blade is low and the blade deformation can be neglected.
- Quasi-steady aerodynamics is adequate in this case where the blade is rigidly clamped in its centre of gravity.

The limitations of the chosen methodology are itemised as follows:

- The CFD simulation is done in a steady-state which disregards the unsteady effects that might arise.
- The *aeroelastic model* does not incorporate sagging of the tacklines, due to its own weight.

Chapter 3

Theoretical Background

There is a theoretical background that must be understood prior to any analysis through numerical simulation or experimental measurements. This part of the thesis discusses the theoretical basis of the work. In order to answer the first research question, **1.** *how to model the aerodynamic forces and dynamic behaviour of a hoisted wind turbine blade in different inflow angles?*, theory needs to be understood from research topics on dynamics and aerodynamics. Relevant aerodynamic effects and theory on the determination of the forces on the blade are presented. However, in order to properly determine the movement of the blade, the effect of these forces on the blade/cable systems need to be modelled. This coupling between the aerodynamic forces and the dynamic response can be described by means of aeroelastic simulation.

Important research papers which have already examined wind turbine installation have been reviewed in Section 2.3 and thorough discussion of relevant scientific literature is done prior to this thesis by Kuijken [17]. Nonetheless a concise theoretical background is needed to provide the necessary expertise and understanding which will start with documentation regarding dynamic modelling in Section 3.1. Afterwards the aerodynamic modelling is presented in Section 3.2, including among others, basic theory of lift and drag and the principle of crossflow. Computational fluid dynamics is introduced in Section 3.3, which will review the Navier-Stokes description of fluid motion and ways of solving it numerically.

3.1 Dynamics

The motion of a free hanging blade suspended from two cables, as illustrated in the Figure 2.2, can be described by a dynamic model. The blade's movement is coupled to the crane boom and is constrained in certain rotations and translations due to the cable system, leaving a certain amount of degrees of freedom (DoF). In Section 3.1.1 a brief overview of possible degrees of freedom and the feasibility or necessity of including them into the dynamic model is given. Afterwards, the blade lifting system is simplified and the use of

multibody dynamics is proposed and explained in Section 3.1.2. Finally, in Section 3.1.3 a particular type of beam element is explained, which is used in the HAWC2 code.

3.1.1 Degrees of Freedom

Clearly the dynamic system becomes more accurate when including more degrees of freedom. However, on the counter part the system also becomes more complex and more computational expensive. The blade is considered the main body and has six degrees of freedom (three rotations and three translations). For the assessment of the movement of the blade a set of assumptions are made. First of all, from Hooke's Law [1] it can be determined that the elongation of the cables can be neglected under the relative low mass of the blade and yoke. Secondly, for simplicity, the jack-up vessel is assumed unaffected by the low wind and wave loading as the vessel is rigidly supported by four jack-up legs. Thirdly, the investigation is done for a crane boom in a fixed position relating to the vessel and thus has no translations nor rotations. Finally, it is assumed that the dynamic deformation of the crane is negligible as it is only loaded up to 50% of the designed maximum capacity [2]. The assumptions lead to a simplified model in which the blade is hanging from two cables which are fixed on the other end as illustrated in Figure 3.1. The origin of the reference frame is moved to the fixed end of the crane boom, however, the axis system remains the same as previously stated.

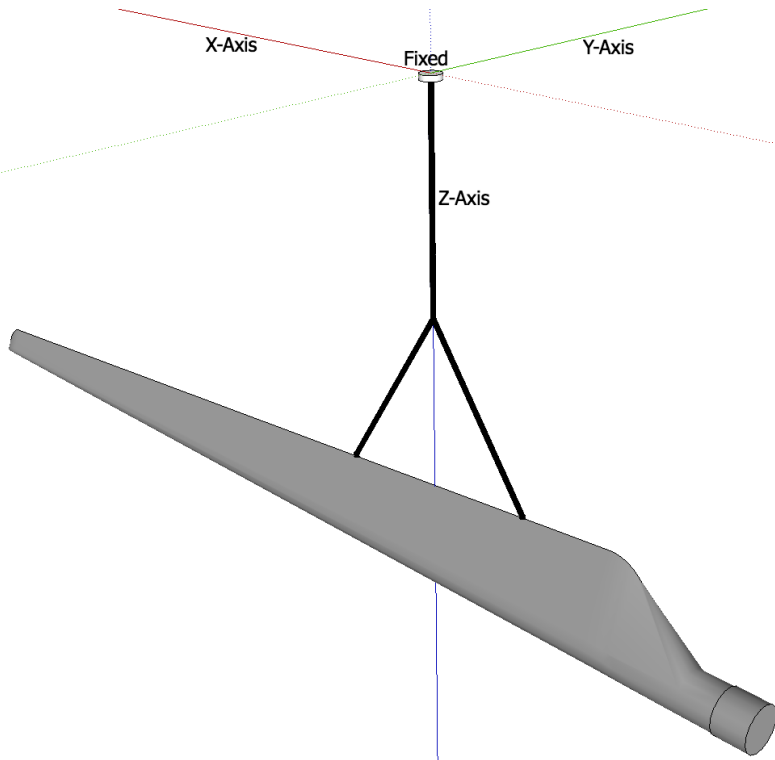


Figure 3.1: Simplified Illustration of HSBM System

3.1.2 Multibody Dynamics

Multibody dynamics (MBD) is the understanding of the motion of subsystems (bodies or components). The subsystems can be either flexible or rigid. The term *rigid body* implies that the deformation of the body under consideration is assumed small such that the body deformation has no effect on the gross body motion. The configuration of a rigid body in space can be identified by using six coordinates. Three coordinates describe the body translation, and three coordinates define the orientation of the body. If a centroidal body coordinate system is used, the translational equations are called *Newton equations*, while the rotational equations are called *Euler equations*. Newton-Euler equations, which are expressed in terms of the accelerations and forces acting on the body, can be used to describe an arbitrary rigid body motion [34]. In MBD, multiple bodies are connected with each other by hinges or joints. Figure 3.2 illustrates a multibody system, where all bodies are connected via joints and the body B_1 is defined to be the base. The degrees of freedom (DoF) of the system is defined by evaluating the DoF per body which depends on the connection between the bodies. A revolute joint reduces the DoF down to 1 in a three dimensional domain, and a ball joint leaves 3 DoF. When every connection is defined the equations of motion can be solved. If the bodies are set to be flexible, the deformations of the bodies have to be included. Due to its simplicity and adjustable degree of freedom, the computational costs can be kept low.

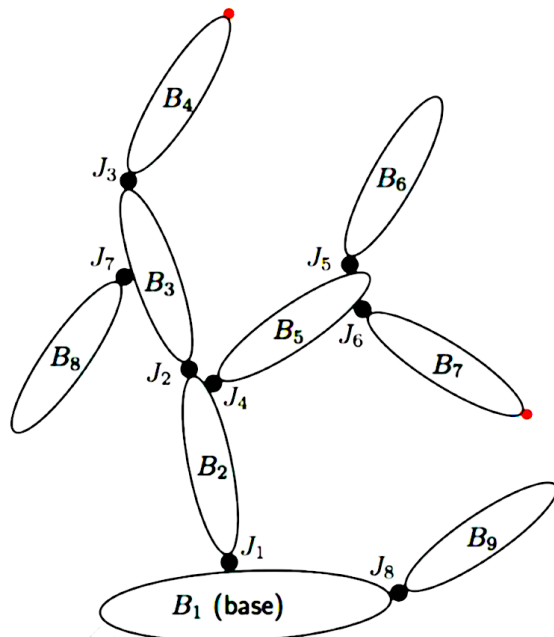


Figure 3.2: Illustration of a Multibody System [26]

In this thesis the HAWC2 code is used, developed by DTU Wind Energy, which works with a flexible multibody system and *Timoshenko* beam elements.

3.1.3 Timoshenko Beam Elements

In the HAWC2 code the structure is discretised in small Timoshenko beam elements, by Kim et al. [16], each interconnected by joints and hinges. Usually beams are model by Eulerian beams, where the cross-section remains perpendicular to the neutral plane, such that they are not capable to include buckling. A better representation can be achieved with the beams theory developed by Timoshenko [44]. A Timoshenko beam introduces more flexibility by an additional variable which states the angle between the perpendicular cross-section of the Eulerian beam and deformed beam, therefore it will take into account shear and rotation of the inertia. A graphical interpretation can be found in Figure 3.3, where Q is the shear force, M the moment and h the beam diameter.

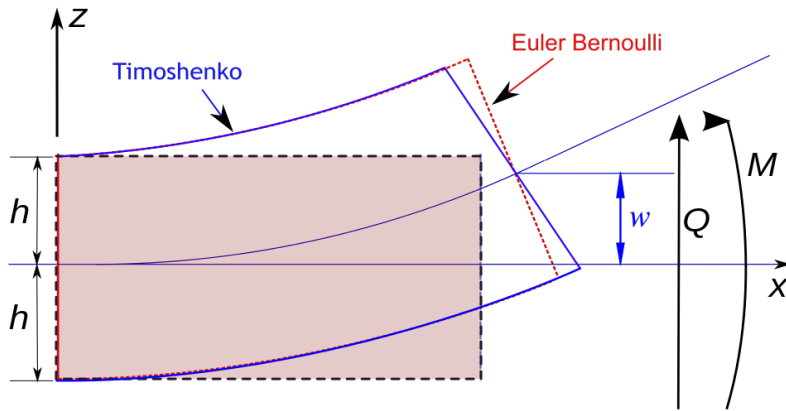


Figure 3.3: Graphical Explanation of a Timoshenko Beam Element

3.2 Aerodynamics

The second important topic is the aerodynamics and will be discussed here. The aerodynamic effects on blades and wings have been investigated thoroughly throughout many years and the loading has been determined both experimentally [3, 10, 25] as well as numerically [8, 33, 48]. These investigations provide lift- and drag coefficients for a range of angles of attack, typically -20° to 20° . However in the presented situation the blade may be lifted in orientations for which no wind tunnel measurements have been done e.g. 90° pitch and/or 90° yaw.

In the previous section the dynamics of the HSBM system has been briefly discussed. As one can imagine the motion of the blade is caused by the wind and the aerodynamic effects on the blade. In the following section the aerodynamic aspects of the system are briefly introduced. The blade needs to be able to be lifted in all possible orientations, which leads to two distinct problems: large yaw angles and large pitch angles. These two problems are investigated and theory is discussed on determining the loads in these *extreme* orientations.

Section 3.2.1 describes basic aerodynamic theory and the definition of lift and drag forces on an airfoil. This theory will be explained and used on the specified blade and situation

and discussed in Section 3.2.2. HAWC2 is based on the crossflow principle to determine the forces on the blade in yaw angles. This principle is explained and the implementation on the blade is discussed in Section 3.2.3. The previously mentioned extreme conditions lead to several flow phenomena such as flow separation caused by large pitch angles. The source of this effect is explained in Section 3.2.4 and is relevant since the blade will be subjected to highly pitched flow. Afterwards, a simple method of computing the standard deviation of the forces due to the turbulence is derived in Section 3.2.5. Finally, the method of creating a turbulence field in HAWC2 is assessed in Section 3.2.6.

3.2.1 Basic Lift & Drag Theory

Fluid flow passing the surface of a body exerts a force; lift L is the component of this force perpendicular to the flow, drag D the component of the force parallel to the flow as explained by Anderson [4] and illustrated in Figure 3.4. Lift is a result of pressure differences and depends on angle of attack, α , airfoil shape, air density, ρ , and airspeed, U_∞ . The pressure difference arises from Bernoulli's principle [4], which states that when the flow speeds up the pressure decreases. In Figure 3.4(a) a higher velocity (orange) is seen at the upper side of the airfoil corresponding with the lower pressure region (dark green) in Figure 3.4(b), hence suction and thus lift.

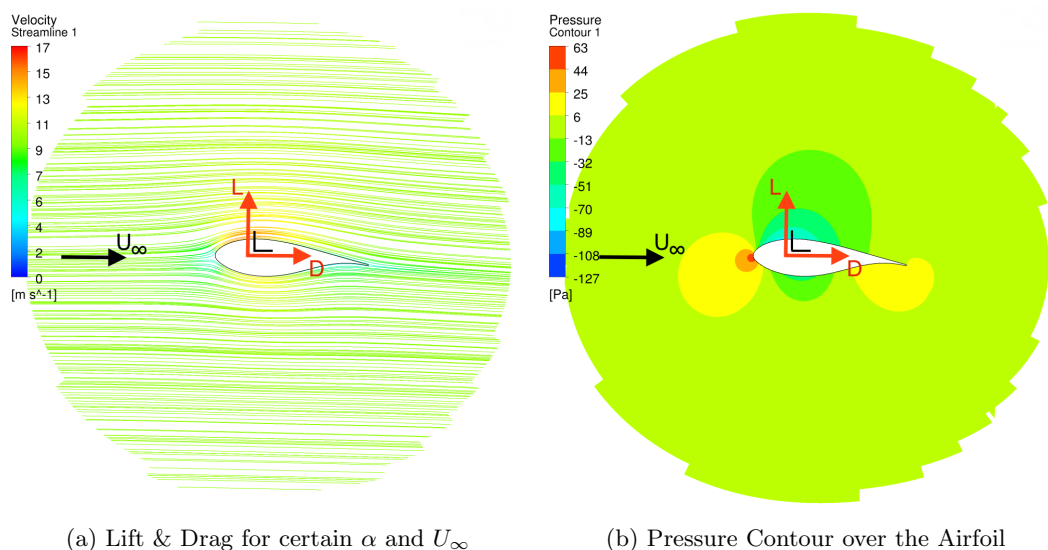


Figure 3.4: Basics Illustration of Lift, L Drag, D and Pressure Contour

The lift and drag forces are determined by numerically integrating the pressure distribution or by measurements in a wind tunnel experiment. Drag also consists of viscous forces which will later be discussed. The forces are non-dimensionalised in order to obtain a two-dimensional coefficient independent of spanwise effects used as a characteristic of a particular airfoil. For a complete wing or blade these coefficients or airfoil polars are determined per airfoil section (i.e. blade station).

Airfoil Polars

Airfoil lift, drag and moment data in the low angle of attack regime is readily available from a multitude of sources [3] as well as from modern computational approaches such as XFOIL [11]. For many applications, data in this linear regime is sufficient.

However, with the hoisting of a wind turbine blade the angle of attack may be up to 90°. Airfoils up to these angles behave in an unconventional manner and operate in the post stall region. In this study lift and drag polars are used which are created with transient 3D CFD simulations, by DTU Wind Energy, for 360°. These polars are frequently used for various scientific research papers and are considered accurate.

Furthermore research by Sørensen and Michelsen [39] and recent studies by Petrilli et al. [27] prove that 3D Reynolds-Averaged Navier-Stokes (RANS) computational analysis on airfoils and wings provides acceptable accurate post-stall forces. Experimental studies have been done for a wide range of airfoils at high angles of attack [35, 43] from which guidelines are developed for an empirical approach that predicts post-stall airfoil characteristics [41]. These findings show that after an angle of attack of 20° the lift/drag ratio at which pressure measurements were acquired essentially followed simple flat plate theory.

However, for very large wind turbine blades, the airfoil thickness, up to 40% of the chord, becomes an important factor in determining the drag at 90°. The airfoil will act more similar to an ellipse than as a flat plate. A study on non-rotating semi-span airfoils showed that the maximum drag at 90° decreases with the airfoil thickness over a range from 9 to 18% for a given aspect ratio \mathcal{A} [30]. This leads to believe that simple flat plate theory is not adequate for the accurate determination of the loading on the blade for this particular situation.

Reynolds Number

The prediction of the flow pattern in a fluid situation can be done by studying the Reynolds number, Re , which is a dimensionless quantity defined as the ratio of inertial forces over viscous forces. The number is used to characterise different flow regimes within a flow, e.g. laminar or turbulent. Laminar flow occurs at low Reynolds numbers, where viscous forces are dominant and turbulent flow occurs at high Reynolds numbers and is dominated by inertial forces, which tend to produce flow instabilities such as chaotic eddies and vortices i.e. swirling of the fluid. The Reynolds number is expressed as follows.

$$Re = \frac{\text{inertial forces}}{\text{viscous forces}} = \frac{\rho U_\infty L}{\mu} \quad (3.1)$$

Where, L [m] is the characteristic length, μ [$kg/(m \cdot s)$] is the dynamic viscosity of the fluid and ρ [kg/m^3] is the density of the fluid.

As mentioned, high Reynolds number flows tend to have chaotic eddies and vortex shedding which have great influence on the mean and fluctuations of the loading on the blade. Vortex shedding is an oscillating flow that takes place when the fluid passes a bluff body at certain velocities, depending on the Reynolds number. Vortices are created behind the body and detach periodically creating alternating low-pressure vortices. Vortex shedding

can be described by the dimensionless Strouhal number and is defined as, $St = \frac{f \cdot L}{U_\infty}$, where f is the frequency of vortex shedding.

Drag Forces

The drag force on a body in a fluid flow is usually divided into two components: frictional drag, and pressure drag. Frictional drag comes from friction between the fluid and the surfaces over which it is flowing. This friction is associated with the development of boundary layers, and it scales with Reynolds number. Pressure drag comes from the eddying motions that are set up in the fluid by the passage over the body. This drag is associated with the formation of a wake and it is usually less sensitive to Reynolds number than the frictional drag.

At $20^\circ C$ the kinematic viscosity of standard air is $15.11 \cdot 10^{-6} [m^2/s]$, with an average chord length of $5 [m]$ the Reynolds number at a wind speed of $10 [m/s]$ is $3.5 \cdot 10^6$, indicating that the flow is in the turbulent region. The blade will be assumed *streamlined* in the region of positive to negative 20° angle of attack and *bluff* in the region around 90° angle of attack. *Bluff bodies* are characterised by a more or less precocious separation of the boundary layer from their surface, and by wakes having significant lateral dimensions and normally unsteady velocity fields.

3.2.2 Mean Forces & Moments

As mentioned before, extreme pitch angles need to be examined since the hoisting of the blade is done in all possible orientations with respect to the incoming wind. Recalling the angle definition in Section 2.4.2, and illustrated in Figure 2.4, the mean forces on the blade can be divided as follows.

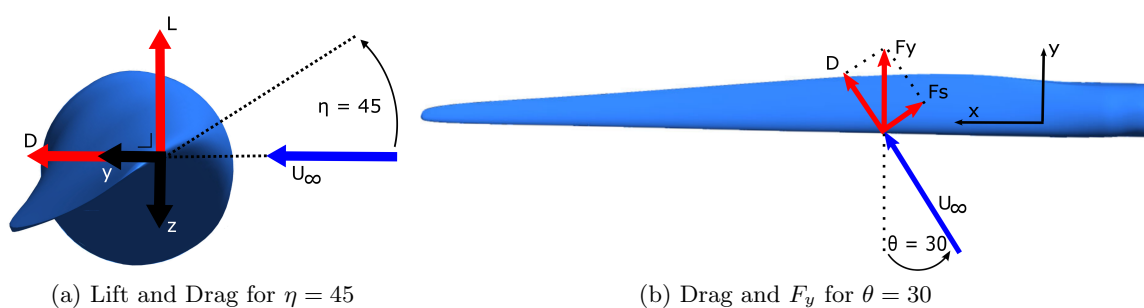


Figure 3.5: Lift and Drag Forces under Pitch Angle $\eta = 45$ and Yaw Angle $\theta = 30$

The drag force, D , is always parallel to the incoming wind, U_∞ . The lift force, L , is always perpendicular to the incoming wind and the blade span direction. In this example the pitch angle η is 45° and θ is 45° . F_s is the side force perpendicular to U_∞ . From the basic lift and drag theory explained in Section 3.2.1, the forces F_z and F_y for this specific situation can be defined as follows.

$$D = F_y \cdot \cos \theta = 0.5C_D(\eta + \xi)\rho U_\infty^2 A \quad (3.2)$$

$$L = -F_z = 0.5C_L(\eta + \xi)\rho U_\infty^2 A \quad (3.3)$$

Here F_y and F_z are the integral forces at the perpendicular flow reference condition $\nu = 0$ at the pitch angle $\eta = 45$ and yaw angle $\theta = 30$. Furthermore, C_D and C_L are the 3D drag and lift coefficient respectively, $A [m^2]$ is the area and $\xi [^\circ]$ the local angle of attack (AoA) due to the structural pitch in the blade.

The moments can be presented similarly for the same conditions, namely $\theta = \nu = 0$ at the pitch angle η .

$$M_x = 0.5C_{M,x}(\eta + \xi)\rho U_\infty^2 A^{3/2} \quad (3.4)$$

$$M_y = 0.5C_{M,y}(\eta + \xi)\rho U_\infty^2 A^{3/2} \quad (3.5)$$

$$M_z = 0.5C_{M,z}(\eta + \xi)\rho U_\infty^2 A^{3/2} \quad (3.6)$$

The coefficients $C_{M,x}$, $C_{M,y}$ and $C_{M,z}$ are the moment coefficients around the x -, y - and z -axis respectively.

3.2.3 Crossflow & Streamwise Flow

[Uranga et al. \[45\]](#) investigate the effects of crossflow on the flow transition for an infinite wing with an angle of attack of 4° and sweep angles from 0° to 60° . It is established that the crossflow cannot be decoupled from the streamwise evolution for sweep angles between about 10° and 40° due to strong non-linear interactions that take place after the laminar boundary layer separates. In the simulation of such flows with Reynolds numbers between roughly 10^3 and 10^4 , accurately predicting transition to turbulence is of crucial importance since the transition location has a significant impact on aerodynamic performance. This is linked to the fact that laminar flows have a much greater tendency to separate than the essentially turbulent flows encountered at high Reynolds numbers. When a laminar boundary layer separates in an adverse pressure gradient, triggering transition and reattachment, it forms what is known as a laminar separation bubble (LSB).

The nature of crossflow over swept wings at large Reynolds number is explained in the works by [Saric et al. \[32\]](#). Near the leading edge, the combination of pressure gradient and sweep deflects the inviscid streamlines inward (i.e. away from the tip of a backwards-sweep wing), and then outwards near the trailing edge. The boundary layer flow carries less momentum and hence this deflection is larger near the wall, which results in a secondary flow perpendicular to the inviscid streamline direction, known as crossflow. As [Saric et al. \[32\]](#) point out, crossflow instability is usually dominant near the leading edge where pressure gradients are important.

Another important consideration is that, small fluctuations in crossflow or in normal velocity can lead to large streamwise disturbances which soon become too large for non-linear interactions to be neglected. This can occur close to the stagnation point. Thus,

a flow can transition due to the growth of streamwise instabilities over swept wings and yet be destabilised by crossflow fluctuations.

Crossflow Principle

Hoerner [13] presents a very practical method to calculate the drag of wires that are inclined with respect to the airflow, see Figure 3.6. This is referred to as the crossflow principle. It can be used to estimate the drag and lift of a tube or cylinder of a given length, l , and particular cross-section, whose two-dimensional drag coefficient is known, C_d .

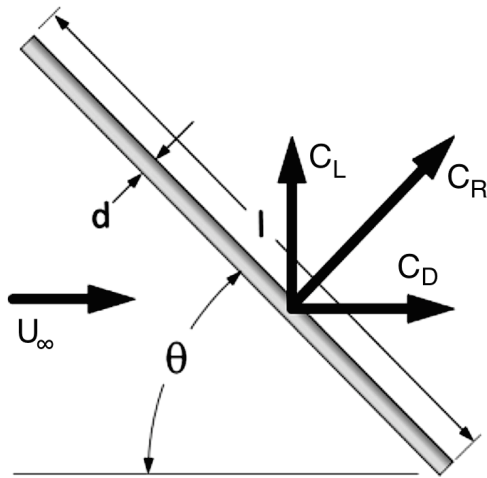


Figure 3.6: The Crossflow Principle by Hoerner

The formulation below is used to calculate the coefficients in terms of the reference wing area so it (primarily the drag) can be added directly to the miscellaneous drag coefficient. Note that the absolute sign in equation (3.9) guarantees the drag is always greater than zero. Also note that the inclination angle of $\theta = 90^\circ$ means the cylinder is perpendicular to airstream. The crossflow principle is very helpful in determining the drag of wings, aircraft components and wind turbines. The resultant, lift and drag coefficient respectively are:

$$C_R = C_d \left(\frac{l \cdot d}{S_{ref}} \right) \sin^2 \theta \quad (3.7)$$

$$C_L = C_d \left(\frac{l \cdot d}{S_{ref}} \right) \sin^2 \theta \cdot \cos \theta \quad (3.8)$$

$$C_D = C_d \left(\frac{l \cdot d}{S_{ref}} \right) |\sin^3 \theta| \quad (3.9)$$

where C_d is the 2D drag coefficient of the section in the case of perpendicular inflow, $\frac{l \cdot d}{S_{ref}}$ is the ratio to compensate for the smaller frontal area and θ is the angle of inclination, as seen in Figure 3.6. Basically, the crossflow principle states that the aerodynamic forces on a 2D structure act as if the spanwise flow velocity component was absent.

The published book on lift by [Hoerner and Borst \[14\]](#) presents that the experimental wind tunnel measurements on a straight wing section follows the simple $\cos^2 \theta$ function (i.e. the crossflow principle). This proves that the crossflow principle is a good method to predict the forces on a two-dimensional straight wing in attached inviscid flow. Therefore it has been a widely used method in research conducted in both the aeronautical and wind energy industry.

This crossflow principle is also used in the *aerodynamic model* and the *aeroelastic model* developed with the HAWC2 code. A graphical visualisation is given in Figure 3.7. Here U_∞ , in red, is the actual inflow w.r.t. the blade under a yaw angle, $\theta = 30^\circ$ and U_x and U_y are the velocity components in the x - and y -axis respectively. The principle applies to the aerodynamic forces on a wind turbine blade, where a local 2D approximation of the blade shape is acceptable.

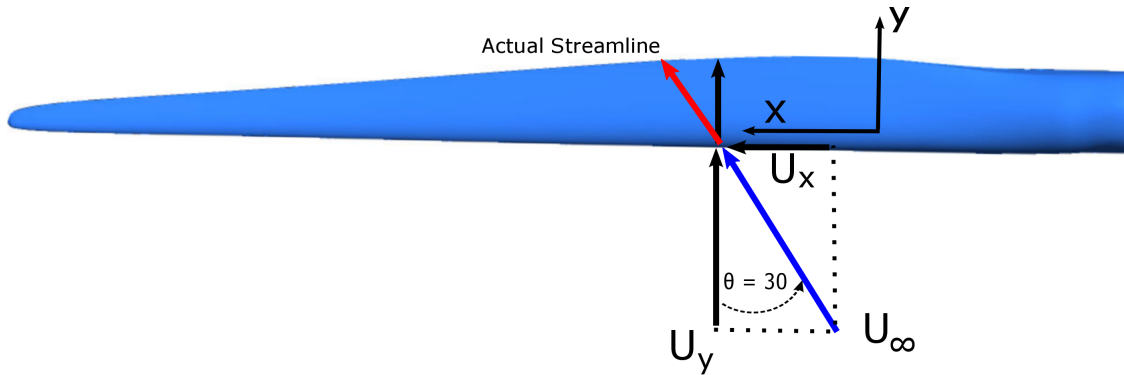


Figure 3.7: Visualisation of the Crossflow Principle in the case of HSBM

From Figure 3.7 and the fact that, $|U_\infty| = \sqrt{U_x^2 + U_y^2}$, $\cos \theta$ can be determined as follows.

$$\cos \theta = \frac{|U_y|}{|U_\infty|} = \frac{U_y}{\sqrt{U_x^2 + U_y^2}} = \frac{1}{\sqrt{1 + \left(\frac{U_x}{U_y}\right)^2}} \quad (3.10)$$

With the forces in equation (3.2) and the fact that the force as function of U_∞ times $\cos \theta$ is the same as the force as function of U_y , i.e. $F(U_\infty) = \frac{F(U_y)}{\cos \theta}$, it can be stated that,

$$D = F(U_\infty) = 0.5\rho|U_\infty|^2|c \cdot C_{y,yaw}| = 0.5\rho|U_y|^2 \left(\sqrt{1 + \left(\frac{U_x}{U_y}\right)^2} \right)^2 C_{y,yaw} \quad (3.11)$$

$$L = F(U_\infty) = 0.5\rho|U_\infty|^2|c \cdot C_{z,yaw}| = 0.5\rho|U_y|^2 \left(\sqrt{1 + \left(\frac{U_x}{U_y}\right)^2} \right)^2 C_{z,yaw} \quad (3.12)$$

where, c [m] is the chord line and $C_{y,yaw}$ [-] and $C_{z,yaw}$ [-] are the *yawed* force coefficients in y - and z -direction. Note that the z -axis is pointing into the paper according the righthand rule.

As mentioned before, the assumption in the crossflow principle is that the spanwise force can be neglected, thus $F(U_y) = F(U_\infty)$, this leads to the following.

$$0.5\rho|U_y^2|c \cdot C_d = 0.5\rho|U_y^2| \left(\sqrt{1 + \left(\frac{U_x}{U_y} \right)^2} \right)^2 C_{y,yaw} \quad (3.13)$$

Rewriting the previous equation and inserting equation (3.10) yields the following.

$$C_{y,yaw} = \frac{1}{\sqrt{1 + \left(\frac{U_x}{U_y} \right)^2}} \cdot C_d = \cos^2 \theta \cdot C_d \quad (3.14)$$

Analogously, $C_{z,yaw} = \cos^2 \theta \cdot C_l$.

Combining the cross-flow principle with the setup geometry (η is the blade pitch, $\xi(r)$ is the blade local twist as a function of the blade station, r), the local angle of attack is:

$$\alpha_{loc}(r) = \eta + \xi(r) \quad (3.15)$$

Note that the variation of angles of attack along the blade stems only from the blade twist, so it is independent of the orientation of the blade with respect to the wind. This means that, according to [Gaunaa et al. \[12\]](#), the mean integral lift and drag forces turn out to be (in the global coordinate system):

$$\bar{F} = \sqrt{1 - \sin^2 \theta \cos^2 \nu} \begin{bmatrix} -\sin^2 \nu \sin \theta & \sin \nu \cos \theta \\ \cos \theta & \sin \nu \sin \theta \\ -\sin \nu \cos \nu \sin \theta & \cos \nu \cos \theta \end{bmatrix} \begin{bmatrix} F_{y\perp} \\ F_{z\perp} \end{bmatrix} \quad (3.16)$$

Here $F_{y\perp}$ and $F_{z\perp}$ are the mean forces presented in equation (3.2), ν is the roll angle and θ is the yaw angle. Note that in case of a *clean* yawed flow ($-90^\circ < \theta < 90^\circ$) where $\nu = 0$, the forces scale with $\cos^2 \theta$ as they should according to the crossflow principle. Also in this case the non-dimensional coefficients needed for determination of the forces in the general case can therefore be determined once and for all for the wing as function of the pitch angle at the reference perpendicular condition $\nu = \theta = 0$.

Looking back at Figure 3.7 it can be seen that the assumption of neglecting the spanwise velocity component simplifies the system, however, also introduces an error. Two problems can be distinguished: **1.** Due to the absence of the spanwise velocity component the blade will not experience force in the x -direction, leading to an increasing error when subjected to large yaw inflow. Eventually the forces will become zero when $\theta = 90^\circ$, due to the $\cos^2 \theta$ law. **2.** Assuming the yawed inflow to act upon a 2D airfoil section leads to underprediction of the forces, due to the fact that the forces are calculated with a shorter chord length than the flow would actually "see". This is illustrated in Figure 3.7 where the longer *actual streamline* is indicated in blue. These two distinct problems will affect the accuracy of the final results and thus need to be validated by a high-fidelity CFD tool as discussed in Section 2.4.

3.2.4 Flow Separation

Flow separation has large effects on the drag and lift of the blade and occurs when the streamlines detach from the surface. It is caused when an increasing adverse pressure gradient, from trailing edge to leading edge, decreases the speed of the flow close to the surface, i.e. boundary layer, to almost zero. The fluid flow detaches from the surface and takes the form of eddies and vortices which in essence is swirling of a fluid. The separated flow creates a void, i.e. wake, behind the blade section of lower pressure. The fluid tends to flow into the void creating flow reversal, as seen in Figure 3.8(a).

Before the flow separates it can either be laminar or turbulent, depending on the turbulence in the flow and Reynolds number. In the case of a laminar separation the flow might transition into turbulent and reattached to the surface. The region enclosed by the separated laminar flow and reattached turbulent flow is called a laminar separation bubble, where flow reversal may be present. This phenomenon is visualised in Figure 3.8(b).

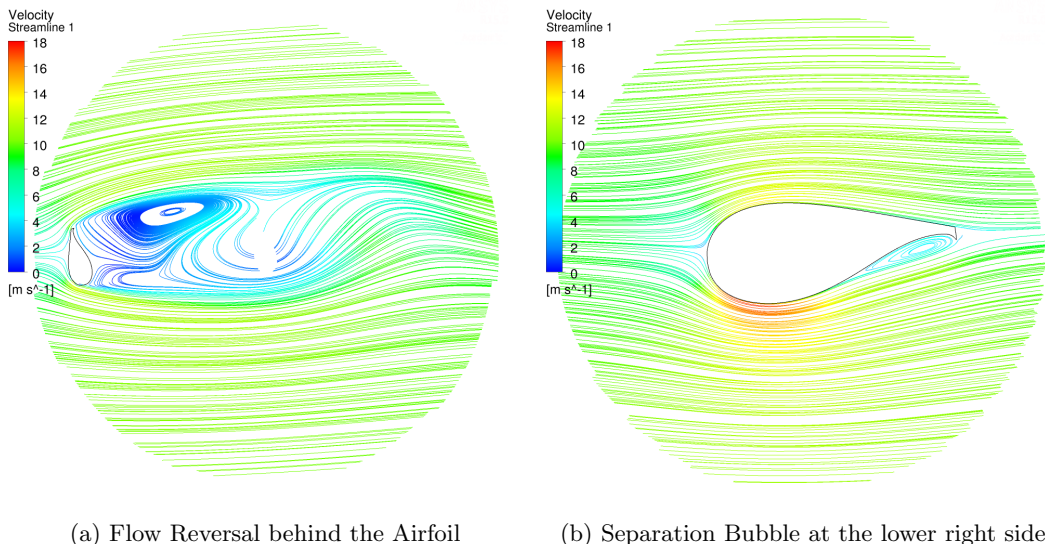


Figure 3.8: Illustration Flow Reversal and Separation Bubble

3.2.5 Standard Deviation of Forces & Moments

For single blade installation the time-varying part of the aerodynamic forces and moments is at least as important as the mean part of the loading. Time-varying loading is caused by the motion of the blade, the turbulence of the flow and the shedding of eddies. However, the considerably large weight of the complete system and the low eigenfrequency of the first modes it is argued that the main part of the load variation stems from the turbulence and vortex shedding.

In incompressible fluid dynamics dynamic pressure, q , is the quantity defined by $q = \frac{1}{2}\rho U_\infty^2$ indicating that pressure scales with the velocity according to, $p(\bar{x}) \sim U_\infty^2$. Under the following five assumptions, with the blade at a fixed position in space and constant density

and viscosity, a basic relation is obtained between the standard deviation of the forces and the turbulence.

1. Reynolds number independence
2. Wind fluctuations are described by $U_\infty(t)$, so no spatial variation, only temporal variation and no change in direction
3. A quasi-steady assumption is adequate, such that static reference data can be used
4. The unsteady loading corresponding to vortex shedding is neglected

Since the forces are mainly due to the pressure, the integral forces and moments on the blade all scale with U_∞^2 such that:

$$\bar{F}(U_\infty) = \bar{F}(\bar{U}) \cdot \frac{U_\infty^2}{\bar{U}^2} \quad (3.17)$$

$$\bar{M}(U_\infty) = \bar{M}(\bar{U}) \cdot \frac{U_\infty^2}{\bar{U}^2} \quad (3.18)$$

The velocity fluctuations can be specified using the turbulence intensity as $TI_x = \frac{\sigma(U_x)}{\bar{U}}$, where σ_x is the standard deviation (or std) in x -direction. Since $U_\infty = \bar{U} + \sigma(U)$, where \bar{U} is the mean part and $\sigma(U)$ the fluctuating part, it can be stated that $\sigma(U_x) = \bar{U} \cdot TI_x$. Taking the standard deviation σ of equation (3.17) leads to the following.

$$\begin{aligned} \sigma(\bar{F}(U_\infty)) &= \sigma\left(\bar{F}(\bar{U}) \cdot \frac{U_\infty^2}{\bar{U}^2}\right) = \bar{F}(\bar{U}) \cdot \sigma\left(\frac{(\bar{U} + \sigma(U))^2}{\bar{U}^2}\right) \\ &\dots = \bar{F}(\bar{U}) \cdot \sigma\left(\left(1 + \frac{\sigma(U)}{\bar{U}}\right)^2\right) = \bar{F}(\bar{U}) \cdot \sigma\left(\left(\frac{\sigma(U)}{\bar{U}}\right)^2 + 2\frac{\sigma(U)}{\bar{U}}\right) \end{aligned}$$

For $\frac{\sigma(U)}{\bar{U}} \ll 1$ this leads to,

$$\sigma(\bar{F}(U_\infty)) = \bar{F}(\bar{U}) \cdot \sigma\left(2\frac{\sigma(U)}{\bar{U}}\right) = \bar{F}(\bar{U}) \cdot 2 \cdot TI_x \quad (3.19)$$

This last expression indicates that the standard deviation σ of the forces is similar to the mean forces time twice the turbulence intensity. Analogously for the moments: $\sigma(\bar{M}(U_\infty)) = \bar{M}(\bar{U}) \cdot 2 \cdot TI_x$. \bar{F} and \bar{M} are the mean forces and moments as defined in Section 3.2.2, so it can be stated that the standard deviation of integral forces and moments scales linearly with density, and quadratically with wind speed. Furthermore, the standard deviation of the loading scales linearly with the turbulence intensity. These two conclusions are similar to the ones derived in the paper of Gaunaa et al. [12], although

different assumptions and methods are used. This is valuable as different methods point to similar conclusions.

This method of defining the standard deviation of the loads on the blade is a new method developed by the author. The assumption that wind fluctuations are only described by temporal variation is rather rudimentary. However, it provides a good approximation of the order of magnitude of the force fluctuations and can be used to compare with the actual variations determined by transient analysis and will be referred to as the *simplified standard deviation method*.

3.2.6 Mann Turbulence Model

Previously the importance of modelling the turbulence is discussed as it is a essential source of the fluctuations of the loading on the blade. There are numerous turbulence models either for engineering models and wind resource assessment tools (WAsP[24]) as well as for Navier-Stokes solvers as discussed later in Section 3.3.2. [Mann \[23\]](#) designed an efficient algorithm to simulate turbulent, atmospheric or wind tunnel generated wind fields. The fundamentals of the Mann model is isotropic turbulence in neutral atmospheric conditions. The energy spectrum is given based on the Von Karman spectrum, equation (3.20).

$$E(k) = \alpha \epsilon^{\frac{2}{3}} L^{\frac{5}{3}} \frac{(Lk^4)}{(1 + (Lk)^2)^{\frac{17}{6}}} \quad (3.20)$$

Where the wave number k is related to the frequency f and mean wind speed \bar{U} as: $k = \frac{2\pi f}{\bar{U}}$. The method is based on a model of the spectral tensor for atmospheric surface-layer turbulence at high wind speeds and can simulate two- or three-dimensional fields of one, two or three components of the wind velocity fluctuations. Through rapid distortion theory, by using a shear blocking Γ , the model accounts for *non-isotropic* atmospheric conditions. A Γ parameter of 0 corresponds to isotropic turbulence, whereas a higher Γ value is used for non-isotropic turbulence. It is normally recommended to use $\Gamma = 3.9$ for normal atmospheric conditions.

3.3 Computational Fluid Dynamics

In the previous sections CFD has been mentioned to solve difficult fluid flow problems and validate the *aerodynamic* model. CFD is a numerical approach of solving the *Navier-Stokes* equations. The Navier-Stokes equations will be presented and explained in Section 3.3.1 and afterwards several approaches of solving the turbulence are discussed in Section 3.3.2. In order to ensure the accuracy of the model the different numerical methods of solving the NS-equations need to be understood. These numerical methods are explained in Section 3.3.3.

3.3.1 Navier-Stokes Equations

The following section will clearly present the governing equations explain the derivation of the Navier-Stokes (NS) and the necessity of the stress tensor. Afterwards incompressibility and non-dimensionalisation will be introduced.

Conservation Laws

The derivation of the Navier-Stokes equations is realised by applying the conservation laws of mass, momentum and energy to a moving fluid:

$$\text{Mass} : \quad \rho \left(\frac{\partial}{\partial t} + \nabla \cdot \mathbf{u} \right) = 0 \quad (3.21)$$

$$\text{Momentum} : \quad \rho \left(\frac{\partial \mathbf{u}}{\partial t} + \nabla \cdot (\mathbf{u} \mathbf{u}) \right) = \nabla \sigma \quad (3.22)$$

$$\text{Energy} : \quad \rho \left(\frac{\partial e}{\partial t} + \nabla \cdot (e \mathbf{u}) \right) = \nabla \cdot (\sigma \mathbf{u}) - \nabla \mathbf{q} + \rho Q \quad (3.23)$$

Mass conservation follows from the continuity equation and the physical principle that mass can be neither created nor destroyed. Momentum conservation is based on Newtons second law $F = \frac{d}{dt}(m\mathbf{u}) = m\mathbf{a}$, which in its more general form relies on the principle that force equals the time rate of change of momentum. The body forces are omitted in the momentum equation above. The stress tensor σ represents:

$$\sigma = \begin{bmatrix} \sigma_{xx} & \sigma_{xy} & \sigma_{xz} \\ \sigma_{yx} & \sigma_{yy} & \sigma_{yz} \\ \sigma_{zx} & \sigma_{zy} & \sigma_{zz} \end{bmatrix} \quad (3.24)$$

Finally the conservation of energy entails that energy can change in form but without the possibility of being created or destroyed, known as the first law of thermodynamics. The total specific energy e [J/kg] comes from the more general fluid enthalpy $h = e + \frac{p}{\rho}$, \mathbf{q} [W/s] is the heat flux vector and Q [J/m^3] the energy generation. The stress tensor defined by normal and viscous stresses on the surface:

$$\sigma = -p\mathbf{I} + \mathbf{T}, \quad (3.25)$$

where \mathbf{I} is the identity matrix and \mathbf{T} the deviatoric stress tensor: $T = \mathbf{A}(\nabla \mathbf{u})$ with \mathbf{A} , being a viscosity tensor. Now \mathbf{T} can be expressed as:

$$\mathbf{T} = 2\mu\mathbf{E} + \mu''\Delta\mathbf{I}, \quad (3.26)$$

where

$$\mathbf{E} = \frac{1}{2}(\nabla \mathbf{u} + \nabla \mathbf{u}^T) \quad (3.27)$$

is the rate of strain tensor and $\Delta = \nabla \mathbf{u}$ the expansion rate of the flow. Now with $2\mu + 3\mu'' = 0$, the deviatoric stress tensor is expressed as

$$\mathbf{T} = 2\mu \left(\mathbf{E} - \frac{1}{3}\Delta \mathbf{I} \right) \quad (3.28)$$

Finally substituting equation (3.28) and equation (3.27) into equation (3.25) gives the expression for the stress tensor:

$$\sigma - p\mathbf{I} + \mathbf{T} = -p\mathbf{I} + 2\mu \left(\frac{1}{2}(\nabla \mathbf{u} + \nabla \mathbf{u}^T) - \frac{1}{3}\Delta \mathbf{I} \right) = - \left(p + \frac{2}{3}\mu \nabla \mathbf{u} \right) \mathbf{I} + \mu (\nabla \mathbf{u} + \nabla \mathbf{u}^T) \quad (3.29)$$

The stress tensor in equation (3.29) is one of the required constitutive relations to close this set of equations. To close the energy equation, the perfect gas law is used: $p = \rho RT$, and finally Fourier's law relates the heat variables to each other as: $\mathbf{q} = \lambda \nabla T$, where λ [$\frac{W}{mK}$] is the heat conductivity.

Incompressibility

Considering the airspeed of 10 [$\frac{m}{s}$] used in this study, the Mach number can be defined. In aerodynamics, Mach number M is a dimensionless quantity representing the ratio of fluid velocity and the local speed of sound, $M = \frac{U_\infty}{U_{sound}}$. At standard sea level conditions and a temperature of 15 degrees Celsius, the speed of sound is 340.3 [m/s] leading to a Mach number of 0.03. The Mach number is used to determine if the flow can be treated as incompressible. If $M < 0.2$, compressibility effects can be neglected and simplified incompressible flow equations can be used. In this situation $M \ll 0.2$, which simplifies the Navier-Stokes equations to the unsteady, incompressible form where there is no more need for the energy equation:

$$\nabla \cdot \mathbf{u} = 0 \quad (3.30)$$

$$\underbrace{\frac{\partial \mathbf{u}}{\partial t} + \nabla \cdot (\mathbf{u} \mathbf{u})}_{\begin{array}{c} \text{Inertia} \\ \text{Unsteady} \\ \text{acceleration} \end{array}} = \underbrace{\nu \nabla^2 \mathbf{u}}_{\begin{array}{c} \text{Divergence of stress} \\ \text{Viscosity} \end{array}} - \underbrace{\frac{\nabla p}{\rho}}_{\begin{array}{c} \text{Pressure} \\ \text{gradient} \end{array}} \quad (3.31)$$

Non-dimensional

To reduce the number of parameters and to have better comparing abilities, the next step is to non-dimensionalise the unsteady, incompressible NS-equations. This is done by division of a variable by its reference variable. Each of the variables in equation (3.31) are made dimensionless by:

$$\mathbf{u}' = \frac{\mathbf{u}}{U_{ref}} \quad x' = \frac{x}{L_{ref}} \quad \rho' = \frac{\rho}{\rho_{ref}} \quad p' = \frac{p}{\rho_{ref} \cdot U_{ref}^2} \quad t' = t \cdot f_{ref} \quad (3.32)$$

Variables with a star (\cdot) represent the dimensionless variables. The dimensionless form of the incompressible, unsteady Navier-Stokes equations is expressed as:

$$\nabla \cdot \mathbf{u}' = 0 \quad (3.33)$$

$$St \frac{\partial \mathbf{u}'}{\partial t} + \nabla(\mathbf{u}' \mathbf{u}') = -\nabla p + \frac{1}{Re} \nabla^2 \mathbf{u}', \quad (3.34)$$

where the dimensionless Strouhal and Reynolds numbers emerge, adjoining the temporal and viscous term respectively. Both the Reynolds and the Strouhal number are defined in Section 3.2.1.

3.3.2 Solving the Navier-Stokes Equations

The derivation of the Navier-Stokes equations has been shown, such that several methods of solving these equations can now be discussed. The main difference lies in the modelling of the turbulence and the computational expense. As turbulence is of great influence on the response of the dynamic system it should be investigated how these effects can be predicted and simulated. Fully modelling the turbulent fluid flow would require a Direct Numerical Simulation, other solvers make use of averaging models to include these effects.

Direct Numerical Simulation

Direct Numerical Simulation (DNS) is a solver of the Navier-Stokes equations, it resolves all scales of motion from the smallest dissipative scales (Kolmogorov scales) up to the integral scale L associated with the motions containing most of the kinetic energy [28]. Conceptually it is the simplest approach, unrivalled in accuracy and in level of description provided. However because the cost is extremely high and computer requirements increase with the cube of Reynolds number, DNS is inapplicable to high Reynolds number flows.

Reynolds-Averaged Navier-Stokes

Over the past years, Reynolds-Averaged Navier-Stokes (RANS) simulations have been widely used to predict fluid flows due to its simplicity and, to some extent, capability of prediction. Instead of studying the time-dependent flow, the time-averaged flow is analysed. This means that all scales of motion are modelled. Fully writing the gradient, ∇ , of the incompressible Navier-Stokes, presented in equation (3.34), leads to the following similar expression.

$$\frac{\partial u_i}{\partial x_i} = 0 \quad (3.35)$$

$$\frac{\partial u_i}{\partial t} + u_j \frac{\partial u_i}{\partial x_j} = -\frac{1}{\rho} \frac{\partial p}{\partial x_i} + \nu \frac{\partial^2 u_i}{\partial x_j^2} \quad (3.36)$$

Reynolds decomposition is done by writing the velocities in terms of the mean value plus a fluctuation: $u_i = \bar{u}_i + u'_i$. After substitution the Reynolds-Averaged Navier-Stokes equations are obtained.

$$\frac{\partial \bar{u}_i}{\partial x_i} = 0 \quad (3.37)$$

$$\frac{\partial \bar{u}_i}{\partial t} + \bar{u}_j \frac{\partial \bar{u}_i}{\partial x_j} = -\frac{1}{\rho} \frac{\partial \bar{p}}{\partial x_i} + \nu \frac{\partial^2 \bar{u}_i}{\partial x_j^2} - \frac{\partial \bar{u}'_i \bar{u}'_j}{\partial x_j} \quad (3.38)$$

The momentum equation can be written as following,

$$\rho \left(\frac{\partial \bar{u}_i}{\partial t} + \bar{u}_j \frac{\partial \bar{u}_i}{\partial x_j} \right) = -\frac{\partial}{\partial x_j} (\sigma_{ij} + \rho \bar{u}'_i \bar{u}'_j) \quad (3.39)$$

where σ_{ij} is the mean molecular stress defined as:

$$\sigma_{ij} = \bar{p} \delta_{ij} - \mu \left(\frac{\partial \bar{u}_i}{\partial x_j} + \frac{\partial \bar{u}_j}{\partial x_i} \right) \quad (3.40)$$

As can be seen the turbulent fluctuations act on the mean flow as if they induce an additional stress, called the Reynolds stress. We now have four equations but ten unknowns, i.e. three velocity components, the pressure, and six Reynolds stress components. Therefore a closure model is needed for the Reynolds stress. In order to evaluate the Reynolds stress tensor, a set of equations is needed to account for the transport of some turbulent quantities such as turbulent kinetic energy k and some length-scale determining equation (ε or ω). The Reynolds stress $\rho \bar{u}'_i \bar{u}'_j$ can be computed with both linear and nonlinear eddy-viscosity models or the Reynolds-stress model.

The $k-\omega$ and $k-\varepsilon$ models are most common. They represent the turbulent kinetic energy k [$\frac{m^2}{s^2}$], the dissipation rate of the turbulent kinetic energy ε [$\frac{m^2}{s^3}$] and the specific dissipation ω [$\frac{1}{s}$]. The turbulent kinetic energy k , is a measure of the kinetic energy per unit mass of the turbulent fluctuations in a flow. The dissipation ε , the rate at which k is converted into thermal energy. And finally the specific dissipation ω indicates at which rate k is converted into thermal energy per unit volume and time, sometimes also referred to as mean frequency of the turbulence.

The relation between these parameters is shown in equation (3.44) and the turbulence models are discussed in more detail in Section 5.3.

$$k = \frac{3}{2} (U \cdot TI)^2 \quad (3.41)$$

$$\varepsilon = \frac{k^{\frac{3}{2}}}{l} \quad (3.42)$$

$$\omega = \frac{k^{\frac{1}{2}}}{l} \quad (3.43)$$

$$\varepsilon = k^n \omega^m \quad (3.44)$$

where, TI the turbulence intensity [−] and l the turbulent length scale [m].

Large Eddy Simulation

In computational expense, Large Eddy Simulation (LES) lies between Reynolds-stress models and DNS, and is motivated by the limitations of both. Since large-scale motions (which are affected by the flow geometry, initial and boundary conditions are not universal) are represented explicitly by the Navier-Stokes equations, LES can be expected to be more accurate and reliable than Reynolds-stress models for flows in which large-scale unsteadiness is significant. The smaller scales (which have, to some extent, an isotropic character) are represented by simple sub-grid scale models. This in turn avoids the vast computational cost of explicitly representing the small-scale motions. However, LES still requires substantially finer meshes than those typically used for RANS calculations. Also, a LES has to be run for a sufficiently long flow-time to obtain stable statistics of the flow being modelled. This results in computational costs with orders of magnitude higher than that for steady RANS calculations in terms of RAM and CPU time.

For this investigation RANS is chosen to be most suitable due to the lesser computational effort needed compared to DNS and LES. Furthermore, the increased accuracy obtained from performing a large eddy simulation is not required in this investigation since only the mean forces are of interest. From the research of Sørensen and Michelsen [39] and literature earlier discussed, it is known that Reynolds-Averaged Navier-Stokes solvers are capable of accurately computing the loading on a wind turbine blade. The data provided by DTU Wind Energy, used as input for the HAWC2 models, is based on LES.

3.3.3 Numerical Methods

This section will explain several numerical methods used in order to solve the Navier-Stokes equation. In order to iteratively solve the NS equations the domain needs to be discretised into small finite domains. Many discretisation techniques exist and the most common commercially available is the *finite volume method*. Amongst other, *finite difference* and *finite element* are also recognised approaches.

Finite difference, historically the oldest of the three, is based upon a differential formulation of the NS equations. It is easy to implement, on the contrary, it is restricted to simple grids and does not conserve momentum, energy and mass on coarse grids. Finite element is based on the Galerkin projection. Advantages are the high accuracy on coarse grids and suitability for viscous flows. Disadvantages are the higher computational time for large problems and it is not well suited for turbulent flow. Finite volume is based upon an integral formulation of the NS equations and it has an advantage in memory usage and solution speed, especially for large problems and high Reynolds number turbulent flows. In the finite volume method, the NS equations are solved over discrete control volumes, which guarantees the conservation of fluxes through a particular control volume. For these reasons and the fact that the finite volume method is most used in CFD codes it is considered the most suitable. Using finite volume method, the solution domain is discretised into a finite number of small control volumes (cells) by a grid.

Discretisation Schemes

The discretised domain consists of a large amount of control volumes, each with a computational node and boundary nodes as illustrated in Figure 3.9. To evaluate derivative terms, values at the control volume faces are needed, this can be done with several types of discretisation schemes.

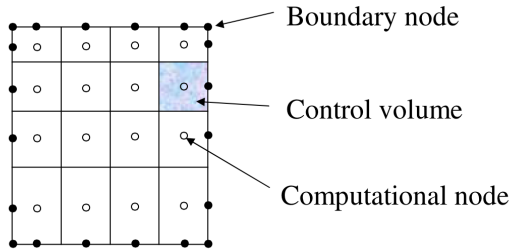


Figure 3.9: CFD Finite Volume Grid Example

1st Order UDS First order upwind scheme is the simplest numerical scheme. It is assumed that the value at the face is the same as the cell centred value in the cell upstream of the face. It is very stable, but inaccurate and very diffusive.

2nd Order CDS Central differencing scheme determines the value at the face by linear interpolation between the up- and downwind cell centred values. More accurate, but may lead to oscillations.

2nd Order UDS Second order upwind scheme determines the value from the cell values in the two cells upstream of the face. Stable and reasonably accurate.

QUICK Quadratic Upwind Interpolation for Convective Kinetics fits a quadratic curve through two upstream nodes and one downstream node. Very accurate scheme, but can lead to stability problems.

Velocity-Pressure Coupling

Considering the discretised form of the Navier-Stokes equations, the form of the equations shows linear dependence of velocity on pressure and vice-versa which is called velocity-pressure coupling. A special treatment is required in order to solve this coupling. SIMPLE provides a useful method of doing this for *segregated* solvers. However it is possible to solve the system of Navier-Stokes equations in *coupled* manner, taking care of inter equation coupling in a single matrix.

Segregated With segregated methods an equation for a certain variable is solved for all cells, then the equation for the next variable is solved for all cells, etc. The most commonly used algorithm is the SIMPLE (Semi-Implicit Method for Pressure-Linked Equations), where an algebraic equation for the pressure correction is derived, in a form similar to the equations derived for the convection-diffusion equations. It is based on the premise that fluid flows from regions with high pressure to low pressure.

Coupled With coupled methods, equations for all variables are solved for a given cell, and that process is then repeated for all cells.

Wall Functions

Near the blade or wall the flow behaves very different from far field conditions due to the strongly decreasing velocity towards the wall which inflicts friction meaning the flow becomes more dependent on the viscous terms. Accurate simulation of this boundary layer can be done by increasing the mesh density towards the wall in order to better capture the flow behaviour or by using less computational tools such as wall functions.

The required mesh density near the wall and the size of the first element is determined by the $y+$ value, which is a non-dimensional distance (based on local cell fluid velocity) from the wall to the first mesh node, as illustrated in Figure 3.10 and defined in equation (3.45).

$$y+ = \frac{u_* \cdot y}{\nu} \quad (3.45)$$

Here, u_* is the friction velocity near the wall, y is the distance to the wall and ν is the local kinematic viscosity of the fluid. The validity of using wall functions can be determined by the value of $y+$.

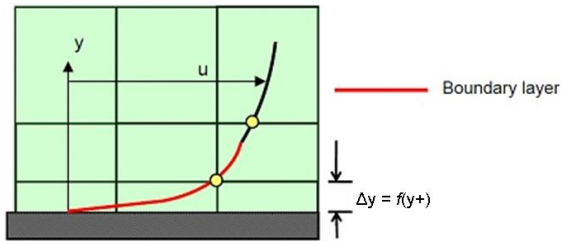


Figure 3.10: Illustration of the $y+$ value [21]

Wall functions are semi-empirical expressions that bridge the viscosity-affected region between the wall and the far field region. For an attached flow, generally wall function can be used, which means a larger initial $y+$ value, smaller overall mesh count and faster run times. If flow separation is expected and accurate prediction of the separation point is needed in order to resolve near wall effects e.g. drag prediction, as visualised in Figure 3.11, then it is advised to resolve the boundary layer all the way to the wall with a finer mesh such that $y+ < 1$.

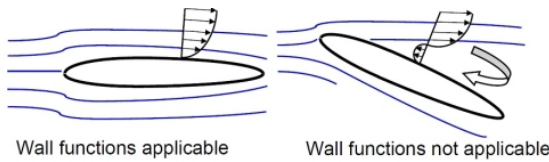


Figure 3.11: Visualisation of the applicability of Wall Function [20]

3.4 Summary

This chapter has presented relevant theoretical background on modelling the dynamic behaviour of the blade by means of multibody dynamics. In this thesis the HAWC2 code is used, developed by DTU Wind Energy, which works with a flexible multibody system and *Timoshenko* beams. Afterwards, basic understanding of computing the mean lift- and drag force on the blade are assessed. Furthermore, important aerodynamic aspects are explained in order to understand the flow phenomena arising when subjecting the blade to extreme inflow angles and turbulence. Finally, the method of determining the loading on the blade by means of computational fluid dynamics has been elaborated. The Navier-Stokes equations are derived to understand how they can be solved. The Reynolds-Averaged Navier-Stokes are used to model the turbulence due to its computationally cheap nature and reasonable accuracy for computation of the forces. Considering the numerical methods of CFD, it is evaluated that third order accurate QUICK schemes should be used due to the high precision. Moreover, coupled velocity-pressure can be used to speed up the computational time. The use of wall functions should be avoided, since they are not applicable for large pitch angles. Therefore, a $y+$ value smaller than 1 should be ensured.

Chapter 4

Aerodynamic Model

In Chapter 2 relevant research papers have been discussed regarding the aerodynamic forces on blades, subsequently Chapter 3 elaborates on the theoretical background of the dynamics and aerodynamics. The first piece in answering research question one, *1. how to model the aerodynamic forces and dynamic behaviour of a hoisted wind turbine blade in different inflow angles?* is the translation into a computational model, hence the *aerodynamic model*. This chapter performs task *one* "computing the aerodynamic forces on a blade in hoisting orientation" and explains the *aerodynamic model* which is the fundament of the later described *aeroelastic model*.

First, the HAWC2 code in which the model is developed, is clarified in Section 4.1 and subsequently the blade used in this study is presented and illustrated in Section 4.2. The aerodynamic model is set up in such a way that it resembles the later produced CFD results such that accurate comparison can be ensured, this is explained in Section 4.3. Furthermore, a straight blade is introduced in Section 4.4 which is used to test the *aerodynamic model* to the analytical solution of the crossflow principle. The results consist of the blade loading, the crossflow comparison and standard deviation of the forces, which all will be discussed and presented in Section 4.5. Finally, the model is compared and verified in Section 4.6 and this chapter is concluded with a summary in Section 4.7.

4.1 HAWC2 Setup

HAWC2 is an aeroelastic simulation tool for wind turbines developed at DTU Wind Energy [19] and is based on a multibody formulation which is a general coupling method for independent structural bodies. Each body, either rigid or flexible, is a set of Timoshenko beam elements [16] and are defined in the structural file. The motions between the bodies are defined by certain constraints which can either be a fixed joint or a bearing, making it possible to model the system of a wind turbine blade suspended from two cables. The aerodynamic model is based on the sectional force coefficients and the crossflow principle including corrections to account for unsteady and three-dimensional effects. It uses lift-

and drag coefficients from look-up tables ranging over 360° provided by DTU Wind Energy. However, when large yaw angles are introduced the crossflow principle might not be accurate in calculating the forces on the blade.

The structural model is defined in the HAWC2 .htc file. The HAWC2 input files can be found in Appendix A. The different modules and required input is discussed in this section. The user can create the bodies with the corresponding internal coordinate system and structural properties in the `main_body` section. The orientation of the body is given in the `orientation` section where each body's initial position and velocity is determined. The method of connection between the bodies, e.g. joints, bearing or fixed, is defined in the `constraint` section. Afterwards, the wind conditions and aerodynamic properties are defined in the sections `wind` and `aero` respectively. Finally, the definition of the sensors' output is done in the `output` section. The HAWC2 model will be set-up according to the simplified system of HSBM as seen in Figure 3.1. The cables will be modelled with series of Timoshenko beams.

The `wind` and `aero` section of the .htc file contain the wind conditions and aerodynamic properties respectively. In the `wind` section, the windspeed and turbulence intensity is defined as well as the `windfield_rotations` for defining the yaw angle. Afterwards the turbulence model is chosen to be a Mann model, specified in Section 3.2.6. In the `aero` section of the .htc file the link is made to the dynamic model and the aerodynamic layout and profile coefficients of the blade is given. The aerodynamic layout file holds the blade station position, chord length and thickness ratio and can be viewed in Appendix B. The profile coefficients file holds the angle of attack from -180° to 180° , lift coefficient C_l , drag coefficient C_d and moment coefficient C_m and can be viewed in Appendix C. Finally, the `aero` section includes the aerodynamic calculation method, as explained in Section 3.2, and the number of aerodynamic calculation points on the blade. In this study the blade will therefore be modelled as an infinitely stiff blade.

4.2 The DTU 10MW Blade

Due to confidentiality reasons the Siemens B75 blade cannot be used and a suited alternative is used: the 87 meter DTU Wind Energy blade for the 10MW reference wind turbine [5]. This blade is used primarily because of the extensive research data available and the similarity to the Siemens B75 blade. The airfoils used in this DTU blade are FFA[42] airfoils with relative thicknesses ranging from 21.1% to 36.0% excluding the cylindrical root part, as seen in Figure 4.1.

The structural twist in the blade ranges from -14.5° at the root to $+3.43^\circ$ at the tip and the prebend is 3.332[m]. Visualisation of the blade can be seen in the following Figure 4.2 and a detailed representation of the Gurney flap is shown in Figure 4.3. A Gurney-flap is a trailing edge device for performance improvement. Analysis done by Bak et al. [5] showed that the aerodynamic performance at the inner part of the blade increased significantly when using Gurney flaps.

As mentioned before, 3D CFD simulations were carried out to derive 2D airfoil data for a single blade at standstill. The unsteady simulations were done using the incompressible Navier-Stokes flow solver EllipSys3D on a spherical mesh with 7.8 million cells by DTU

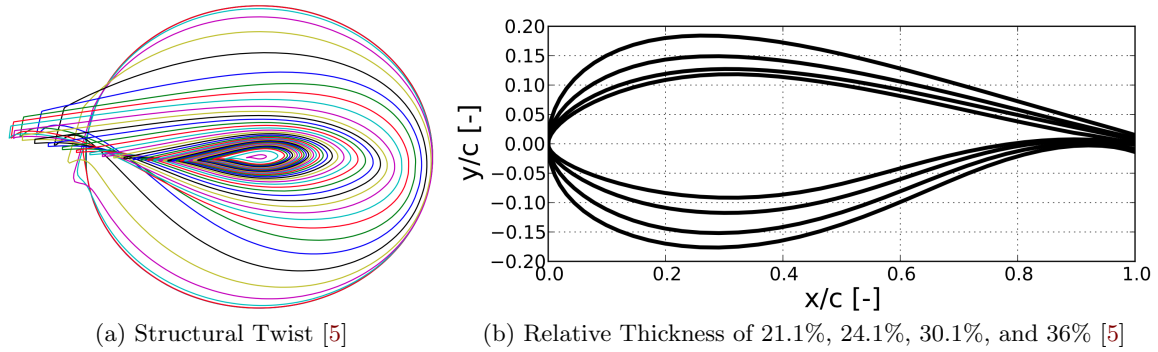


Figure 4.1: The FFA-W3-xxx airfoil series and Structural Twist Visualisation

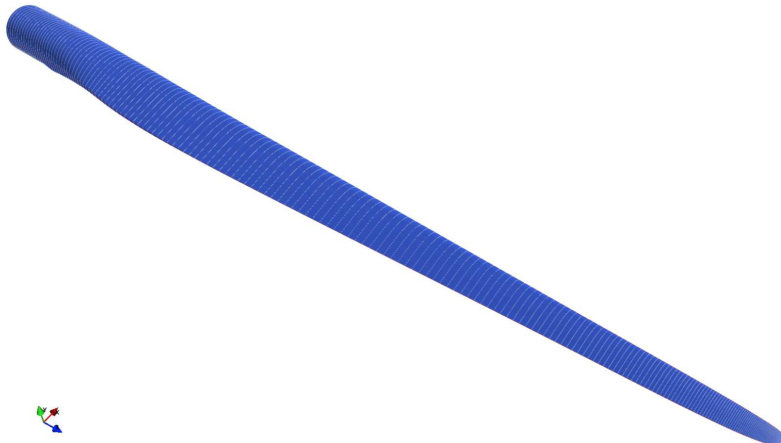


Figure 4.2: 3D Visualisation of the DTU 10MW Blade

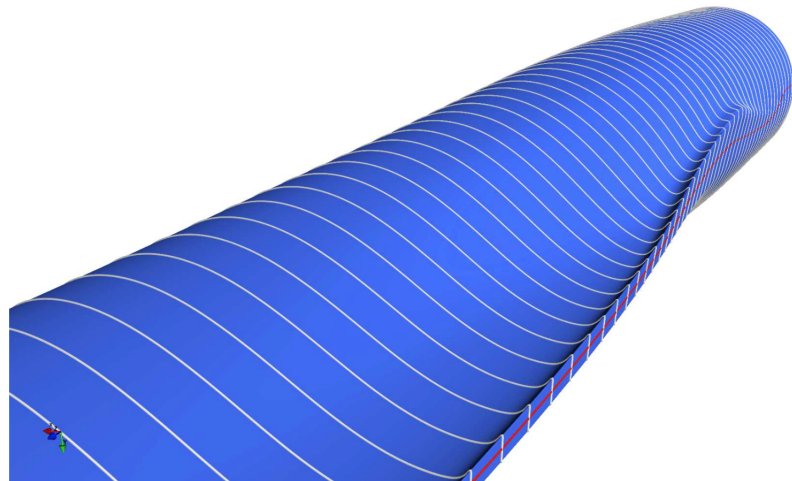


Figure 4.3: Detailed View of the Root Showing the Gurney flap

Wind Energy. The total simulation time was 100 seconds with an averaging time of 40 seconds. The turbulence was modelled using Detached Eddy Simulation to resolve the unsteady vortex shedding on the blade at standstill. The C_l - and C_d -coefficients for five

blade stations are plotted in Figure 4.4 and will be used in later discussions. Further specification on the analysis can be found in Bak et al. [5].

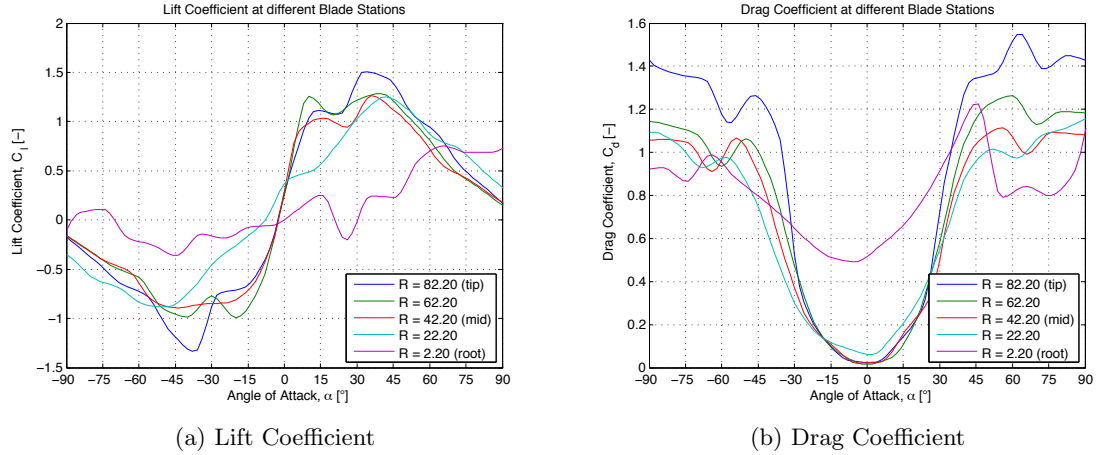


Figure 4.4: The C_l - and C_d -coefficients for several Blade Stations

4.3 Model Setup

In Section 2.4.3 the need for a static aerodynamic model is explained, namely for the ability to correctly validate the calculated forces from the aeroelastic model with the CFD model. Therefore the aerodynamic model solely consists of the blade clamped in its centre of gravity, 26.1789 meters from the root. The blade is positioned horizontal such that $\nu = \theta = \eta = 0$, thus the suction side upwards. In this orientation the $AoA = 0^\circ$ in the station with zero degrees twist and $AoA = +3.43^\circ$ at the tip station. The blade is rotated in the domain according to the global reference frame stated in Section 2.4.2, hence the y -axis always points perpendicular to the blade, the z -axis point downwards to ground and the x -axis points according to the righthand rule in spanwise direction towards the tip.

In the HAWC2 model the pitch angle η is changed by rotating the blade around the spanwise x -axis and the yaw angle θ is changed by rotating the velocity vector U_∞ around the z -axis. In Figure 4.5 an example is illustrated where the blade is subjected to an incoming wind U_∞ under a yaw angle $\theta = -45$ while the pitch and roll remain zero such that, $\nu = \eta = 0$.

The blade consists of 50 blade stations each with a specific airfoil and corresponding 2D airfoil polars, i.e. C_d , C_l and C_m . By means of equation (3.2) the forces and moments in three directions, according to the reference frame in Figure 2.4, are calculated for the entire blade. In this case the aerodynamics are looked up independently at each blade station, using the steady aerodynamic input from 3D Transient CFD analysis done by DTU Wind Energy, and a Beddoes-Leishmann dynamic stall model. In order to use HAWC2 for this application disabling of the Blade Element Momentum (BEM) based rotor aerodynamics is required and thus the calculation method is reduced to the equation (3.2) to equation (3.6). In the research paper of Gaunaa et al. [12] it is proven that simplifying

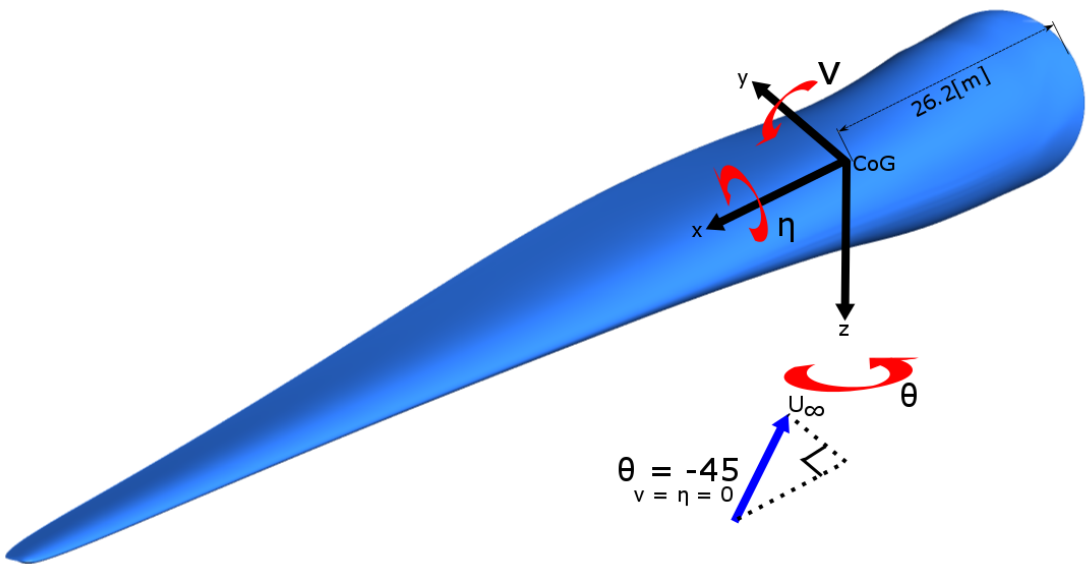


Figure 4.5: Illustration of the Reference Frame in HAWC2

the system by assuming an infinitely rigid blade returns a valid approximation of the structural response only if the rigid motions that the blade will undergo during mounting (e.g. from dangling of the yoke) have prevailing frequencies which are lower than 0.4 [Hz].

The steady simulations are performed in uniform flow, and for turbulent wind fields generated using Mann's model, see Section 3.2.6. The default configuration used to compare with the *CFD model* considers a mean wind speed of $10 \frac{[m]}{[s]}$, and a turbulence intensity of 0.16 [-], representative of an offshore site.

The forces and moments will be defined in the global reference frame. Note that the drag, as known from basic aerodynamics on an airfoil, is parallel to the incoming wind and the lift perpendicular to the incoming wind. Hence, for $\theta = 0$ the drag is similar to the force in y -axis and lift similar but negative to the force in z -axis, thus $D_{\theta=0} = F_y$ and $L_{\theta=0} = -F_z$.

For $\theta \neq 0$ and $\eta \neq 0$ the lift force L remains similar to $-F_z$ since the incoming wind is always horizontal. Furthermore, for $\eta \neq 0$ and $\theta = 0$ the drag force D remains identical to F_y . Finally, for $\theta \neq 0 \rightarrow D = F_y \cdot \cos \theta$.

4.4 Straight Blade

The DTU 10MW wind turbine blade is highly bent, as seen in Figure 4.6, moreover it is not only prebend in the flapwise direction, it is also slightly bent in the edgewise direction. This geometric prebend in the blade makes it a much more complex shape and thus strongly changes the flow behaviour. This potentially plays a significant role and might lead to a different behaviour than expected in the orientation where the blade is subjected to large yaw angles, $45 < \theta < 135$, compared to a straight blade. The crossflow principle, explained in Section 3.2.3, at the basis of the *aerodynamic model*, considers a straight blade or cylinder with certain stations and corresponding force coefficients. However, in

the case of a non-straight blade, each blade station might experience a different inflow angle or yaw angle θ , leading to non-zero lift-, drag and spanwise forces for $\theta = 90$, which should be the case according to the crossflow principle. In order to accurately and confidently argue that the model behaves according to the crossflow principle, a straight blade is introduced and tested. This straight blade has similar blade stations, airfoils and length, as well as, twist angle. However, the aerodynamic centres of all the airfoil are perfectly aligned. The analysis of the straight blade compared to the real prebend blade is discussed in Section 4.5.

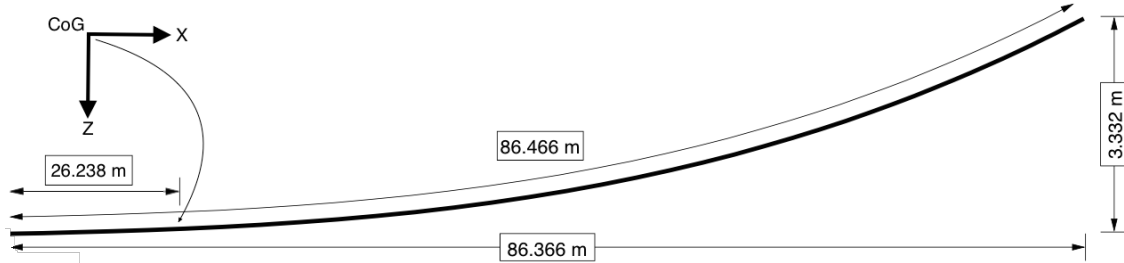


Figure 4.6: Representation of the Blade Length and Prebend

4.5 Results & Discussion

This section will present the output and results of the *aerodynamic model* in HAWC2. First in Section 4.5.1 the forces and moments for the range $-90 < \theta < 90$ and different pitch η angles are presented. This provides a good visualisation of what physically happens when pitching or yawing the blade. Afterwards, Section 4.5.2, compares the forces and moments of the DTU blade with the analytical solution of the crossflow principle, \cos^2 , as well as the straight blade introduced in Section 4.4. Finally, in Section 4.5.3 the *simplified standard deviation method* derived in Section 3.2.5 will be verified with the *aerodynamic model*.

4.5.1 Forces & Moments on the Blade

Figures 4.7, 4.8 and 4.9 present the forces and moments in x -, y - and z -direction for $-90 < \theta < 90$ and $\eta = -90, -45, 0, 45, 90$. Note that the global reference frame is not fixed to the blade such that F_x is always the force in spanwise direction, the drag $D = F_y \cdot \cos \theta + F_x \cdot \sin \theta$ and F_z is always minus the lift force. Similarly, M_x is the pitching moment, M_y is the rolling moments and M_z is the yawing moment.

Figure 4.7(a) shows the spanwise force, interesting is the fact that -45° and 45° pitch induce a larger force in x -direction than -90° and 90° . This is explained by the fact that the blade has a structural pitch or twist angle of almost 45° from root to tip, in $\eta = \pm 45$ the blade is pitched such that the spanwise force is largest.

Figure 4.7(b) shows the force in y -direction. F_y is the force perpendicular to the blade, however the drag force is always parallel to the wind, leading to: drag $\cdot \cos \theta = F_y$. As

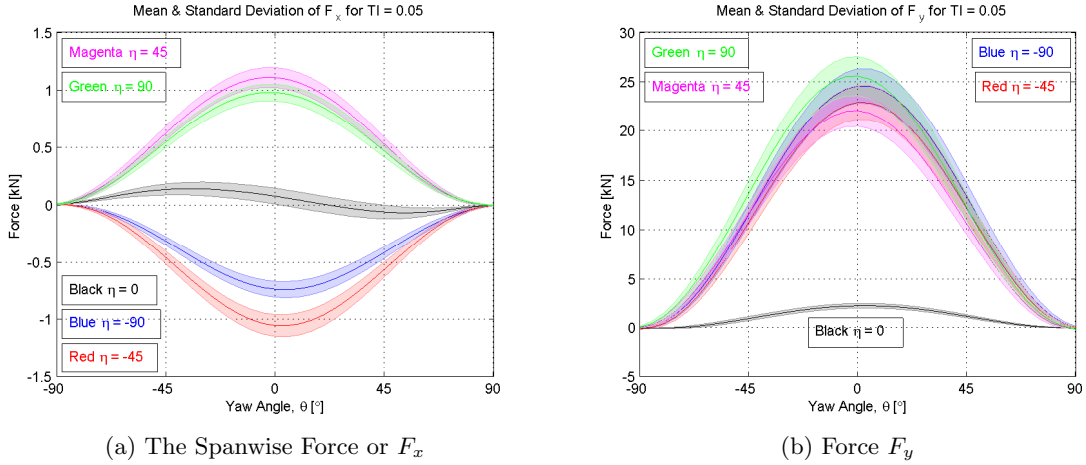


Figure 4.7: Mean and Standard Deviation of Forces F_x and F_y for varying η and θ with $TI = 0.05$

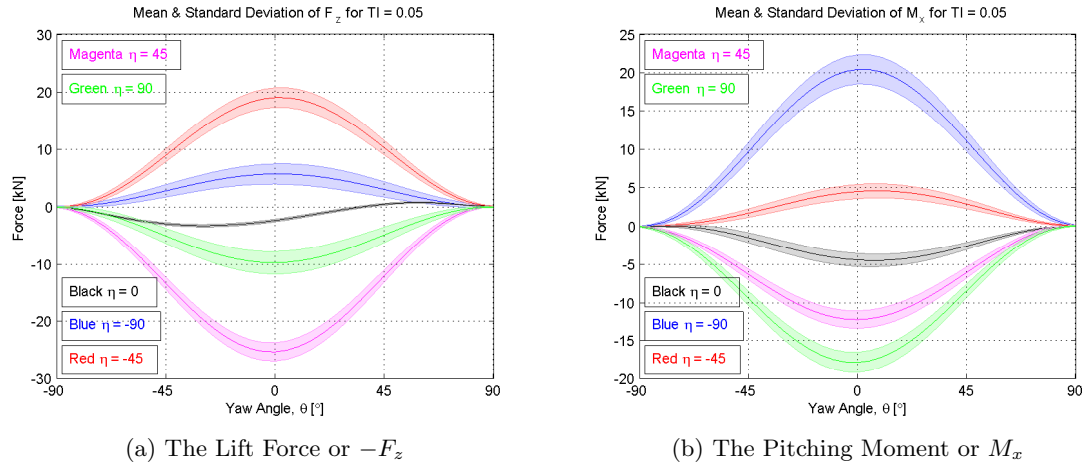


Figure 4.8: Mean and Standard Deviation of Force F_z and Moment M_x for varying η and θ with $TI = 0.05$

expected the force is largest for the blade with no yaw and $\pm 90^\circ$ pitch, however due to the strong twist angle, F_y is already large for $\eta = \pm 45^\circ$.

Figure 4.8(a) illustrates the force in z -direction which is similar to minus the lift force since the z -axis is positive downwards. Positive pitch or pitching up increases this lift force as expected. The lift force is largest for $\eta = \pm 45^\circ$, since the flow will separate in larger pitch angles, leading to lift decrease and drag increase.

Figure 4.8(b) presents the pitching moment of the blade. M_x is largest when the blade has its largest frontal area, i.e. $\eta = \pm 90^\circ$, which agrees with the theory. Figure 4.9(a) shows the rolling moment around the y -axis. Again it is noticeable that the moment is largest for $\eta = \pm 45^\circ$ corresponding with the lift force. Figure 4.9(b) presents the yawing moment or M_z which clearly is also largest for larger η .

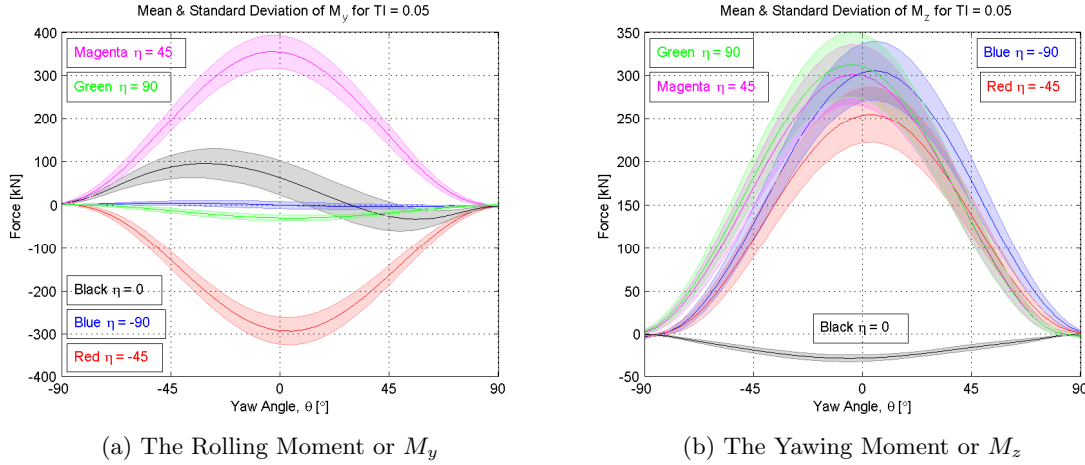


Figure 4.9: Mean and Standard Deviation of Moments M_y and M_z for varying η and θ with $TI = 0.05$

As already explained in Section 3.2.5 the time-varying part of the forces is at least as important as the mean part. In all images in Figures 4.7, 4.8 and 4.9 the standard deviation, std, has been displayed above and below the mean value. The standard deviation of the forces stem from the turbulence in the incoming windspeed. The turbulence is created using the Mann model and takes into account changes in flow direction as well as changes in velocity magnitude. More information of the Mann turbulence model can be found in Section 3.2.6.

The std is higher for pitch angles, η , that return higher aerodynamic mean forces. However higher std in the force also occurs for cases with lower mean values in some cases. This can be explained by changes in angle of attack along the blades, which in the cases with high force coefficients slopes result in higher unsteady loading.

4.5.2 Comparison with Crossflow principle & Straight Blade

Figures 4.10, 4.11 and 4.12 compare the results from the DTU 10MW blade with the analytical solution of the crossflow principle, $\cos^2 \theta$ and the straight blade. The first Figure 4.10(a) shows the spanwise force. It is seen that a spanwise force exists which should not be the case considering the crossflow principle. This is caused by the prebend of the blade and it is later seen that when introducing the straight blade from Section 4.4 the model agrees with the analytical solution. The analytical solution, in light blue, is zero for all yaw angles θ , which agrees with the crossflow principle, explained in Section 3.2.3, that assumes that the spanwise force can be neglected.

Figure 4.10(b) shows F_y , which resembles the crossflow principle for all angles. Furthermore, in Figure 4.11(a) the lift force is identical to the \cos^2 rule for all angles but $\eta = 0^\circ$, the green line. As previously mentioned, when introducing the straight blade for $\eta = 0^\circ$ from Section 4.4, it perfectly matches the analytical solution (black and purple line respectively), indicating that the crossflow principle does as expected. Nevertheless it also reveals the strong effect of the prebend of the blade on the forces.

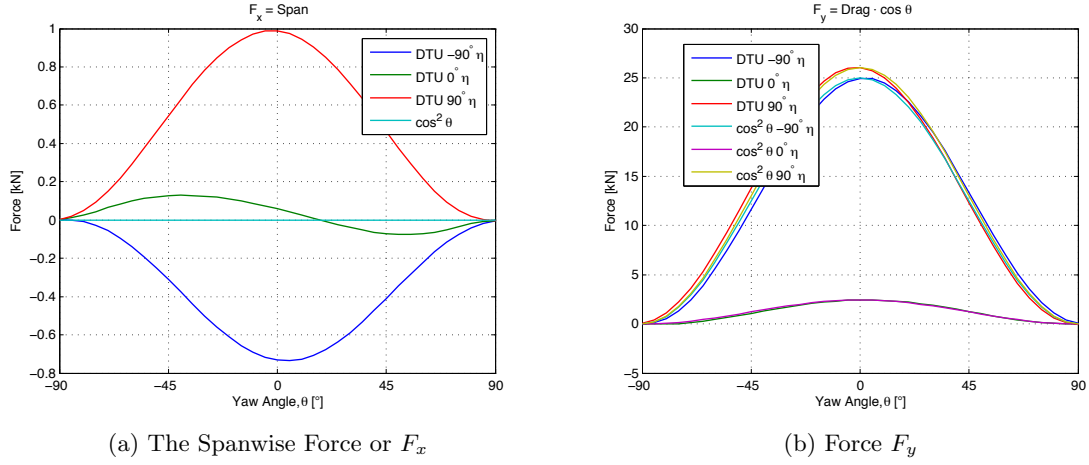


Figure 4.10: F_x and F_y Comparison with the Crossflow Principle, \cos^2 , and the Straight Blade

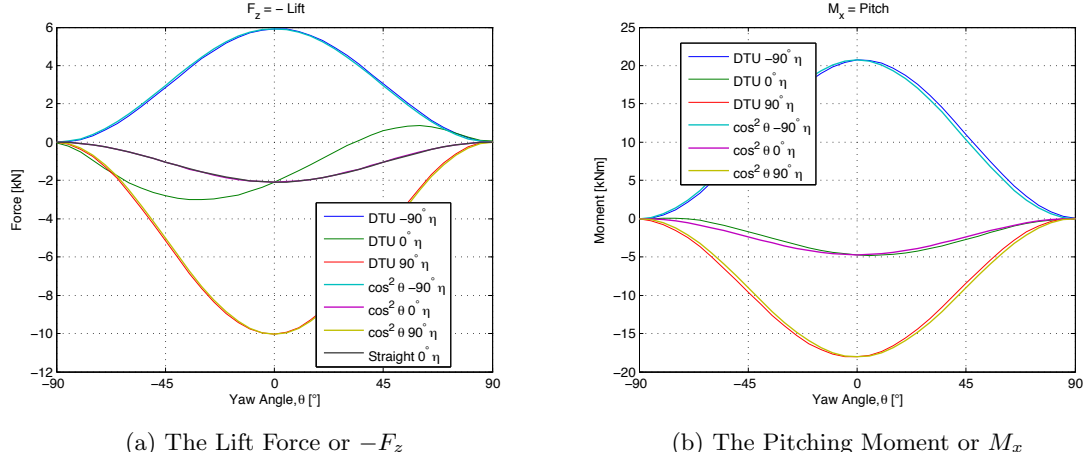


Figure 4.11: F_z and M_x Comparison with the Crossflow Principle, \cos^2 , and the Straight Blade

The pitching moment, in Figure 4.11(b), is in very good agreement with the analytical solution. In Figure 4.12(a) only the rolling moment in $\eta = 90^\circ$ agrees with the \cos^2 rule, however when introducing the straight blade, it is identical to the principle. Similar with the yawing moment in Figure 4.12(b) where for all cases only the straight blade resembles the crossflow principle.

4.5.3 Standard Deviation

From the *simplified standard deviation model* explained in 3.2.5 it is seen that the standard deviation of the aerodynamic loads scales linearly with the turbulence intensity, TI . This hypothesis is verified with the *aerodynamic model* in a 3D turbulent wind field using the Mann turbulence model, see 3.2.6. The results in Figure 4.13(b) confirm an approximate linear dependency of the standard deviation of the aerodynamic loads with the turbulence intensity. The slope is steeper for the lift force $-F_z$ than for the drag force F_y , caused by

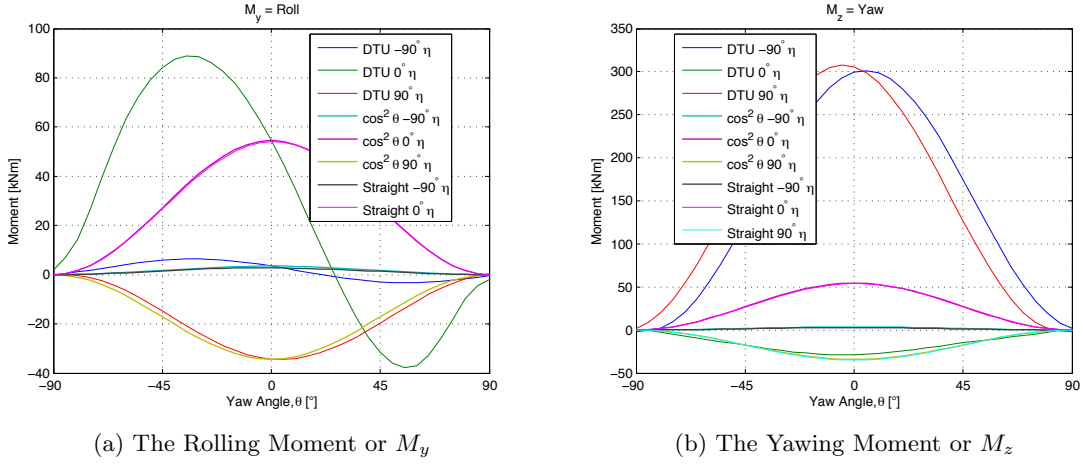


Figure 4.12: M_y and M_z Comparison with the Crossflow Principle, \cos^2 , and the Straight Blade

changes in angle of attack along the blade from the turbulence. To elaborate, at $\eta = \theta = 0$ hence $\alpha \approx 0$, the lift coefficient slope of $-F_z$ is higher resulting in higher change of loading with varying AoA. On the contrary, the drag coefficient slope of F_y for $\alpha \approx 0$ is flatter leading to small change in loading with varying AoA. This effect is clearly seen in Figure 4.13(a). For the lift-, drag- and moments coefficients see Figure 4.4 in Section 4.2.

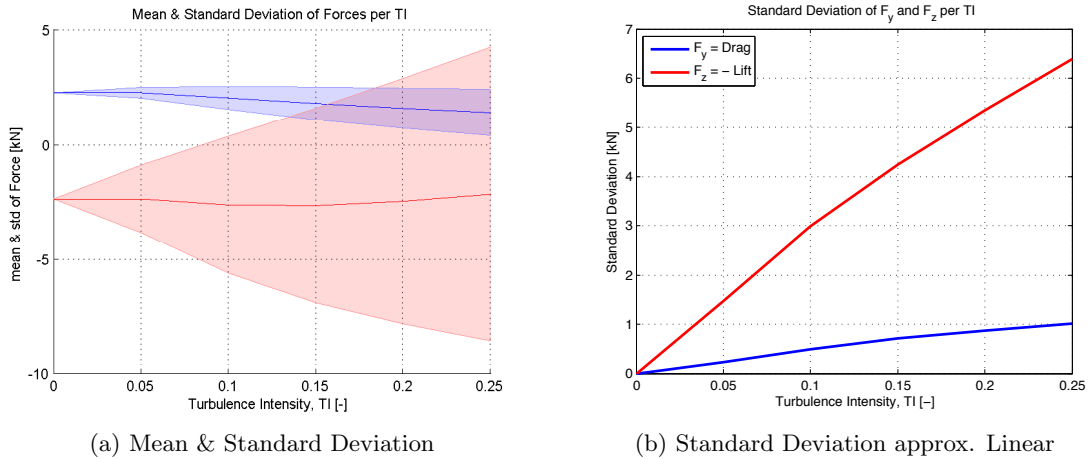


Figure 4.13: Mean & Standard Deviation of the Forces for Different TI at $\eta = \theta = 0$

4.6 Verification

The previously introduced article by Gaunaa et al. [12] developed a similar model in HAWC2 in order to predict the static forces during hoisting of the DTU 10MW reference wind turbine blade. This HAWC2 model has been validated with a simple engineering model. The work characterises the first-order aerodynamic and aeroelastic behaviour of a

single blade installation system, where the blade is grabbed by a yoke, which is lifted by the crane and stabilised by two tacklines, similar to the procedure done by Siemens WP. The results from the *aerodynamic model* created in this thesis study and presented in the previous Section 4.5 are compared with the HAWC2 analysis from [Gaunaa et al. \[12\]](#) in order to provide a verification of the developed model. Since both the model by [Gaunaa et al. \[12\]](#) and the one developed by the author are based upon the same aerodynamic principle and both designed in HAWC2, the model by [Gaunaa et al. \[12\]](#) turned out to be identical to the *aerodynamic model* to such extent that comparison is pointless and thus is not done to ensure conciseness.

Three phenomena observed from the *aerodynamic model* can be verified with an analytical expression in order to determine the validity of the developed model. First, from Section 3.2.2 and the paper by [Gaunaa et al. \[12\]](#) it is known that the aerodynamic forces and moments on the blade, and thus also its standard deviation, scale with ρU_∞^2 which is verified in the *aerodynamic model* and shown in Figure 4.14. Secondly, the fact that the standard deviation of forces and moments scale linearly with turbulence intensity, as derived in Section 3.2.5 and seen in Figure 4.13. And thirdly, the mean aerodynamic forces and moments scale with the square cosine of the wind yaw angle, as derived in equation (3.14) and displayed in Figure 4.10 with the straight blade. These three verifications clearly show that the *aerodynamic model* behaves as expected.

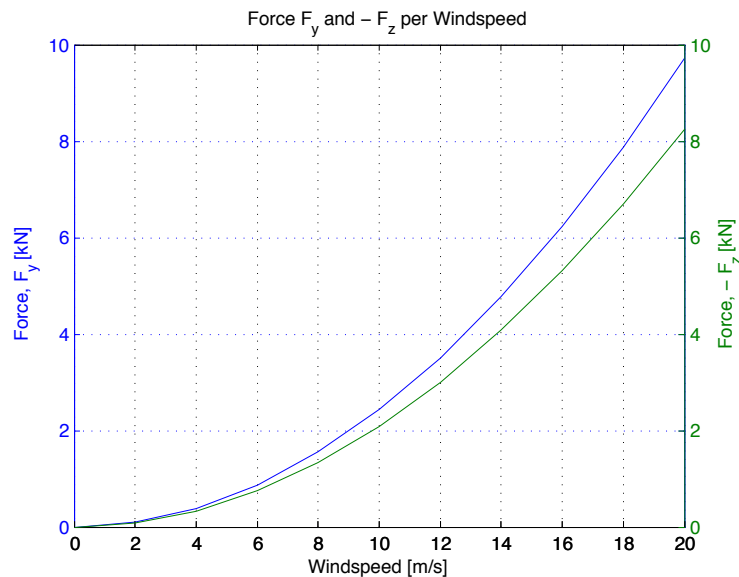


Figure 4.14: Forces Scale Quadratically with the Windspeed

[Wang et al. \[46\]](#) calculate the hoisting forces of a 1.5 MW wind turbine rotor with the aeroelastic tool GH Bladed. This article is used to compare the trend of the forces for different pitch and yaw angles. The results can merely be compared by means of extrema since the model of [Wang et al. \[46\]](#) could not be used by the author. The maximum drag is seen at $\eta = \pm 90$ and $\theta = 0$ for both models and the maximum span and lift also agree at $\eta = \pm 45$ and $\theta = 0$. The minimum forces are seen at $\theta = \pm 90$ according to both models. More comparison could not be done due to the fact that the blade is smaller and has a different geometry. However, this comparison shows good agreement which

simply provides the author and the reader with verification of the order of magnitude and confidence in the developed model. It should be noted that the GH Bladed software is also based upon the crossflow principle, which will later be tested by means of a computational fluid dynamics analysis.

4.7 Summary

This chapter has presented the developed *aerodynamic model* which is used to find an answer to the first research question, **1. how to model the aerodynamic forces and dynamic behaviour of a hoisted wind turbine blade in different inflow angles?**.

The model based on the crossflow principle is able to calculate the mean forces and moments as well as the standard deviation for yaw and pitch angles every 5° . It is found that the large prebend in the blade causes a small spanwise force to be computed by the model. When introducing a similar straight blade it is demonstrated that the *aerodynamic model* does not compute any forces. Therefore it can be concluded that the prebend of the blade plays an important role, such that the blade cannot be approximated as being straight. However, the theory in HAWC2 is a straight implementation of the crossflow principle, which is clearly shown by the comparison of the straight blade with the $\cos^2 \theta$ rule.

Furthermore, it is verified that the forces scale quadratically with the windspeed and that the standard deviation of the forces scales linear with the turbulence intensity, complying with the theory. Finally, the aerodynamic model is verified with the models by [Gaunaa et al. \[12\]](#) and [Wang et al. \[46\]](#).

This however does not completely answer the first research questions since the validity of the crossflow principle should be verified, which will be done in the following Chapter 5 by means of computational fluid dynamic analysis.

Chapter 5

Computational Fluid Dynamic Model

As previously explained the HAWC2 code based *aerodynamic model* has a limited accuracy when considering the aerodynamics due to the fact it can not handle large yaw angles and nonlinear effects. In order to answer the first research question, **1. how to model the aerodynamic forces and dynamic behaviour of a hoisted wind turbine blade in different inflow angles?**, the validity of the crossflow principle should checked. For this reason the *aerodynamic model* will be validated with a high-fidelity computational fluid dynamic (CFD) model based on the Navier-Stokes equations in the commercial package ANSYS Fluent. In Section 3.3.1 the basics of the Navier-Stokes equations are introduced and different types of solvers are discussed. This part will discuss the developed *CFD model* and perform task two "validate the obtained results with a high-fidelity model".

This chapter starts off with a short explanation of the chosen CFD code, in Section 5.1. A mesh study in order to ensure high accuracy and grid independency is done in Section 5.2 followed by a detailed explanation of the setup of the model in Section 5.3. The results will be discussed in Section 5.4, including the comparison with the *aerodynamic model* as well as analysis of the discrepancies. Verification of the model will be done in Section 5.5 and finally the findings are summarised in Section 5.6.

5.1 ANSYS Fluent

A great variety of CFD codes exists. A few commonly used solvers are briefly discussed in order to justify the solver choice made.

OpenFOAM is a library of C++ routines that facilitates the numerical solution of partial differential equations. Applications range from laminar incompressible flow to fully turbulent reacting compressible flow. OpenFOAM is freely available under the GNU Public License which is advantageous since license are something difficult to obtain. For post-processing, the distribution comes with a version of ParaView.

COMSOL Multiphysics is a finite element solver and capable of simulating various physics and engineering applications, especially coupled phenomena, or multiphysics. The ability

of coupling physics make it interesting as the current thesis study includes the coupling of aerodynamics and dynamic response. As discussed in Section 3.3.3 the finite element method is not suited for this study due to the higher computational time needed and the fact that a high Reynolds number flow (i.e. more turbulence) is studied.

Both of Fluent and CFX solvers come as integrated packages with post-processing. CFX is now integrated into the ANSYS Workbench, which allows user to take advantage of its vast structural analysis capability as well. CFX is a very powerful compressible solver, however since this fluid problem is fully incompressible CFX is not suitable. Fluent is an extremely versatile code that has probably been applied with success to more classes of flow than any other. Unlike CFX, Fluent has a great speed of calculations. Fluent solves partial differential equations on an unstructured mesh and the spatial discretisation of the equations is based on the *finite volume method* as explained in Section 3.3.3.

A finite volume solver is chosen due to the advantages that mass, momentum and energy are conserved even on coarse grids and that it is very efficient. Many finite volume codes exist, however ultimately, Fluent is chosen in alignment with Siemens Wind Power to ensure the model can be used for following investigations. Furthermore, Fluent is a well-documented and often scientifically referenced code.

5.2 Mesh Study

With computational fluid dynamics the Navier-Stokes equations are solved in a domain which holds the geometry. It is of great essence that the domain is large enough to eliminate any effects from the boundary conditions. The spherical domain created for this study has a radius of 500 meters. Given the blade of 87 meters, the domain is in spanwise direction more than ten times the blade and approximately hundred times in chordwise direction, which is considered sufficient. The domain is discretised in a large number of small finite volumes, this is called the grid or mesh. The quality of the mesh greatly influences the stability of the solution and accuracy of the results. The quality of the mesh can be checked with certain parameters such as aspect ratio and element skewness. In Table 5.1 these parameters are summarised and are within the acceptable limits.

Table 5.1: Various Parameters Indicating Mesh Quality

Parameter	Mesh G3		Mesh G2		Mesh G1	
Elements	172,032		1,376,256		11,010,048	
	Max	Min	Max	Min	Max	Min
Aspect Ratio	297,093	1	379,043	1	445,027	1
Skewness	0.77	0.002	0.69	0.0006	0.68	0.0003

Besides these parameters, the mesh density or number of volume elements, is a main driver for the solution accuracy. To ensure that the results are independent of a change in mesh density, it is needed to perform a mesh independence study. In general, as the number of cells grow, i.e. if the mesh becomes finer, the solution should increase in accuracy. This is caused by the fact that the flow is solved on a smaller scale and thus better resembles the reality. Once the solution does not change within a predefined value, the solution can be

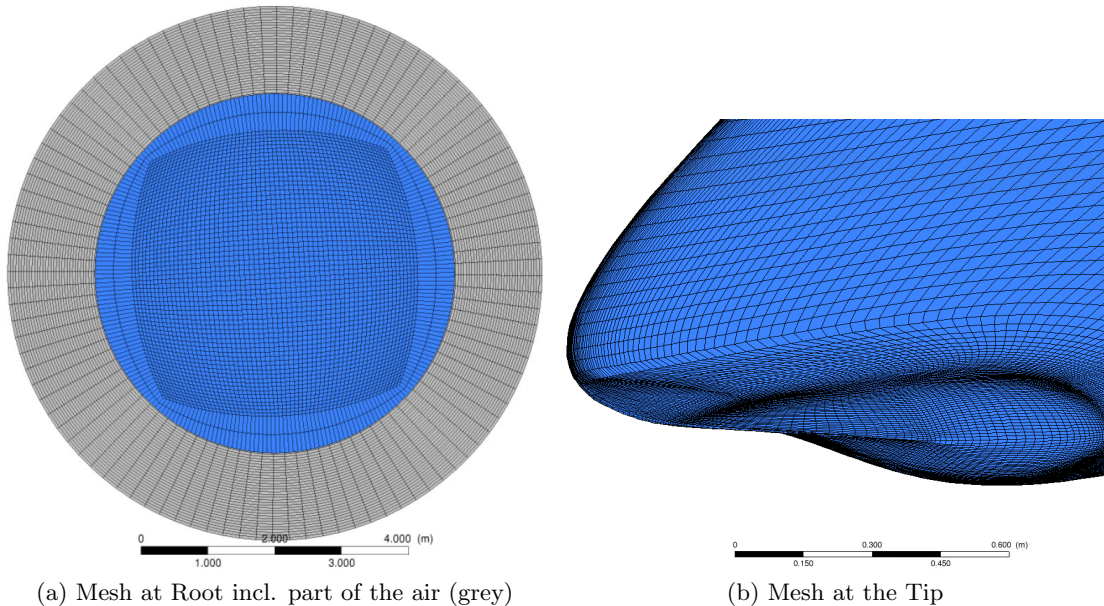


Figure 5.1: Indication of the Mesh Density of G1, note the Length Scale

considered converged with respect to the mesh. Richardson extrapolation is a technique to estimate the grid independent value for the lift, drag, etc. This is elaborated in Section 5.2.1.

5.2.1 Richardson Extrapolation

The purpose of the *Richardson extrapolation* is to produce high accuracy results by means of general formulae. The idea is to obtain higher accuracy by extrapolating less accurate solutions based on the theory of truncation errors. Based on the mesh spacing h , it is possible to predict outcomes without actually knowing them, as formulated in equation (5.1). Where, N is value of interest (in this case the force), p is the order of discretisation, N_∞ the extrapolated infinite value of interest and r the refinement ratio.

$$N_\infty = N_p \left(\frac{h}{r} \right) + \frac{N_p \left(\frac{h}{r} \right) - N_p(h)}{r^p - 1} \quad (5.1)$$

Chartier and Greenbaum [9] use the method by taking an initial step size and halve this initial step size the next iteration, leading to improved accuracy and decreased error with every iteration. This study uses the extrapolation method for a mesh study by using the equation (5.1) to obtain a mesh with an infinite number of cells and its corresponding value by increasing the mesh density until it converges towards the final extrapolated value.

It is common to allow a maximum deviation of 1% from the extrapolated *infinite* value[22]. From Figure 5.2 and Table 5.2 it follows that the finest mesh complies with this criterion with the values: $F_{z,\infty} = -8996[N]$ and $F_{y,\infty} = 23602[N]$. The mesh is tested for both the F_z and F_y force at $\eta = 90$ and $\theta = 0$, i.e. the most unsteady inflow angle, to ensure the mesh is fine enough for all cases.

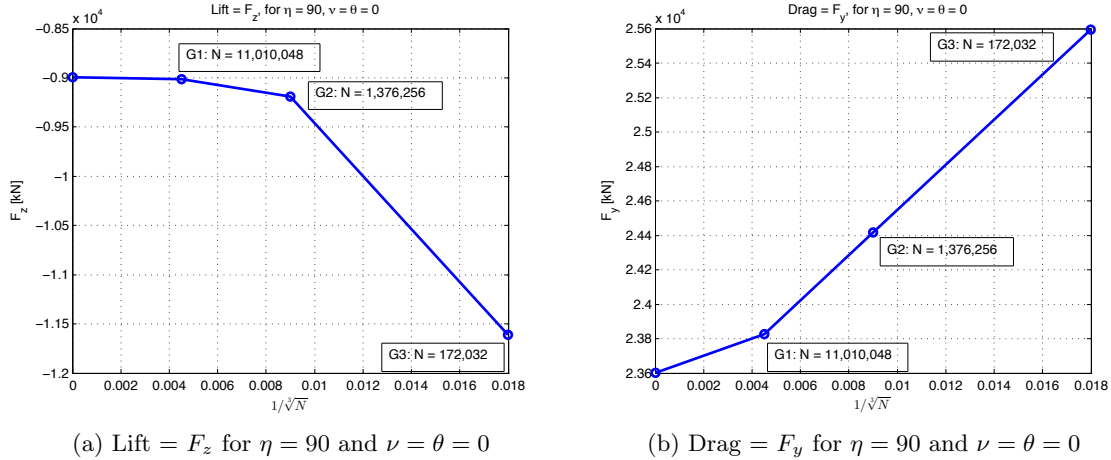


Figure 5.2: Richardson Extrapolation for Suitable Grid Determination

Table 5.2: Percentage Difference between the Grids and Extrapolated $F_{z,\infty}$ and $F_{y,\infty}$

Grid	F_z [N]	% Diff.	F_y [N]	% Diff.
N_∞	-8996	0.0	23602	0.0
G1	-9016	0.22	23825	0.94
G2	-9191	2.17	24415	3.44
G3	-11613	29.1	25594	8.44

5.3 Solver Setup

The CFD model is developed in the commercial package ANSYS Fluent. In this code the user defines the turbulence model, which will be explained in Section 5.3.1. Afterwards the boundary conditions are set, which are the conditions far away from the surface of the blade such as velocity and pressure. These boundary conditions are tested and explained in Section 5.3.2. The accuracy of the model greatly depends on the previously mentioned topics, however the type of discretisation scheme is of equal importance and is tested and discussed in Section 5.3.3. Finally, if all settings and conditions are set correctly, it is crucial that convergence of the solution is assured. The criteria for checking the solution for convergence are discussed in Section 5.3.4.

5.3.1 Turbulence Model

This section is dedicated to set out the differences between the $k - \varepsilon$ and $k - \omega$ turbulence models. $k - \varepsilon$ is widely used for relatively simple flow problems that do not need accurate modelling of the boundary layer and complex viscous effects, therefore its performance for separated flow conditions with adverse pressure gradients is poor [31]. The $k - \omega$ model does allow accurate boundary layer treatment and performs better with adverse pressure gradients in separated flow conditions. The downside of the $k - \omega$ model is the higher computational expense. However, as large angles of attack will be present, accurate modelling of the flow separation is favourable. The combination of the two, $k - \omega$ and

$k - \varepsilon$, namely $k - \omega$ SST (Shear Stress Transport) is used for this fluid investigation. Near the wall $k - \omega$ is used and further away $k - \varepsilon$, with a blending function ensuring proper transition. The inclusion of turbulent shear stress transport enhances the near wall treatment leading to more accurate modelling of flow separation under adverse pressure gradients, which is likely to occur in large pitch angles, $45 < \eta < 135$.

5.3.2 Boundary Conditions

Every computational fluid dynamic problem is defined under the limits of boundary conditions, BC . The inlet boundary conditions is specified where inlet flow velocity is known, hence where the flow comes from. Similarly the outlet BC is where the flow exits the domain. The wall boundary is the blade geometry and is completely rigid. In Fluent one has the option to choose from a multitude of different types of boundary conditions, e.g. velocity, pressure, farfield, etc. For this study the boundary condition, *Pressure Farfield*, would be the most ideal, since only one BC needs to be assigned and the solver defines whether or not the boundary is an inlet or outlet. Moreover, the velocity magnitude and vector can easily be entered by the user, which greatly simplifies the definition of the large amount of different inflow angles modelled. Unfortunately, this BC proved to be very unstable and even in the simplest cases convergence could not be reached due to fast divergence in the pressure solver. For this reason the most stable BC combination is used: *velocity inlet* and *pressure outlet*. Firstly, the velocity inlet boundary conditions specifies the velocity, which is known to be 10 [m/s], and the pressure which is the standard atmospheric pressure, equal to 101325 [Pa]. Secondly, the pressure condition is used where boundary values of pressure are known and the exact details of the flow distribution are unknown. Hence, ideal for the outlet where atmospheric pressure is assumed, since it is far behind the wake and the flow disturbance of the blade have dissipated, but the velocity is unknown. In Figure 5.3 the mesh and its boundary conditions are clearly illustrated.

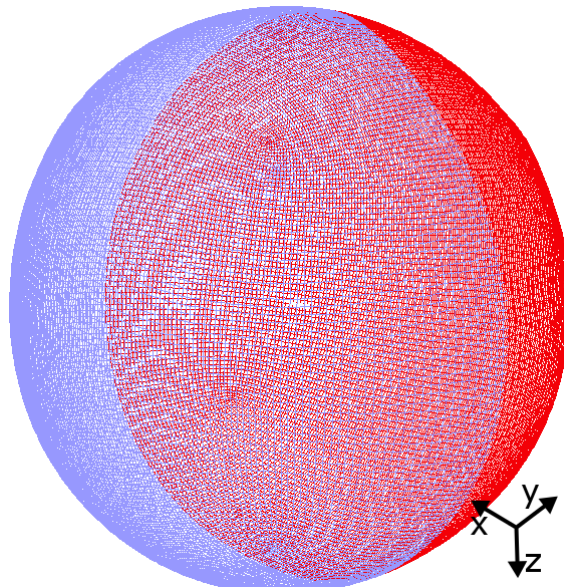


Figure 5.3: Velocity Inlet and Pressure Outlet of the Domain

Unfortunately due to the fact that the grid has been generated in eight subdomains, the in- and outlet are only able to rotate by 90° , while the inflow angle needs to be able to rotate around the spherical domain with steps of 5° . This problem is solved by creating six cases with different flow direction: two as illustrated in Figure 5.3, two with the BC's rotated 90° around the x -axis and two with the BC's rotated 90° around the z -axis. Afterwards, the velocity vector is defined within one of these cases, such that the mesh and geometry remains the same and the inflow angle is changed by rotating the velocity vector around the x - and z -axis, as seen in Figure 5.4, where two examples are illustrated for $\theta = \nu = 0$ and $\nu = \eta = 0$.

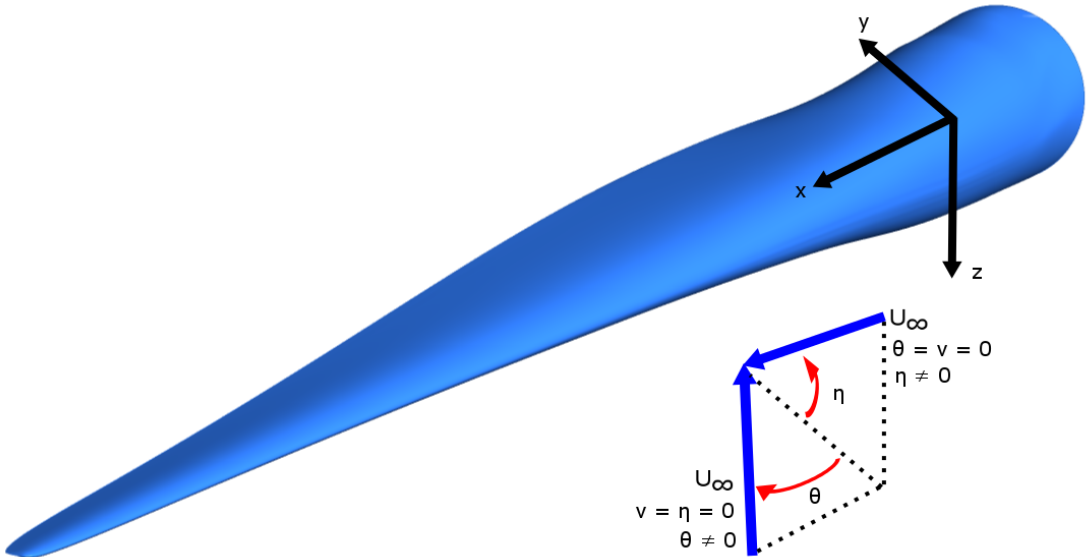


Figure 5.4: Reference Frame and Inflow Definition in CFD Model

This leads to a situation, where the BC are defined in such away that at certain locations in the domain the BC is defined as inflow where it is actually an outflow and visa versa. This leads to unphysical flow distortions, as seen in Figure 5.5. In Figure 5.5(a) the upper right corner shows the region of where outflow is present but inflow is prescribed and the lower left corner shows the region where inflow is present but outflow is prescribed. Note that this distortion is maximum when the offset between the centre line, of the half spherical BC, and the inflow vector is 45° . Table 5.3 summarises all six flow direction cases and the corresponding range of inflow angles.

Table 5.3: Flow Direction Cases and Corresponding Inflow Angles

Flow Direction	Pitch Angle [°]	Yaw Angle [°]
+z	$-45 < \eta < 45$	$-45 < \theta < 45$
-z	$-135 < \eta < 135$	$-135 < \theta < 135$
+y	$-45 < \eta < 45$	$45 < \theta < 135$
-y	$-45 < \eta < 45$	$-135 < \theta < -45$
+x	$45 < \eta < 135$	$-45 < \theta < 45$
-x	$-135 < \eta < -45$	$-45 < \theta < 45$

However, this offset causes unphysical effects at the points where the two BC's meet. In

Figure 5.5 this distortion is visualised in the most extreme case, 45° , and compared with the same inflow case only without an offset. The unphysical flow effects become visible as the dark blue strongly curved streamlines at the bottom left of Figure 5.5(a). In order to ensure that these flow direction cases will generate accurate forces, it is compared with a 'normal' situation where there exists no offset whilst having a 45° yaw angle.

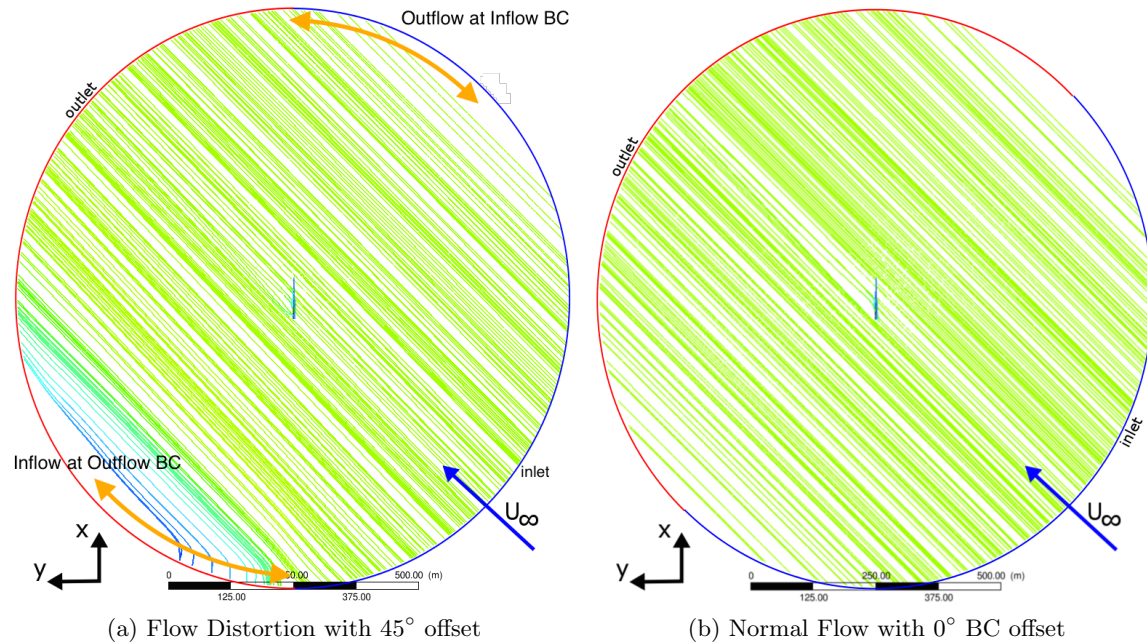


Figure 5.5: Visual Comparison of BC with 45° offset and Reference Case

This comparison proves the flow distortion does not affect the accuracy, as the forces only differ 1.3% from the reference case. This can also be argued by the fact that the blade is still approximately 350 meters removed from the distortion and the flow equals the free stream velocity for the majority of the domain.

5.3.3 Solver Settings

This section describes and states the solver settings used in Ansys Fluent. Several parameters or setups will be investigated and tested in order to ensure that the most accurate CFD model is utilised. Nevertheless, time constraints and computational effort almost always counteract accuracy and the challenge is to find the most appropriate balance between these elements.

As explained in Section 5.3.1, the $k - \omega$ SST model is judged the most appropriate for this study. This model makes use of enhanced wall functions; meaning it automatically checks if the $y+$ value is larger or smaller than 1, see Section 3.3.3. In Fluent, wall functions will be used when $y+ > 1$. The grids are designed such that the elements near the wall are very fine while strongly increasing in size towards the far field conditions. Since wall functions are not applicable for large pitch angles it is advised to assure the maximum $y+$ value is smaller than 1. From Table 5.4 it is seen that the $y+$ is smaller than 1 in all

grids, meaning that the boundary layer is resolved without wall functions. This ensures accurate simulation of the near-wall flow and good prediction of flow separation during adverse pressure gradients in large pitch angles.

Table 5.4: The $y+$ value for the three different grids

Parameter	Mesh G3	Mesh G2	Mesh G1
Number of Elements	172,032	1,376,256	11,010,048
Average $y+$ value	0.154	0.057	0.024

Furthermore also the discretisation scheme and pressure-velocity coupling, both explained in Section 3.3.3, need to be defined. The QUICK discretisation scheme is used mainly due to the third order accuracy. The scheme is best suited for uniform structured grids, such as used in this study. QUICK uses three point upstream weighted quadratic interpolation which highly increases the accuracy, on the contrary it uses more computational effort and is unstable. QUICK has the tendency to be more diffusive and thus requires a good initial guess, obtained by initialising with lower order schemes. This leads to a more stable simulation and ultimately the desired convergence.

The coupled pressure-velocity solver shows superior performance over the segregated solver, due to the ability to solve the equations of all variables for a given cell. This strongly decreases the time to reach the solution, on the other hand it requires significantly more memory. Furthermore, oscillations are more likely to occur, such that the solution will never converge. This can be avoided by starting with the SIMPLE segregated solver and switching to the coupled solver after a certain amount of iterations.

These different discretisation schemes and pressure-velocity coupling methods are tested on the blade for $\eta = \nu = \theta = 0$ in $10 \frac{m}{s}$ wind speed and compared to the Detached Eddy Simulation (DES) done by DTU Wind Energy. The results are presented in Table 5.5.

Table 5.5: Comparison of Turb. Models, Discretisation Schemes and P-V-Coupling for $\theta = \eta = 0$ at $10 [m/s]$ wind

	Drag	% Diff	Lift	% Diff	Iter.	Conv.
DTU Wind Energy DES	2432	0,00%	2091	0,00%	n/a	n/a
$k - \varepsilon$ SIMPLE 2 nd Q.	2163	11,06%	1749	16,36%	3000	Yes
$k - \varepsilon$ Coupled 2 nd Q.	2157	11,31%	1174	43,85%	(4500)	No
SST $k - \omega$ SIMPLE St. 1 st	2954	21,46%	666	68,15%	800	Yes
SST $k - \omega$ Coupled St. Q.	2105	13,45%	1776	15,06%	2200	Yes
SST $k - \omega$ SIMPLE 2 nd Q.	2137	12,13%	1723	16,60%	4300	Yes
SST $k - \omega$ Coupled 2 nd Q.	2488	2,30%	1796	14,11%	2500	Yes

The first term, in Table 5.5, states the turbulence model used, e.g. SST $k - \omega$, the second term indicates the pressure-velocity coupling method, the third term states the discretisation scheme for the pressure (Standard or 2nd) and the last term defines the discretisation scheme for the momentum (1st or QUICK). The result clearly shows the inaccuracy of the 1st order discretisation, which mispredicts the forces on the blade by almost 70%. The higher accuracy of the third order QUICK (Q.) discretisation scheme is also clearly seen. The SST $k - \omega$ turbulence model performs slightly better than the $k - \varepsilon$. Furthermore, the coupled solver decreases the amount of iterations needed as

it solves the equations for all variables for a given cell. On the contrary, this solver is more unstable such that in the case of $k - \varepsilon$ the solution could not converge even after 4500 iterations. Using a 2nd order scheme for the pressure increases the accuracy as seen for the SST $k - \omega$ model with SIMPLE solver. This method needs quite an amount of iterations (4300), which can be lowered by introducing a coupled solver. The coupled solver decreases the amount of iterations needed, however requires a very good initialisation. This last method also predicts a more accurate lift force which is due to the fact that better convergence was obtained. To ensure the coupled solver is correctly converged the solution should be monitored and initialised as explained in Section 5.3.4.

The author also performed a large eddy simulation in the computational fluid dynamic code ANSYS Fluent. Using a kinetic-energy transport subgrid-scale model, a time step of $1e^{-5}$ and a maximum of 20 iterations per time step, the transient simulation computed the forces and moments on the blade. In Table 5.6 the average lift-, drag-, and spanwise force over a time period of 1 second are compared to the HAWC2 results based on the DTU Wind Energy detached eddy simulation. The results are in good agreement such that confidence is obtained in the solver settings of the *CFD model*.

Table 5.6: Comparison of HAWC2 based DES and ANSYS Fluent LES performed by the author for $\theta = 0$ and $\eta = -90$

	Drag	Lift	Span	Iter.	Conv.
DTU Wind Energy DES	23651	-5993	-1198	n/a	n/a
Large Eddy Simulation	23010	-6021	-1210	83400	Yes

5.3.4 Convergency Criteria

Computational fluid dynamics iteratively determines the numerical solution of the fluid problem, however only a sufficiently converged solution provides an accurate result. For a steady-state simulation convergence is ensured when the solution satisfies three conditions: 1) Residual error values have reduced to an acceptable value, typically 10^{-4} or 10^{-5} . 2) Monitor values of interest have reached a steady solution. 3) The domain has imbalances of less than 1%.

The model is initialised with a segregated SIMPLE solver using 1st order discretisation for momentum, pressure, turbulent kinetic energy, k , and specific dissipation, ω . After 500 iterations, 2nd order discretisation is used for momentum and pressure, followed by 200 iterations with QUICK discretisation for momentum. Finally, after 900 iterations, the coupled pressure-velocity solver is used to *jump* to the solution.

In the case there is a steady-state solution but the solution does not seem to converge, it is relevant to use under-relaxation factors (URF). URF are there to suppress oscillations in the flow solution that result from numerical errors, however if they are too small it will significantly slow down convergence. At each iteration, at each cell, a new value for variable in a certain cell P can then be calculated from the following equation, $P^{k+1} = P^k + \text{urf} \cdot P'$, where urf is the under-relaxation factor[6].

In some cases when the flow is relatively more unsteady, e.g. $45 < \eta < 135$, the solution might remain oscillating, due to the fact that there is no pure steady-state solution. In

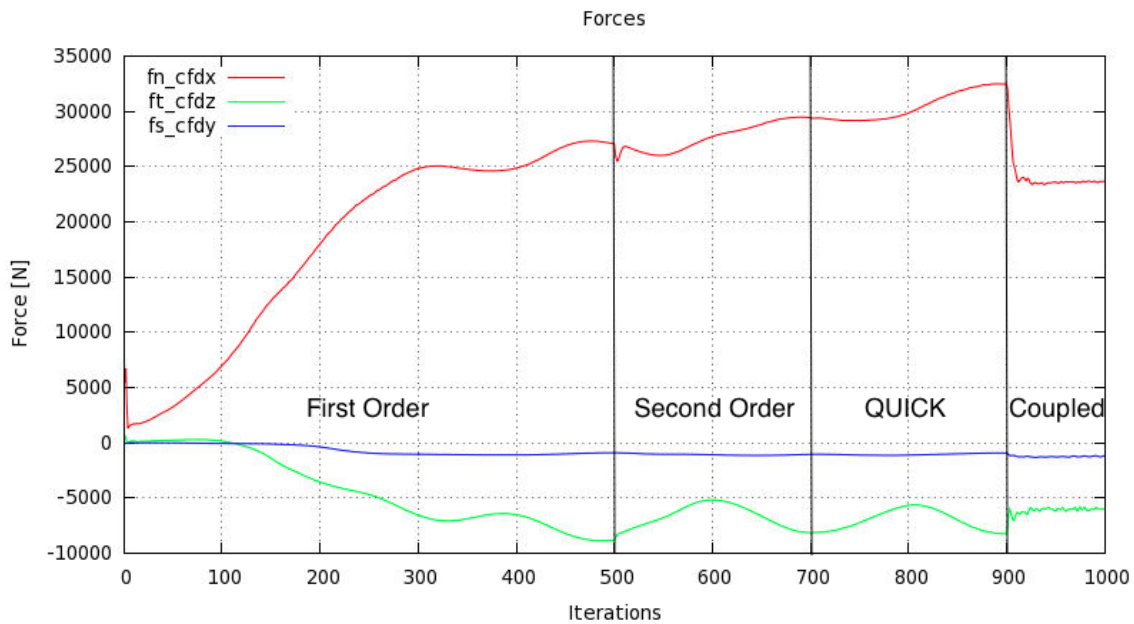


Figure 5.6: CFD Best Practice and Example of Converged Forces

this situation under-relaxation factors do not provide convergence since the oscillation is due to physical effects in the flow, e.g. vortex shedding.

In other cases the flow might contain less unsteadiness such that there exists a pure steady-state solution, e.g. $\eta = 0$. If this is expected a *pseudo transient* solver can be used. In Fluent pseudo transient reverse to pseudo time stepping, which obtains a steady state solution by marching the solution in 'pseudo' time until the steady state condition is reached. The advantage of marching in pseudo time is that it does not require the solution between the initial condition and your final steady-state solution to be a physical representation. The method is based on a time marching scheme. As such, if the problem does not have a steady state solution, the algorithm is not capable of finding the solution and will continuously oscillate or diverge, e.g. vortex shedding in $45 < \eta < 135$. Hence, pseudo transient solving should only be used if the user is confident a steady-state solution exists.

In Figure 5.7 the convergence criteria for the case $\eta = 0$ and $\theta = 40$ are presented. This blade orientation experiences more unsteadiness such that the pseudo transient solving could not be used thus more iterations are required since the problem is solved using the QUICK scheme. Nevertheless it is seen that the solution is converged satisfactorily from both the forces and the moments as well as from the constant mass flow rate.

5.4 Results & Discussion

This part will present the results obtained from the computational fluid dynamic analysis in ANSYS Fluent. Not only the CFD results will be shown, it will also be compared with the equivalent results from the aerodynamic model in HAWC2. First of all, in Section 5.4.1, the static forces and moments on the blade are presented from both the CFD

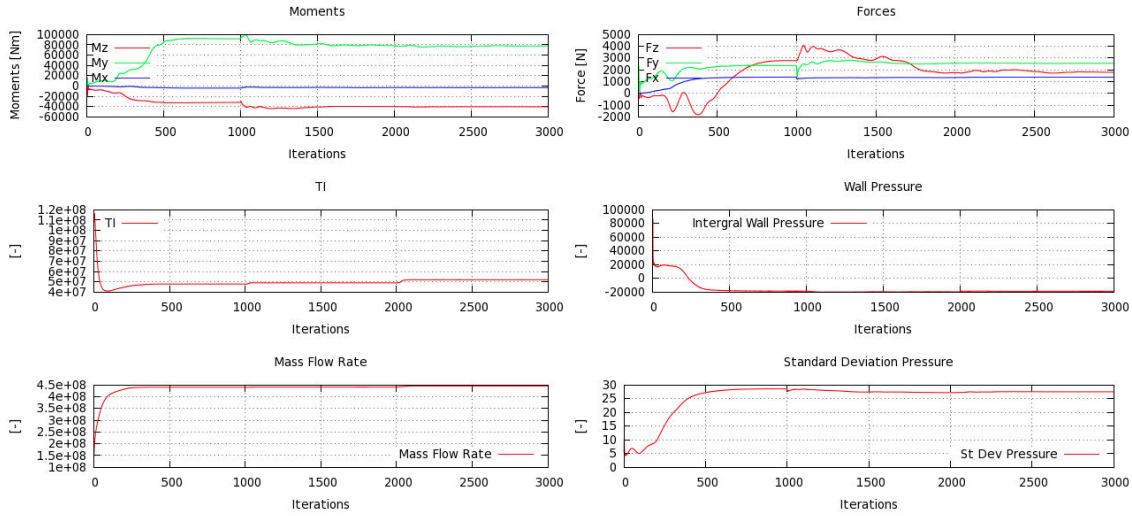


Figure 5.7: Several CFD Convergence Criteria incl. Mass Imbalance

model as from the aerodynamic model. The discussion will provide an explanation of the similarities and differences in the results. Following, in Section 5.4.2, the wake behind the blade is illustrated for the two most important pitch angles to ensure the reader has a clear visualisation of the flow situation. In Section 5.4.3, flow separation between HAWC2 and ANSYS Fluent is compared to argue the difference seen in the forces and moments. Afterwards, in Section 5.4.4, the streamline pattern together with the wall shear stress are displayed in order to discuss the presence of crossflow and the effect on flow separation. Section 5.4.5 presents the estimated standard deviation of the force using the *simplified standard deviation method*. Finally, in Section 5.4.6 the effect of the Gurney flap on the wake structure is visualised.

5.4.1 Forces & Moments

The first results to be discussed are obviously the forces and moments on the blade determined by the high-fidelity CFD model and compared with the simple aerodynamic model. In Figures 5.8, 5.9 and 5.10 the forces and moments are compared for $\eta = 0$ and $\eta = -90$ for a yaw angle from -90° to 90° . Note that the aerodynamic model created in HAWC2 is based on the *crossflow principle* by Hoerner [13], as discussed in Section 3.2.3, and is validated with CFD to determine the feasibility of using it for determining the dynamic behaviour of the blade during installation.

In Figure 5.8(a) the lift force is displayed, where can be seen that for $\eta = -90$ CFD and HAWC2 are reasonably similar, however for $\eta = 0$ the two are very different and do not even show the same trend, resulting from flow phenomena later discussed in Sections 5.4.3 and 5.4.4. Nevertheless for both pitch angles and zero yaw, HAWC2 is within 5% from the equivalent CFD. Figure 5.8(b) plots F_y , which is similar to $Drag \cdot \cos \theta$. The crossflow principle holds reasonable and is similar to the CFD results for both pitch angles, however the force is underpredicted by HAWC2 for $\theta = \pm 30$. This error is explained in Section 3.2.4, and is caused by flow separation which HAWC2 is unable to determine. The third force, F_x in spanwise orientation, is shown in Figure 5.9(a). HAWC2 and CFD do not

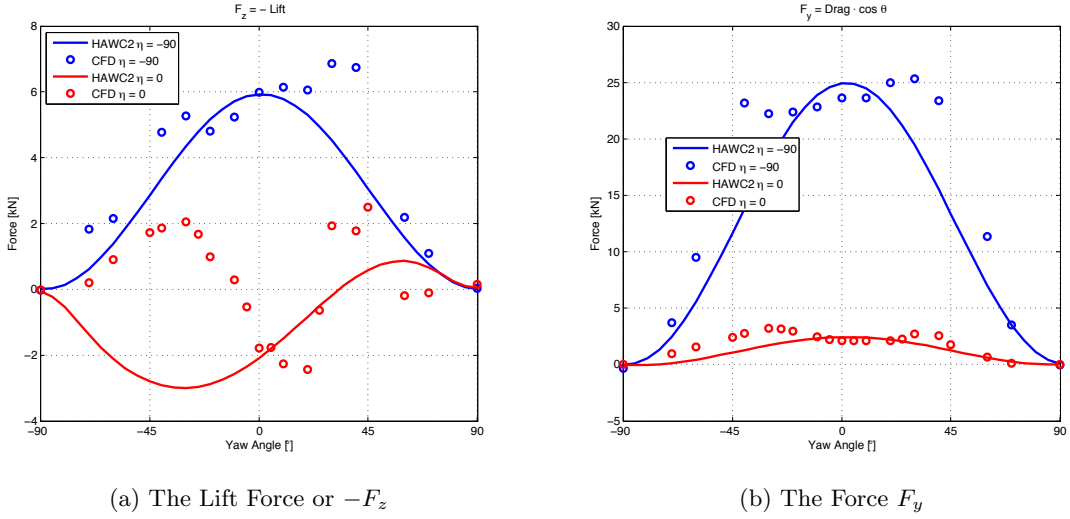


Figure 5.8: CFD to HAWC2 Comparison of F_z and F_y for $-90 < \theta < 90$ and $\eta = -90, 0$

resemble which is explained by the fact that the crossflow principle neglects the spanwise component. However the HAWC2 results are not zero due to the prebend of the blade as argued in Section 4.5.

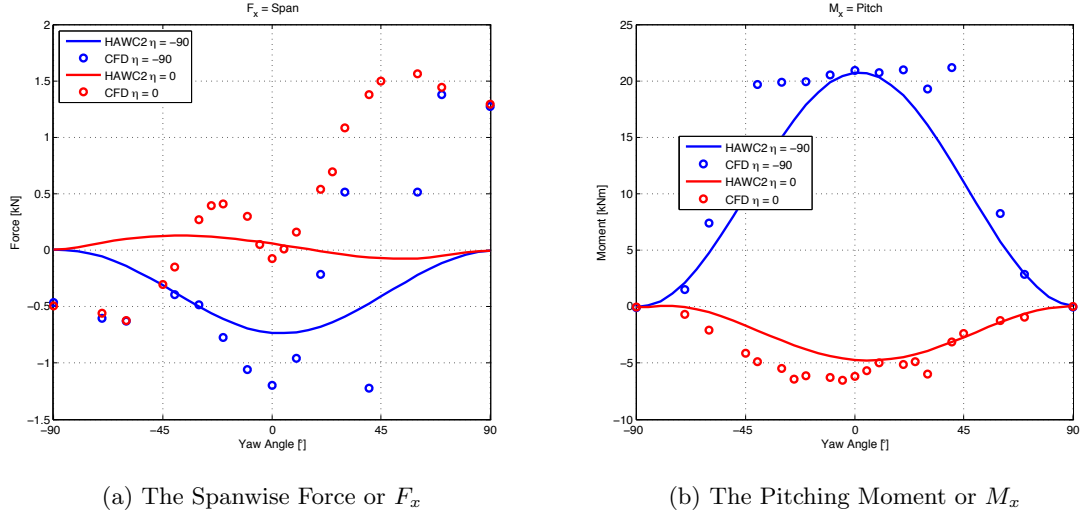


Figure 5.9: CFD to HAWC2 Comparison of F_x and M_x for $-90 < \theta < 90$ and $\eta = -90, 0$

Concerning the moments, Figure 5.9(b), the pitching moment determined by the aerodynamic model behaves very similar to the CFD results. Nevertheless, the same under prediction at $\theta = \pm 30$ is seen as with F_y . Furthermore in Figure 5.10(a) the rolling moment is plotted and clearly the crossflow principle does not perform satisfactory since the CFD results are completely different from the HAWC2 results. This likely a results of the incorrect computation of the lift force in Figure 5.8(a) and will further be investigated in Sections 5.4.3 and 5.4.4. Finally, Figure 5.10(b) displays the yawing moment of the

blade, it can be seen that the moment for $\eta = 0$ from HAWC2 is very accurate, however for $\eta = -90$ there exists a large under estimation at $\theta = -40$ by HAWC2.

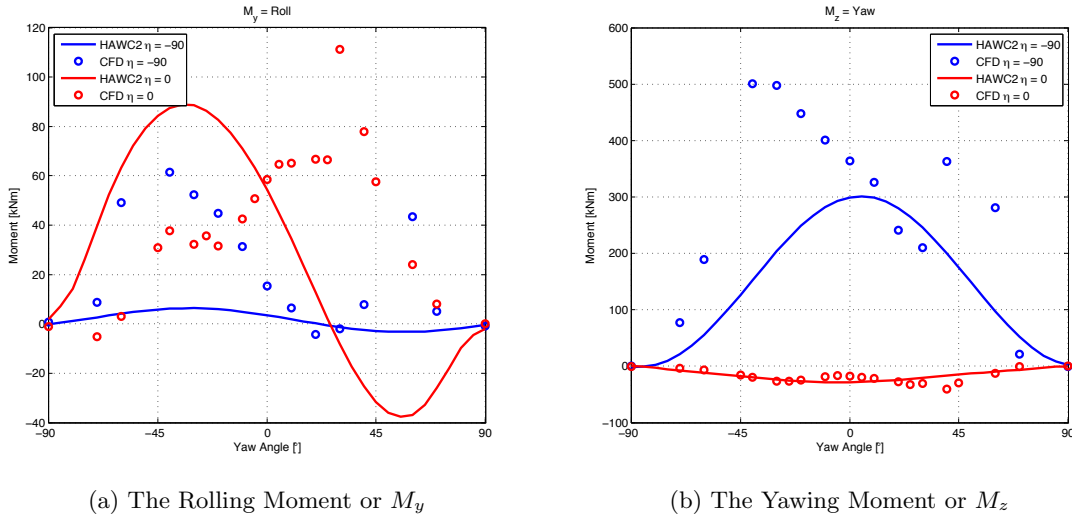


Figure 5.10: CFD to HAWC2 Comparison of M_y and M_z for $-90 < \theta < 90$ and $\eta = -90, 0$

In order to visualise the yawing behaviour of the blade, the centre where the loading acts, R_{drag} , of the F_y force on the spanwise direction of the blade is plotted in Figure 5.11. Here, the change of R_{drag} as function of the yaw angle for two pitch angles 0° and -90° is presented. For $\eta = \theta = 0$ it is seen that the distance from the root to R_{drag} is less than to the Centre of Gravity, CoG, meaning that the blade would rotate with the tip into the wind. When increasing the yaw angle, $\theta > 0$, i.e. the wind vector rotates towards the root, R_{drag} also moves to the root as expected. Analogously, R_{drag} moves more towards the CoG when $\theta < 0$, however the blade still rotates with the tip into the wind. For $\eta = -90$ the location of R_{drag} remains approximately around the mid-section of the blade, represented by the horizontal line 'Mid' in Figure 5.11. However the location is farther from the root than the CoG meaning the blade would rotate with the root into the wind. These results will later be used to compare with the rotations and displacements determined by the *aeroelastic model*.

5.4.2 Wake Visualisation

Illustration of the wake is relevant to ensure the reader has clear visualisation of the wake structure for pitch angles, $\eta = 0$ and $\eta = -90$. This provides proper understanding for further analysis and arguing of specific aerodynamic effects presented in later discussions.

In Figure 5.12(a) and (b) the blade wake is displayed with the velocity contour in five different blade stations for $\eta = -90$ and $\eta = 0$. The large low velocity wake can clearly be seen for $\eta = -90$ compared to the $\eta = 0$ situation. Analogously, in Figure 5.13(a) and (b) the blade is presented for both pitch angles in the horizontal plane. It takes over 300 meters for the wake to be dissipated.

Similarly, in Figure 5.14(a) and (b) the wake is also visualised, now with the streamline pattern over the blade. Noticeable are the converging streamlines in the $\eta = -90$ low

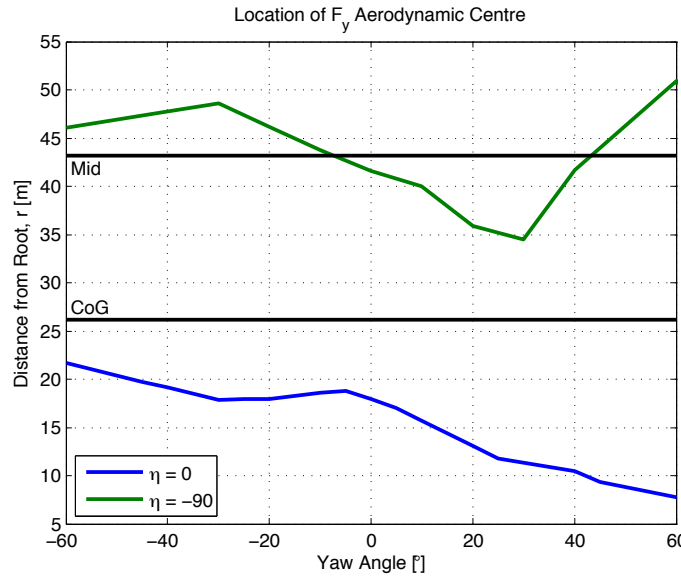


Figure 5.11: Distance from the Root to the point where the Drag acts, R_{drag}

velocity wake, causing the streamlines from the root and tip to bend and spiral inwards into the wake, generating strong vortices. Finally, it is seen that the fluid flow speeds up (dark red) above and below the strong wake of the -90° pitched blade.

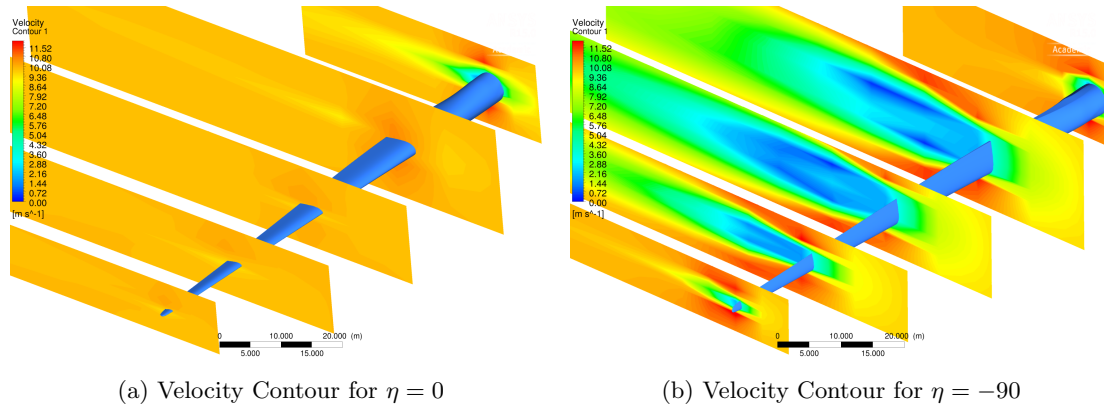


Figure 5.12: Visualisation of the Wake in Airfoil Plane

The cases of $\pm 90^\circ$ yaw, i.e. air flowing from the root to tip or visa versa, are shown in Figure 5.15. Circulation and flow reversal is present for $\theta = +90^\circ$, indicated by the grey negative wall shear stress area. For $\theta = -90^\circ$ a wake is generated at the root where the flow separates.

5.4.3 Streamline Comparison

The forces and moments presented in Section 5.4.1 show differences between the results from the *aerodynamic model* and the *CFD model* in some cases. The difference will be

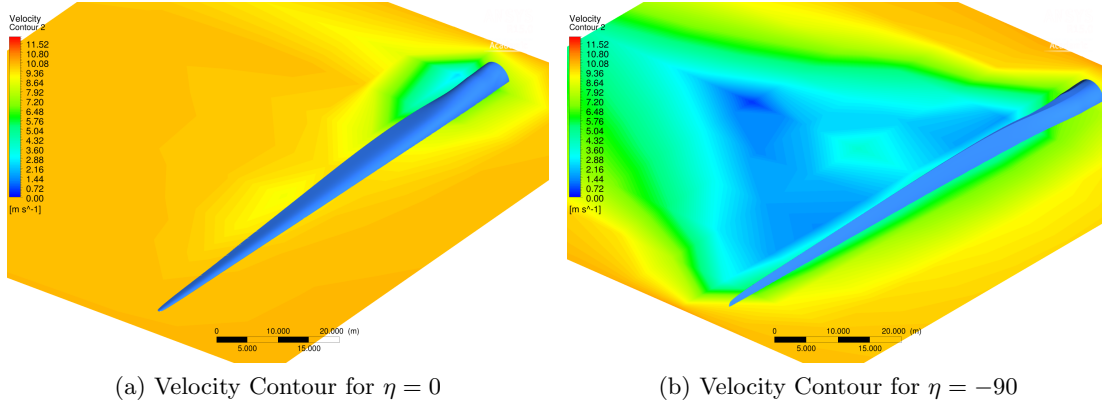


Figure 5.13: Visualisation of the Wake in Spanwise Plane

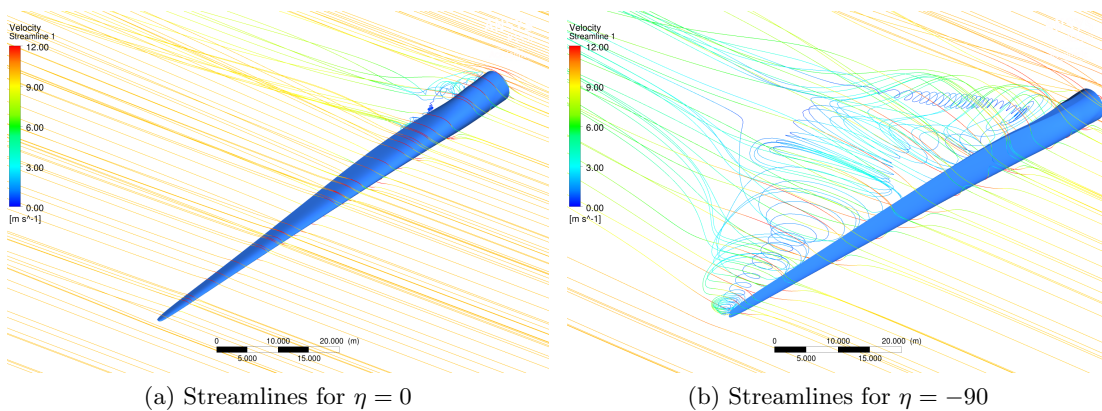


Figure 5.14: Visualisation of the Streamlines

explained on the basis of the prediction of the flow around the blade between HAWC2 and Fluent. This done by looking at the cross-section of four different blade stations. These blade stations are: 2.2, 12.2, 22.2 and 32.2 meters from the root and denoted with the letter R .

Figure 5.16 displays these four most interesting blades stations, all of them close to the root, for $\eta = \theta = 0$. The streamlines are illustrated and coloured with velocity magnitude ranging from 0 to 18 [m/s]. Although HAWC2 is not capable of producing streamlines such as CFD one could say that the 'streamlines' from HAWC2 would look identical to the ones in Figure 5.16.

Recalling the method of the crossflow principle in Section 3.2.3, it is stated that the force coefficients of the yawed blade station is simply scaled with \cos^2 from the un-yawed airfoil section. This means that the principle assumes that the flow around the yawed blade station is identical to flow around the similar un-yawed blade station. However this is not the case. This is partially the source of the difference in the prediction of the lift force between the aerodynamic model and CFD, which will be further visualised in the following illustrations.

Considering the *CFD model*, the first blade stations discussed are at the location R is

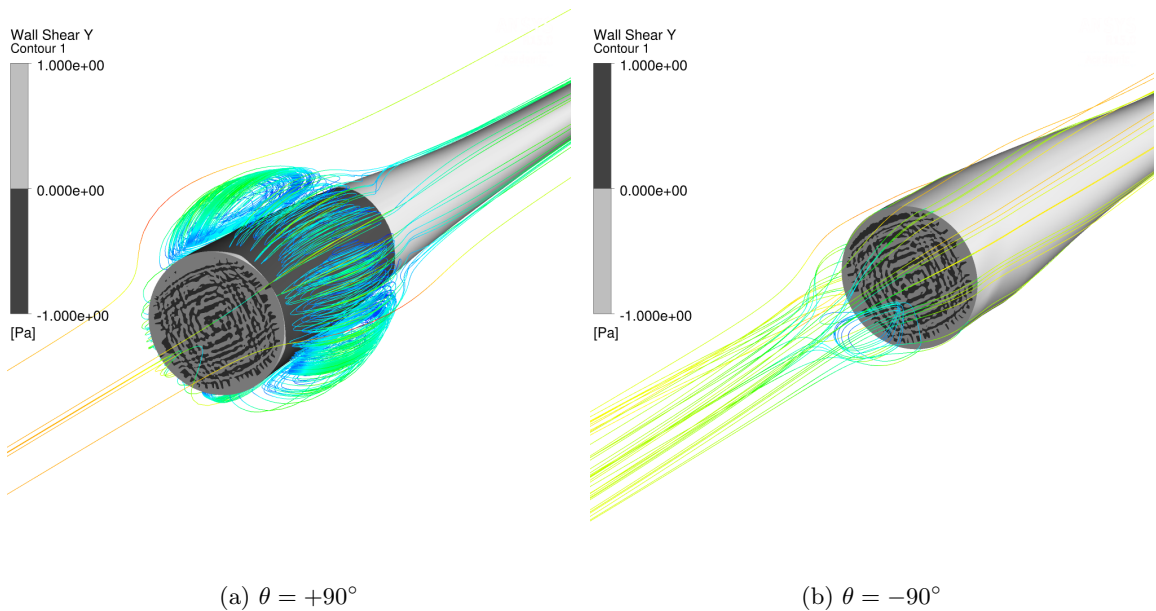


Figure 5.15

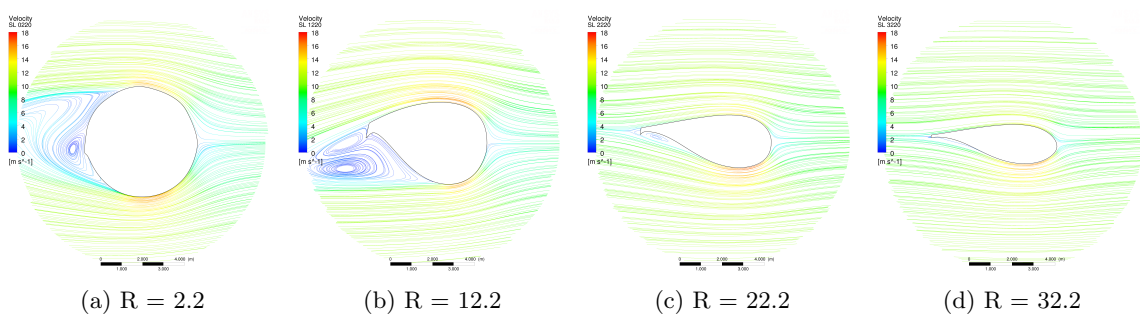


Figure 5.16: Streamline Velocities at Different Blade Stations with $\theta = \eta = 0$

2.2 and 12.2 meters from the root in Figure 5.17, where the streamlines are presented for $\eta = \pm 20$, $\eta = \pm 30$, $\theta = \pm 40$ and $\theta = \pm 60$.

When scaling the force coefficient with \cos^2 the crossflow principle does not take into account whether the yaw angle is positive or negative since the outcome is the same. This leads to the fact that due to the crossflow principle the HAWC2 model considers the positive and negative yaw angle as similar, which seems not to be the case when looking at Figure 5.17.

From the blade stations at 2.2 and 12.2 meters it is immediately noticed that a significantly larger wake is present for the positive yaw cases. Note that positive θ is defined as the wind vector rotated towards the root, as explained in Section 2.4.2. Furthermore, it can be seen that the region of high velocity on the surfaces changes both on the upper as on the lower side, leading to changes in the pressure distribution and thus ultimately the forces.

Analogously, in Figure 5.18 the larger wake is clearly seen for $\theta > 0$. Also for $\theta = -20^\circ$,

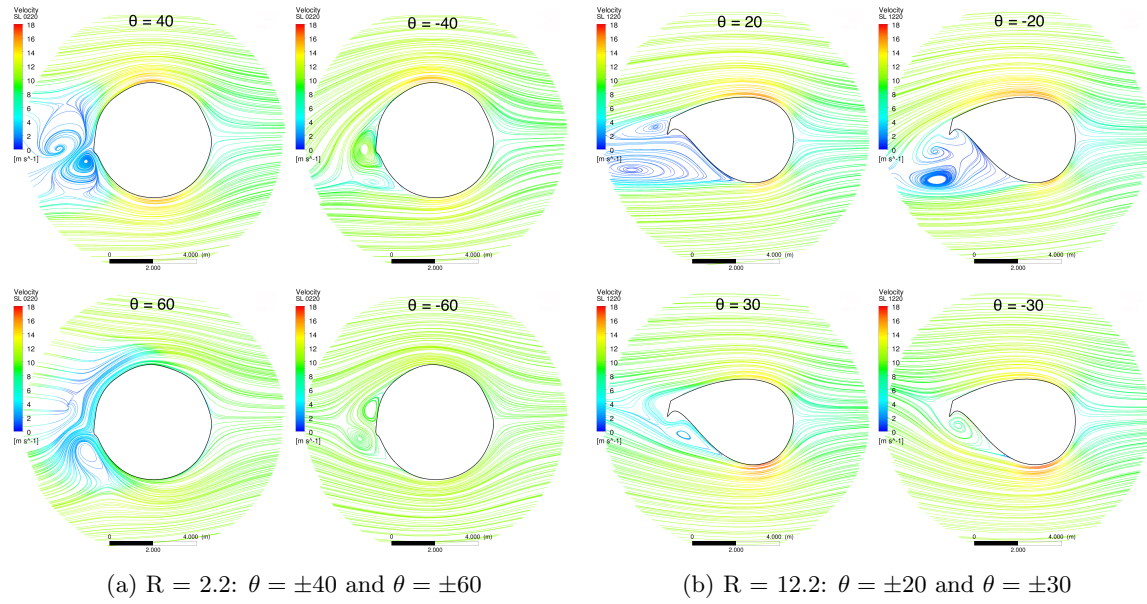


Figure 5.17: Streamline Velocities for $\pm\theta$ at Blade Stations 2.2 and 12.2 [m] with $\eta = 0$

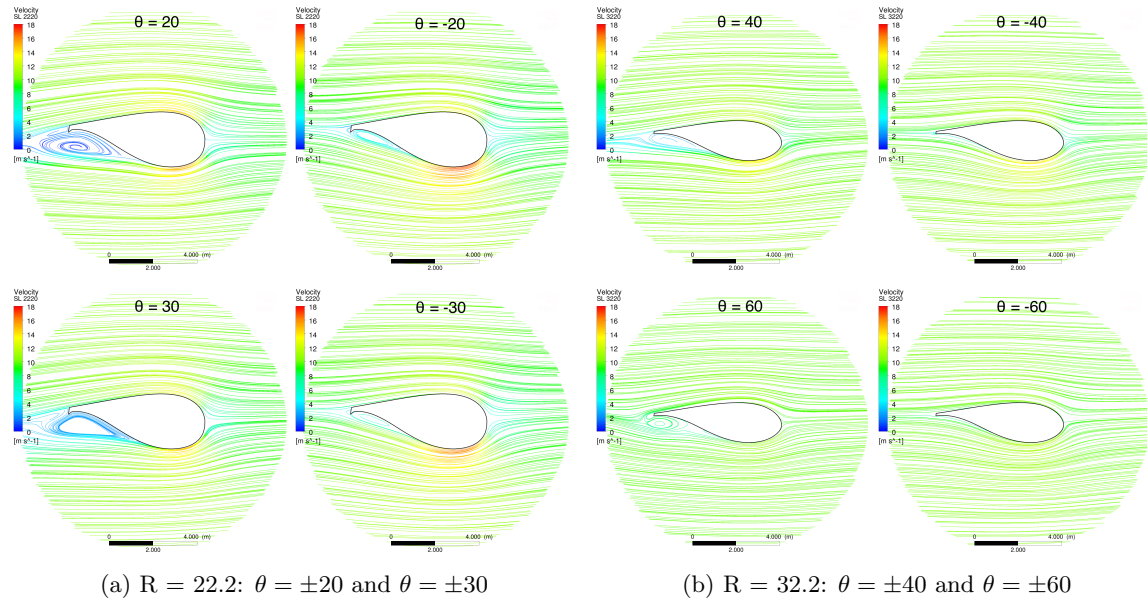


Figure 5.18: Streamline Velocities for $\pm\theta$ at Blade Stations 22.2 and 32.2 [m] with $\eta = 0$

a separation bubble is seen which is not predicted by HAWC2 due to the fact it simply uses $C_d(\theta \neq 0) = C_d(\theta = 0) \cdot \cos^2 \theta$ and thus uses the information of the un-yawed flow situation such as Figure 5.16.

This knowledge justifies the under prediction of the force $-F_y$ by HAWC2 seen in Figure 5.8(b) for $10^\circ < \theta < 60^\circ$. These separation bubbles are created as a result of the three dimensional effects over the blade and the spanwise flow over the blade generating earlier

transition and separation than in an un-yawed case. This will be further explained and visualised in Section 5.4.4.

Finally, from the forces and moments in Section 4.5.1 it is seen that better resemblance are present for the case of $\eta = -90$ between HAWC2 and Fluent. This is in line with the results from the CFD model for pitch -90° where the streamlines patterns are almost identical for $\theta = 0, \theta < 0$ and $\theta > 0$, since the flow is fully separated from trailing edge and leading edge for all yaw cases. The illustrations are not shown here to ensure conciseness of the report.

5.4.4 Crossflow & Flow Separation

In order to argue whether or not the crossflow holds for large yaw angles, crossflow will be identified and the effect on the streamwise component and flow separation illustrated and discussed. In Figure 5.19(a) the blade root is displayed with the streamlines for $\theta = 0$ and $\theta = 20$ accompanied with the wall shear stress on the surface. The first effect to be noticed is the crossflow in the un-yawed situation, caused by the strong three-dimensional effects on the surface due to the twist and airfoil change along the blade. The circular blade root, at the left size of the picture, transforms and twists into a high thickness airfoil towards the tip causing crossflow to develop over the surface. The wall shear stress is negative (dark grey) when flow reversal is present, with this knowledge a distinct line can be drawn where the flow starts to separate from the surface. In the $\theta = 20$ case, at the right side of the image, the flow clearly deflects towards the tip and then back towards the root near the trailing edge, as described in the study by Saric et al. [32]. Finally in Figure 5.19(b) the flow separation region undoubtedly increased in size in the yawed situation, caused by the stronger crossflow as proven by Uranga et al. [45].

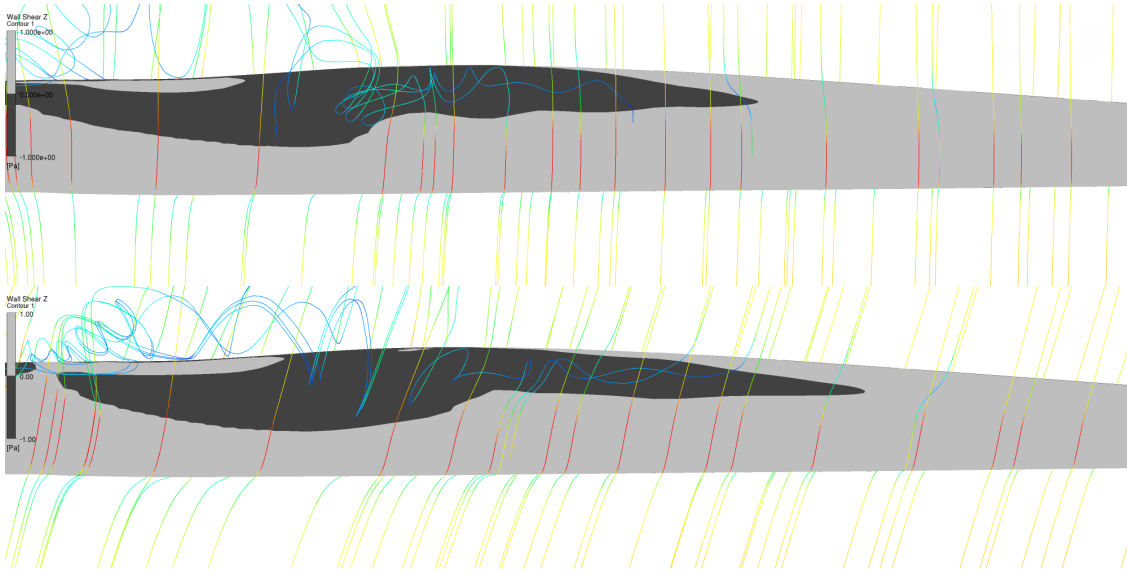


Figure 5.19: Crossflow and Wall Shear Stress Indicating Flow Separation for $\eta = 0$ with $\theta = 0$ (upper) and $\theta = 20$ (lower)

Figure 5.20 analogously present the cases $\theta = 40$ and $\theta = 60$. In the 40° yawed situation more crossflow can be seen and therefore a larger separated flow region. Finally, separation

occurs almost at the same chord-wise location across all yaw angles, however develops more towards the tip when θ increases, which is also recorded in the crossflow study by Uranga et al. [45].

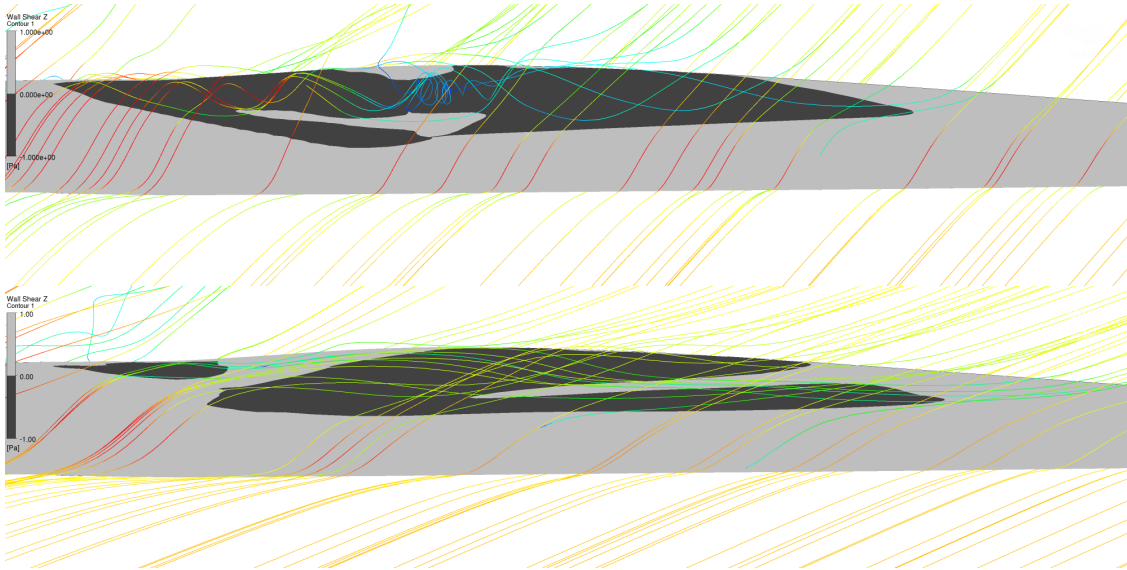


Figure 5.20: Crossflow and Wall Shear Stress Indicating Flow Separation for $\eta = 0$ with $\theta = 40$ (upper) and $\theta = 60$ (lower)

The instantaneous iso-surfaces of the q -criterion of 5.21 show that the yawed blade generates more vortical structures, in particular near the root, than the un-yawed blade; this is consistent with the fact that the flow becomes unstable earlier. Another noticeable phenomena, similar to the research of Uranga et al. [45], is the saturation observed when $\theta > 40$, when the crossflow does not increase and the vortical structures decrease.

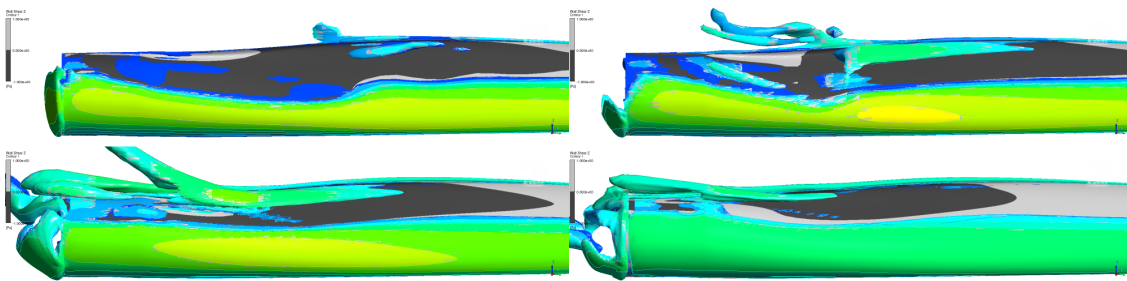


Figure 5.21: Instantaneous Iso-surfaces of the q -criterion for $\theta = 0$ (northwest), $\theta = -20$ (northeast), $\theta = -40$ (southwest) and $\theta = -60$ (southeast)

5.4.5 Standard Deviation

Section 3.2.5 derives a very rudimentary model to determine the fluctuations of the forces on the blade. This *simplified standard deviation method* or std model is based upon the assumption that the fluctuation of the wind are identical in all direction and only experience temporal variation with no change in direction. These assumption are rather

basic, however provide a simple method to be applied to the CFD results and an order of magnitude check when compared with the a more accurate transient simulation from the *aerodynamic model*, as done in Figure 5.22. The drag force for zero yaw and two pitch angles 0° and -90° for a time period of 200 seconds is displayed with a turbulence intensity of 5%. The black line represents a transient simulation from the *aerodynamic model*. The red band represents the mean and standard deviation according to the simplified model of the forces from a steady-state simulation in the *aerodynamic model* and the blue band similar to the red one only for the steady-state solution of the *CFD model*. Note that the red mean line is also the mean of the transient black curve since both are computed with the same model in HAWC2. From Figure 5.22 it can be deducted that the simplified standard deviation model provides a reasonable similar order of magnitude, however in both cases a slightly lower minimum and maximum fluctuation than the transient solution. Nonetheless, due to the fact that conducting transient CFD simulations for all yaw and pitch cases is not an option, inevitably caused by the impossible amount of computational expense needed, this rudimentary std model is the most viable alternative.

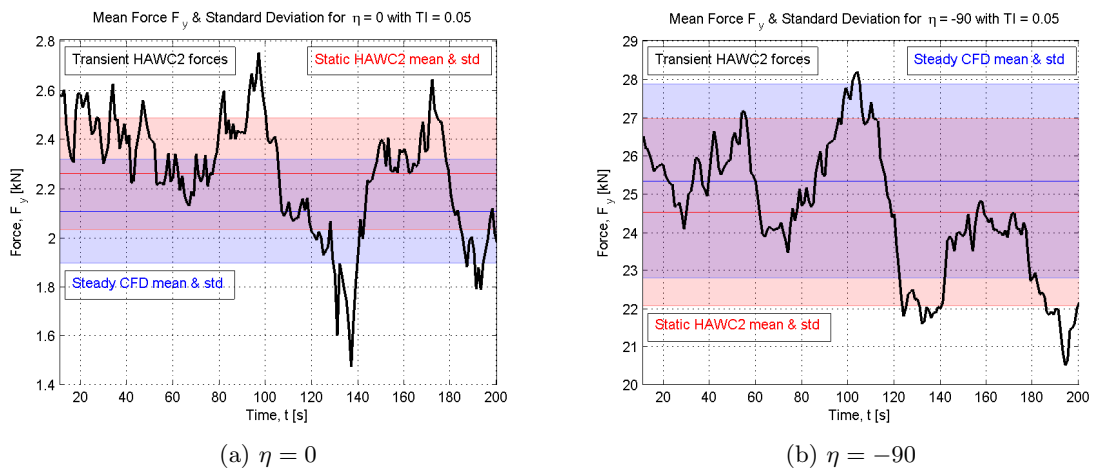


Figure 5.22: Mean Forces & Standard Deviation from Transient Simulation and Simplified Method

As mentioned before the *simplified std model* is a reasonable alternative for indicating the force fluctuations on the blade due to the turbulence intensity. Note that force fluctuations generated by the vortex shedding are not incorporated in this model. Figures 5.23, 5.24 and 5.25 present the similar CFD results as seen in Figure 5.4.1 however the data is now displayed as a continuous line and the standard deviation is added according to the simple model. Two different turbulence intensities are used, 4% and 16 %, of which the latter is measured in offshore location however not very frequent. Turbulence intensity of 4% is common at sea and more appropriate since installation is generally done in easy wind and sea state conditions with low roughness height. The images show that the deviation grows linearly with the increasing force according to expectations based on theory. These images provides the reader with a basic and sufficiently accurate impression of the forces and standard deviation for different yaw, pitch and TI.

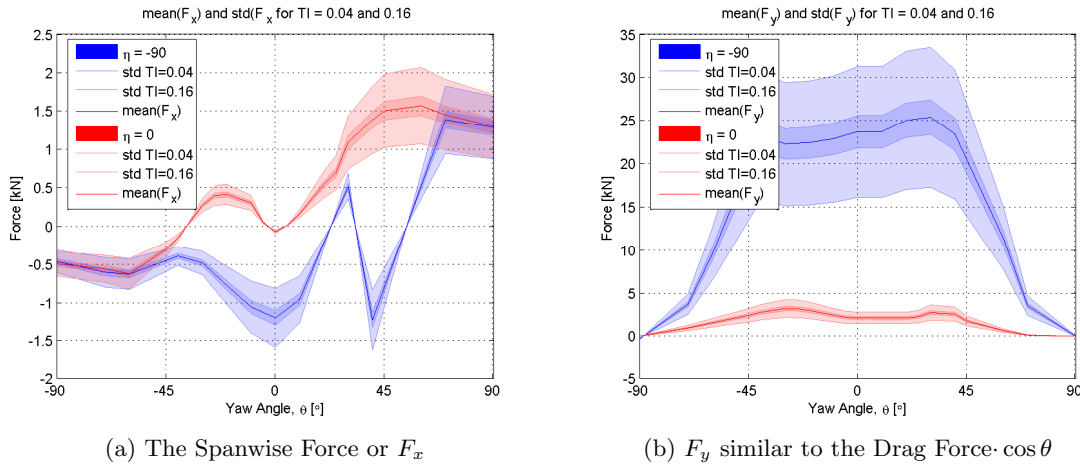


Figure 5.23: Mean and Standard Deviation of F_x and F_y for $-90 < \theta < 90$

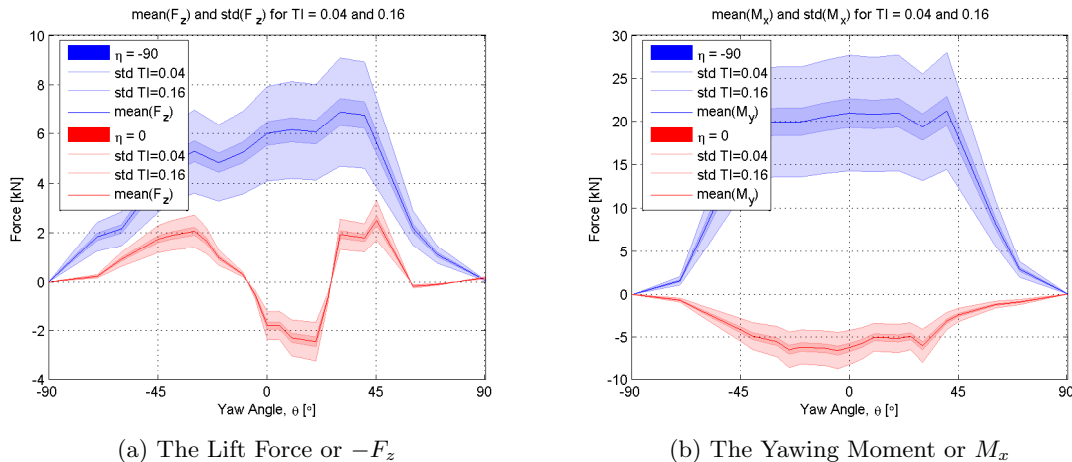


Figure 5.24: Mean and Standard Deviation of F_z and M_x for $-90 < \theta < 90$

5.4.6 Gurney Flap

In Section 4.2 the DTU 10MW reference wind turbine blade is introduced and illustrated including the performance enhancing Gurney flap. However the B75 blade from Siemens WP does not have any Gurney flap and thus the effect of this trailing edge device is investigated here and visualised in Figure 5.26.

The four most interesting blade stations have been chosen, of which all are relatively close to the root. The streamline patterns near the tip do not deviate considerable and are not shown. For all four blade stations the most remarkable phenomenon is that the flow separates earlier from both the upper and the lower side of the airfoil leading to a larger wake behind the blade. The blade station or airfoil section is indicated by R in meters from the root. The difference is largest for blade station 21 in Figure 5.26(d) where the blade without Gurney flap has almost no separation and the one with the device has strong reversed flow. It is also seen that the velocity of the flow is lower on the upper

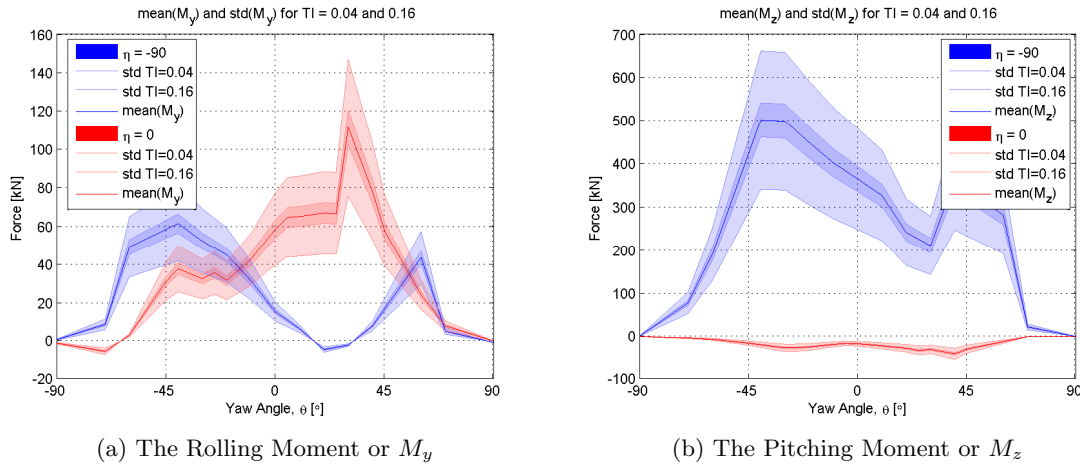


Figure 5.25: Mean and Standard Deviation of M_y and M_z for $-90 < \theta < 90$

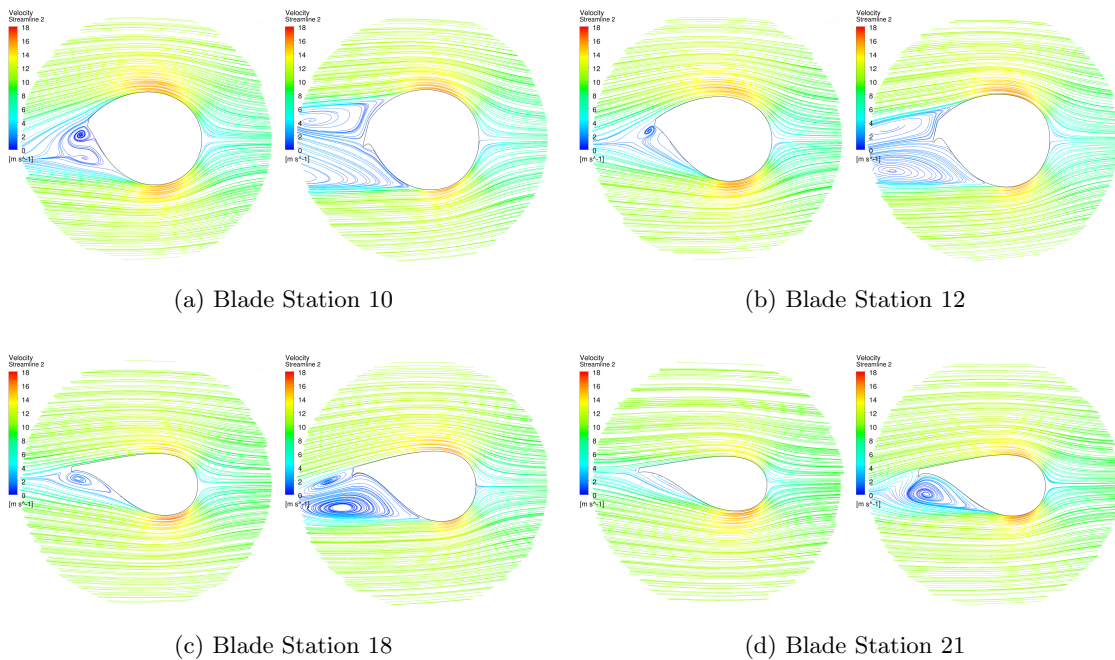


Figure 5.26: Effect of a Gurney Flap on the Wake Structure in $\eta = \theta = 0$

side which would change the pressure distribution and thus the forces in this particular section. The stronger flow reversal and larger wake will lead to higher induced drag and force fluctuations and might affect the behaviour of the blade and with it the complete installation.

5.5 Verification

In the previous Section 5.4.1 the forces and moments of the aerodynamic model are compared to the CFD model, however in order to judge the accuracy of the CFD model, results will be compared to three recent scientific research papers. The CFD computations on a single wind turbine blade by Wang et al. [47] provides a large range of different inflow angles in 8 [m/s] wind. The blade consists of NREL airfoils and has a 38.5 meter length and the first segment near the blade root is a cylinder with 2 meter diameter. The Spalart-Allmaras turbulence model is used for computation and the second order upwind momentum and SIMPLER algorithm is adopted to compute the pressure-velocity coupling. Uranga et al. [45] solves the Navier-Stokes equations using CFD to determine the effect of crossflow on a straight infinite wing using a high-order discontinuous Galerkin method with third order discretisation. The focus is on how crossflow influences transition and separation with varying sweep angles.

In Figure 5.27 and 5.28 the results from the previously introduced articles are presented and compared with the CFD results calculated in this study. All results are normalised with the force in the zero yaw situation, i.e. $\theta = 0$, such that the trend of the different models can be compared. Note that the blade is different in each study considering length, airfoils, twist, thickness, etc. Nonetheless, qualitative comparison is very useful in order to argue the accuracy of the created CFD model.

Figure 5.27(a) shows the normalised force F_y which is the force in chordwise direction of the blade, note $F_y = D \cdot \cos \theta$. Although the results from Wang et al. [47] are not identical to the CFD results, it does follow the same trend; both show the noticeable peak at $\theta = 30$. Likewise, the drag force D in streamwise direction in Figure 5.27(b) presents a similar trend of increasing drag with larger yaw angles, induced by the stronger crossflow causing earlier transition and separation according to Uranga et al. [45] and seen in Section 5.4.4.

In Figure 5.28(a) and (b) the lift force $-F_z$ and span force F_x are illustrated respectively. The lift force decreases for all models however it becomes negative according to Wang et al. [47] and the CFD model, which might have to do with the fact that both investigations use a largely twisted and high thickness blade while Uranga et al. [45] uses a straight wing. Finally, the spanwise force corresponds for all studies and is roughly linearly with increasing yaw angle as demonstrated by Uranga et al. [45].

The research paper by Sørensen and Michelsen [39] demonstrates that state of the art 3D CFD codes are capable of predicting the correct integrated drag of a flat plate placed perpendicular to the flow. In the paper the Reynolds Averaged Navier-Stokes (RANS) equations are solved using the DTU EllipSys3D CFD code with a $k - \omega$ SST turbulence model, a PISO algorithm for the pressure-velocity coupling and third order QUICK discretisation using under-relaxation factors; all very similar to the CFD setup used in this study. The CFD model by Sørensen and Michelsen [39] is validated by comparing the computed C_D on three different flat plates with experimental data from Hoerner [13], seen in Table 5.7. Subsequently the same model is used to determine the C_D of four wind turbine blades, where a C_D between 1.16 and 1.32 was found, which is in good agreement with existing full scale measurements on other wind turbine blade geometries. As can be seen the C_D value computed by the developed *CFD model* of the DTU 10MW reference wind turbine blade used in this study is in good agreement with the results from

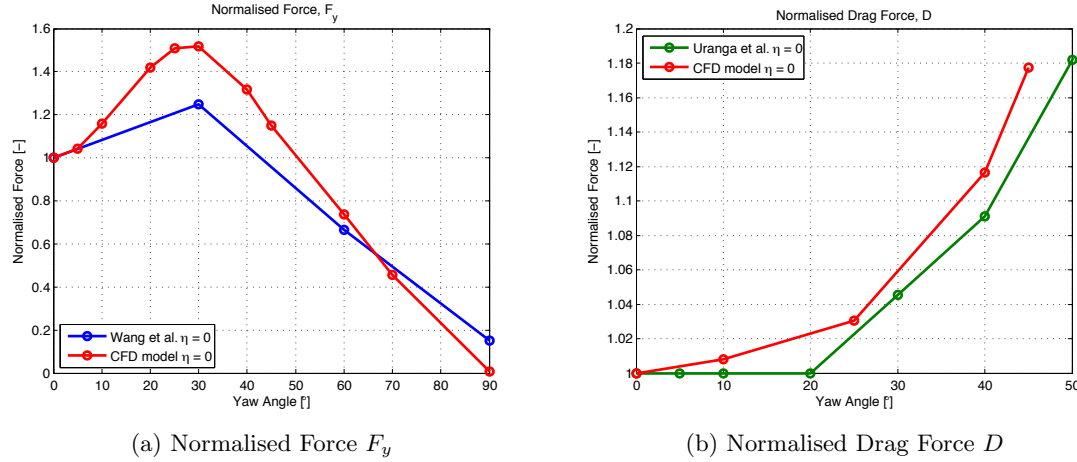


Figure 5.27: Normalised Drag Force Comparison with Wang et al. [47] and Uranga et al. [45]

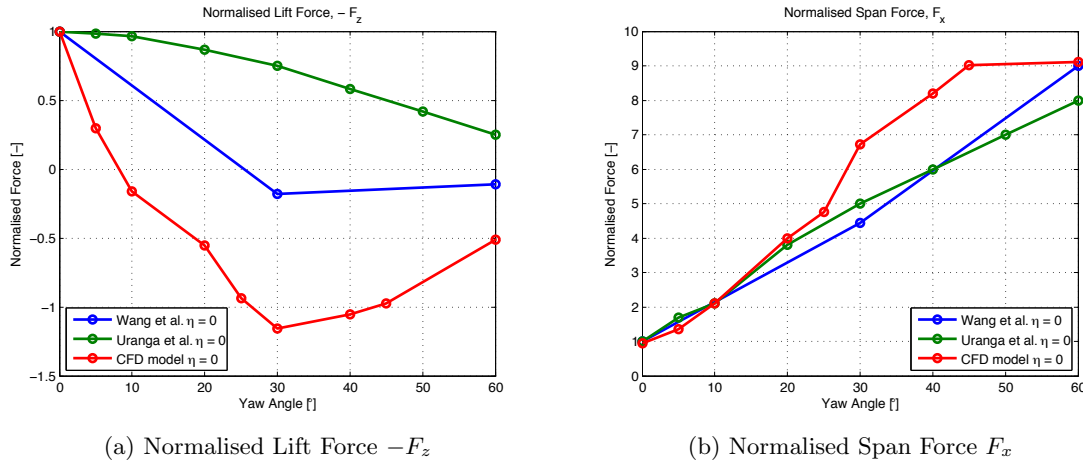


Figure 5.28: Normalised Lift and Span Comparison with Wang et al. [47] and Uranga et al. [45]

Sørensen and Michelsen [39] and the measurement data. The slightly lower value could be appointed to the fact that the DTU 10MW reference blade is designed to be a very slender blade.

The high similarity in the trend line of the normalised forces with Wang et al. [47] and Uranga et al. [45] together with the very good agreement of the drag coefficient with the measurement data of Hoerner [13] and computations by Sørensen and Michelsen [39] provide excellent confidence in the accuracy of the developed CFD model in this study.

5.6 Summary

This chapter explained the workings of the *CFD model* and discussed the results and comparison with the *aerodynamic model* to prove the validity of the crossflow principle.

Table 5.7: C_D of the DTU 10MW blade and several flat plates and other wind turbine blades

	L/w	C_D comp.	C_D meas.
Plate 1	2	1.20	1.18
Plate 2	20	1.48	1.49
Plate 3	40	1.73	1.73
LM8.2	11.4	1.23	
LM19.1	18.0	1.32	
Modern 1	21.0	1.16	
Modern 2	24.0	1.27	
DTU 10MW	29.0	1.14	

The findings provide knowledge to answer the first research question, **1. how to model the aerodynamic forces and dynamic behaviour of a hoisted wind turbine blade in different inflow angles?**.

The three dimensional *CFD model* simulates the flow and computes the mean loading with a Reynolds-Average Navier-Stokes solver with third order accurate QUICK discretisation using a $k - \omega$ SST turbulence model in ANSYS Fluent. Forces are determined for a range of yaw angles and two pitch angles and show reasonable agreement between the *aerodynamic model* and the *CFD model* for certain forces and moments.

In -90° pitch for the drag- and lift force as well as the pitching- and yawing moment, the models show similarity. In 0° pitch there is correspondence for the drag force and the the pitching- and yawing moment. The spanwise force does not match, however this is expected since this load is neglected by the crossflow principle. The lift force and rolling moment for 0° pitch show completely different trends by the two models.

In a streamline study from the CFD results it is demonstrated that the yawed cases have completely different flow behaviour from the un-yawed case. Additionally, the positive and negative yaw cases, e.g. 30° and -30° , have a very much different wake structure from each other. This leads to believe that the *aerodynamic model* is unable to simulate the three-dimensional effects acting on the blade. From the CFD results it is displayed that the wake for positive yaw, hence velocity vector rotated towards the root, increases and flow reversal appears.

Further investigating of the streamlines leads to the observation that already in zero yaw the flow is highly three-dimensional which increases with positive yawing of the inflow. Furthermore, the negative wall shear stress region also increases with positive yaw, indicating a larger flow separation region with flow reversal. These phenomena is also seen by the research from Uranga et al. [45], who demonstrates that this is caused by the increasing spanwise flow, which destabilises the chordwise flow leading to earlier flow separation. This phenomena increases towards a certain yaw angle between 40° and 60° after which a saturation point is reached and the flow separation and unsteadiness in the flow decreases, which is also established by Uranga et al. [45].

Afterwards, the influence of the Gurney flap is tested by comparing the streamline patterns of four blade stations near the root where the trailing edge device is present. This showed that the Gurney flap significantly increases the size of the wake structure behind the blade for 0° pitch.

In the last section, the normalised forces from the *CFD model* are compared with studies from Uranga et al. [45] and Wang et al. [47], proving good agreement which verifies the developed model. Finally, the CFD model is compared with measured and computed drag coefficients from the paper by Sørensen and Michelsen [39], which provides excellent agreement and verification.

Chapter 6

Aeroelastic Model

The previous *aerodynamic model* and *CFD model* where necessary to partially answer the first research question, **1. how to model the aerodynamic forces and dynamic behaviour of a hoisted wind turbine blade in different inflow angles?**. The aerodynamic forces in different inflow angles can accurately be determined with the CFD model and with lesser accuracy but arguable validity with the aerodynamic model. The *aeroelastic model* will be able to model the forces and moments over time and their coupling with the dynamic blade-cable system. This chapter will discuss the developed *aeroelastic model* and perform task *three* "determine the motion of the blade due to these forces".

The transient model setup in HAWC2 will be discussed in Section 6.1, followed by key results to determine the validity of the model in Section 6.2. In Section 6.3 the results will be verified with research papers and discussion of its validity is done in Section 6.4. Finally a summary is presented in Section 6.5.

6.1 Model Setup

The aeroelastic model is based on the same principle as the aerodynamic model and thus holds the same structure. However, the cable system is added in order to simulate the coupling between the dynamics and aerodynamics, hence aeroelasticity. The cables are modelled as a series of small Timoshenko beam elements, refer to Section 3.1.3, and connected with a fixed joint or a spherical joint. The spherical joint constraints any form of translation and permits all rotational behaviour. This system is illustrated in Figure 6.1. The purple and yellow dots represent a spherical and fixed joint respectively, the red dot indicates fixation with the ground (i.e. global reference frame).

The at DTU Wind Energy developed tool, **Animation.exe**, is able to illustrate and animate the motion of the system. For a good understanding an image is presented with the simplified blade shown in the x - z plane in Figure 6.2. The wind direction is along the y -axis and its vector points out of the paper. In the following Section 6.2 the results will be discussed and blade positions will be presented in the global reference frame shown in

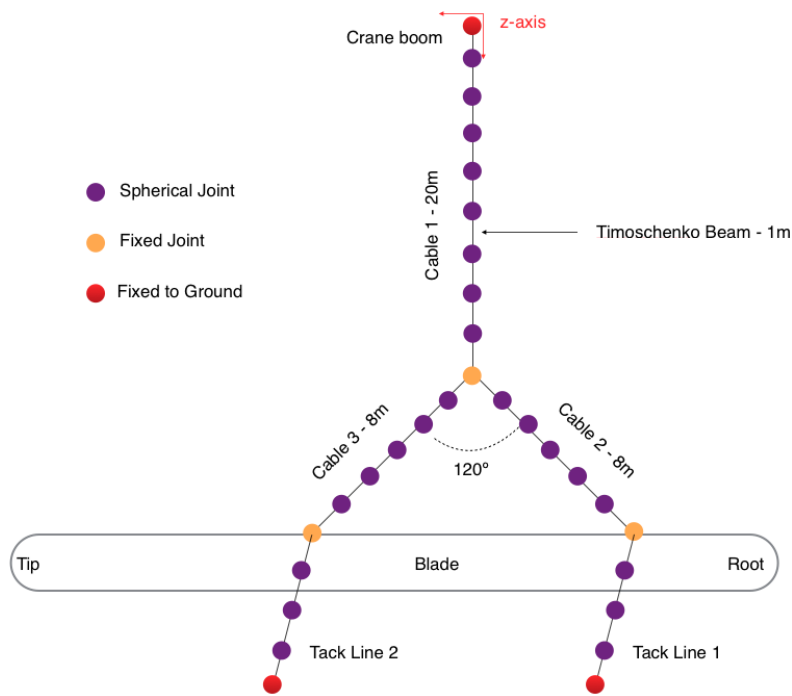


Figure 6.1: Representation of the HSBM system in HAWC2

Figure 6.2. In order to ensure consistency and clarity for the reader the axis are once more defined: the z -axis is positive downwards, the y -axis is positive along the wind direction and the x -axis is positive along the blade length according to the righthand rule. The model can also be seen in Figure 3.1.

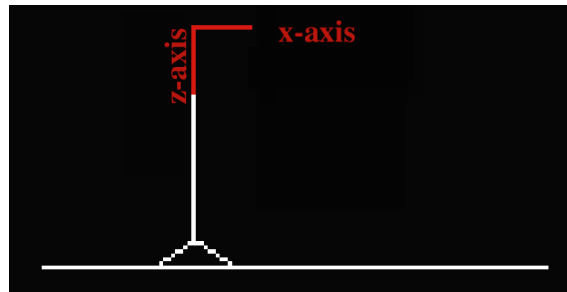


Figure 6.2: "Animation.exe" Image

Calculations are done for different yaw, pitch, wind and turbulence conditions and positions are determined at the blade tip and root in x -, y - and z -direction. However, to keep this thesis concise only relevant data is shown instead of all possible combinations. The data is visualised in graphs where the horizontal axis holds the time in seconds and the vertical axis holds the position with respect to the global reference frame in meters. The global reference frame is defined at the top of the upper cable where it is fixed to the crane boom, as seen in Figure 3.1. The system is simulated for 2240 seconds since the initial blade movement is completely damped out after 2000 seconds.

Finally the simulations are run in the same wind conditions as the *aerodynamic model*,

in Section 4.3, and uses the same aerodynamic calculation method as specified in Section 3.2.2.

6.1.1 Dynamic Stall

HAWC2 makes use of a Beddoes-Leishmann dynamic stall model in order to compute the forces on the blade due to heaving and pitching of the airfoil section over time. In the cases that the blade is hoisted in either 0° or $\pm 90^\circ$ pitch, the dynamic stall effect is not present since the airfoil sections are not in the region of stall, as can be seen in the C_l and C_d force coefficients in Figure 4.4. However, in the cases of approximately 20° pitch there is a small difference seen in the forces on the blade between excluding and including the Beddoes-Leishmann dynamic stall model. These discrepancies are significantly low, leading to the conclusion that dynamic stall does not strongly affect the blade behaviour. Further investigation yields that the heaving and pitching has a low frequency to such an extend that dynamic stall does not arise.

6.1.2 Cable Properties

The cables are modelled as series of Timoshenko beam elements interconnected by spherical joints as illustrated in Figure 6.1. The cables have a high modulus of elasticity and shear modulus of elasticity, low area moments of inertia and a cross-sectional aero of 0.1 [m^2]. In the structural file the Rayleigh damping parameters are added to the cable elements. The damping factors M_x , M_y and M_z are set to zero, the stiffness factors K_x , K_y and K_z are set to $1.53e^{-2}$, $2.55e^{-2}$ and $3.30e^{-3}$, respectively, according to Kim et al. [16]. Due to the fact that the cable elements are massless they might also be modelled as single beams rather than multiple beams, since sagging of the wire is not modelled when there exists no weight. This is tested by modelling the vertical hoisting cable, the two diagonal hoisting cables and the tackline cables as a single element, such that the whole system consists of five beam elements. This lead to the observation that this modification greatly influences the system, since the single beam elements can now withstand compression, which is truly unphysical. Further investigation leads to the understanding that the three hoisting cables remain in tension and only the two tacklines experience compression. Finally, when simulating the hoisting cables as single beams and the tacklines as multiple beams it is seen that the root displacement and behaviour of the blade is similar to the case where all cables are modelled as multiple beams. This observation indicates that the triangle enclosed by the two diagonal hoisting cables and the blade acts as a solid body. This conclusion is later used to investigate the influence of the shape of this solid triangle. Note that this is only the case for massless beam elements. Incorporating cable mass introduces sagging of the wire and to simulate this effect all cables should be modelled as multiple beam elements. From a simulation in the *aeroelastic model* it has been concluded that adding weight to the tacklines increases the damping on the dynamic system.

6.1.3 Blade Deformation

In the *aeroelastic model* the blade is modelled flexible. In order to see what the influence of the blade elasticity is, simulations are done for a long time period of 5000 seconds to

compare the tip displacement with the tip deformation. The deformation in x -direction is zero since the blade does not deform in spanwise direction. For $\eta = -90$ and a windspeed of 30 [m/s] the maximum tip deformation is 0.372 meters in y -direction (i.e. flapwise). This deformation is relatively small compared to the large displacement of the tip (up to 3 meters) due to the rotation of the blade. However it should be noted that the deformation of the blade is strongly dependent on the stiffness properties of the blade. In the following simulations the blade deformations are taken into account according to the blade stiffest properties set by Kim et al. [16]. The observation that the blade deformation is relatively small compared to the displacement agrees with the conclusions from the research of Gaunaa et al. [12] where the stiff blade model returns a valid approximation of the structural response. However this is only the case when the rigid motions that the blade experiences during mounting have prevailing frequencies which are lower than 0.4 Hz.

6.2 Results & Discussion

How the *aeroelastic model* in the HAWC2 code is set up has been explained in Section 6.1. This part will present the initially obtained results and will discuss and interpret the findings. The model's capability will be demonstrated by means of computing the forces on the blade, cable tension in the tacklines and the displacement of the root, δ . The simulation is done over an interval of 4 minutes and the wind velocity is ramped up in the first 2 minutes in order to resemble the reality, as seen in Figure 6.3. The data from the simulation is recorded from 2000 seconds since the blade-yoke-cable system needs to damp out to ensure displacement and fluctuation are due to the variables tested. Figure 6.3 shows the windspeed ramp up for different velocities and turbulence intensities.

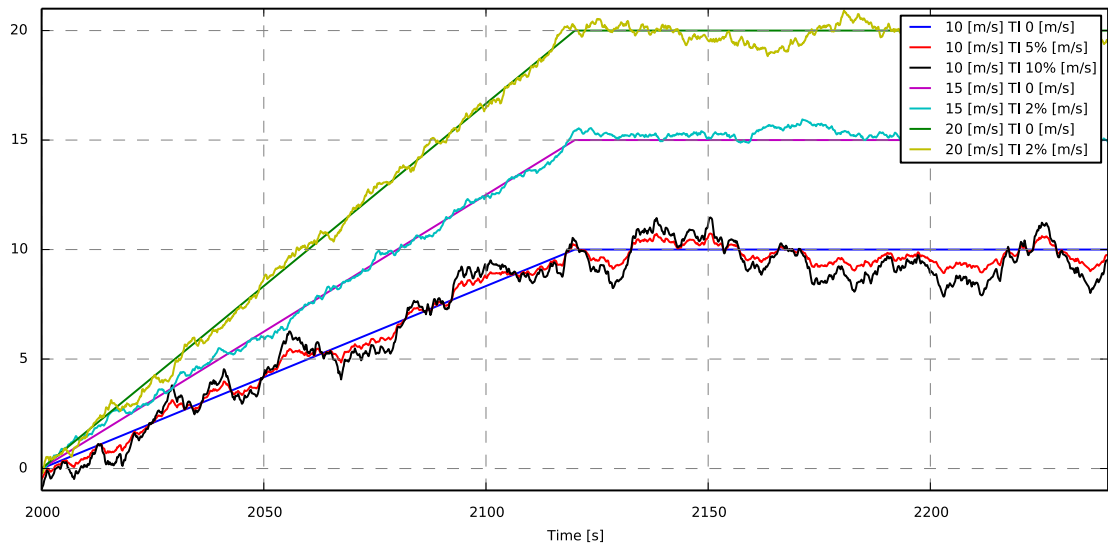


Figure 6.3: Different Wind Velocities & Turbulence Intensities

6.2.1 Forces & Cable Tension

In the aeroelastic model the time depending behaviour of the blade can be simulated. The windspeed is ramped up according to Figure 6.3 and from it the forces and cable tensions will be determined and displayed. In Figure 6.4(a) the aerodynamic force F_z , hence similar to minus the lift, is presented for six different windspeed without any turbulence intensity and with a yoke mass of 57,000 kg. For 10 [m/s] it is assessed that the loads F_y and F_z are similar to the loads determined from the *aerodynamic model*, which is expected. The aerodynamic force increases with increasing windspeed in a quadratic fashion as already seen from the analytical expression and the previous developed models.

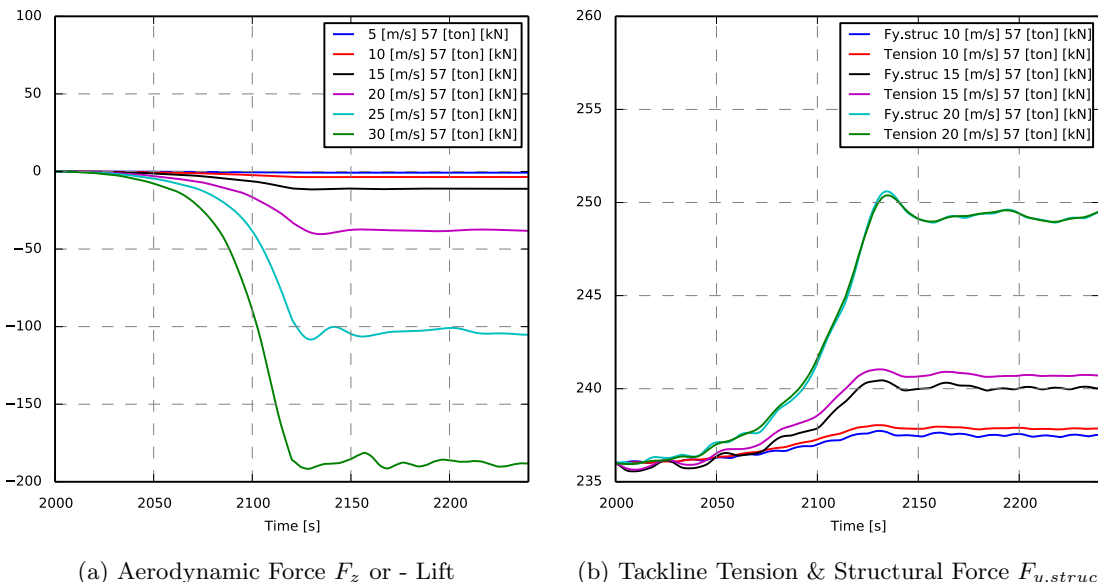


Figure 6.4: F_z & Cable Tension for Different Windspeed at $\eta = \theta = 0$ with 57 ton Yoke

Figure 6.4(b) plots the tackline tension together with the structural force in y -direction, note this structural $F_{y,struc}$ is not similar to F_y which is solely the aerodynamic force similar to the drag when $\theta = 0$. The graph shows that the tension in the tackline behaves in a similar trend as the forces in the horizontal plane, i.e. $F_{y,struc}$, which is as expected since the tackline tension is directly influenced by the drag on the blade.

6.2.2 Root Displacement

The alignment of the root to the hub is the a very delicate procedure. Therefore this study will solely present the displacement of the blade root instead of the tip. However, the tip movement has been checked throughout this investigation and it is assessed that the behaviour is similar to the root movement only in opposite direction. This means that the blade mostly rotates around the z -axis (i.e. yawing) at the centre of gravity. Note that due to the fact that the tip is further removed from the CoG, the tip displacement is larger than the root. However the tip displacement is not considered to be the most relevant for the blade installation.

In Figure 6.5 the blade root positions in x -, y - and z -direction over time, omitting turbulence intensity, for four different wind velocities are presented. The root displacement is defined as the distance from the original position of the blade root in the particular direction and denoted by δ .

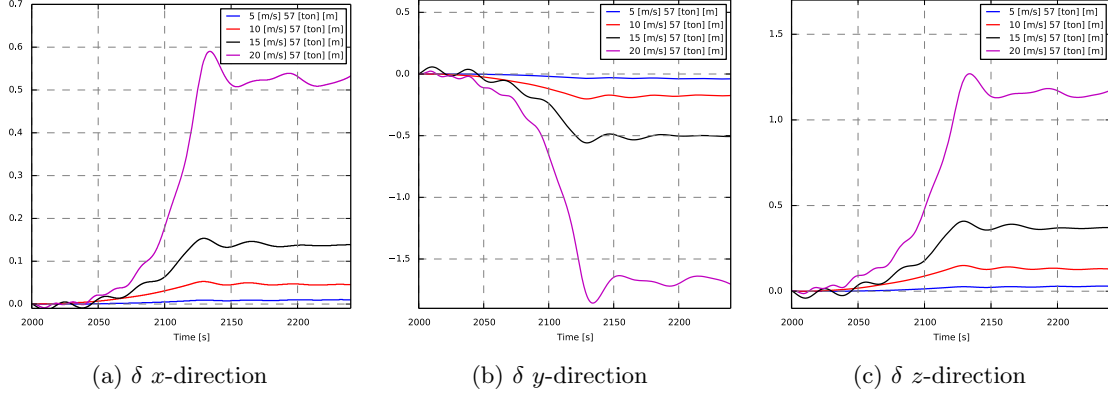


Figure 6.5: Root Displacement for different Windspeed at $\eta = \theta = 0$ with 57 ton Yoke

The first thing to notice is that the blade root moves corresponding with the ramp up of the windspeed and remains at a constant position when the wind velocity becomes constant after 60 seconds. The root displacement slightly overshoots before rotating back and finally reaching a new equilibrium position with a displacement different from the initial position. For example, the blade with a yoke mass of 57 tons in a wind velocity of 15 [m/s] and no TI for $\theta = \eta = 0$, the blade root will move 14 [cm] in x -direction, 50 [cm] into the wind in y -direction and 36 [cm] downwards in z -direction.

6.3 Verification

The *aeroelastic model* is verified by looking at the scaling of the aerodynamic forces. It is seen in Figure 6.6 that the forces F_z and F_y scale quadratically with the windspeed. The blue curve represents the particular force and the green curve the quadratic fit through the data points. This effect is expected and known from the basic lift and drag theory in Section 3.2.2. This indicates that the dynamic movement of the blade does not introduce large non-linear effects on the system.

Furthermore, the root displacement and tackline tension also scale quadratically with the windspeed, as seen in Figure 6.7. This behaviour is expected since it has already been assessed that the structural forces and the tackline tension behave similarly. The root displacement is a direct result of the loading on the system and thus also scales accordingly. These two aspects indicate that the model operates as expected and according to the theory, which provides verification of the model.

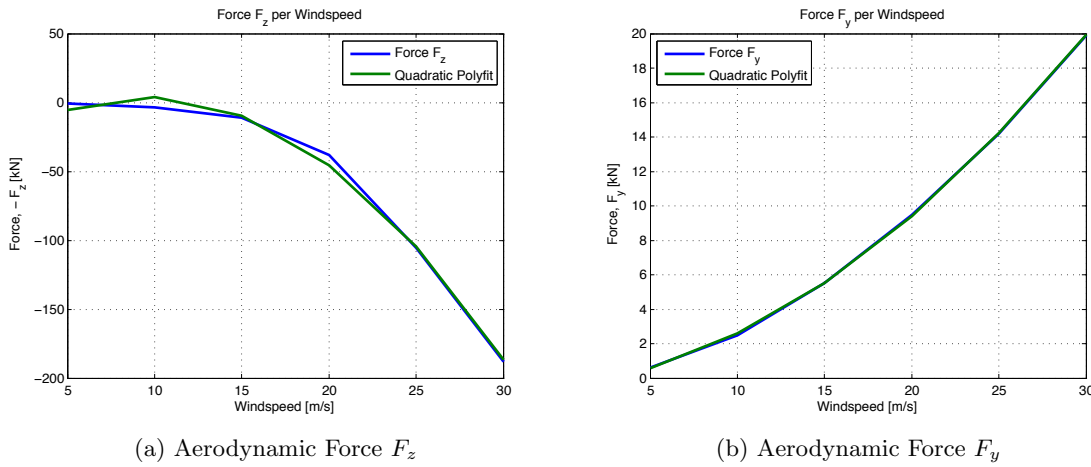


Figure 6.6: Quadratic Scaling of the Forces F_z and F_y with the Windspeed

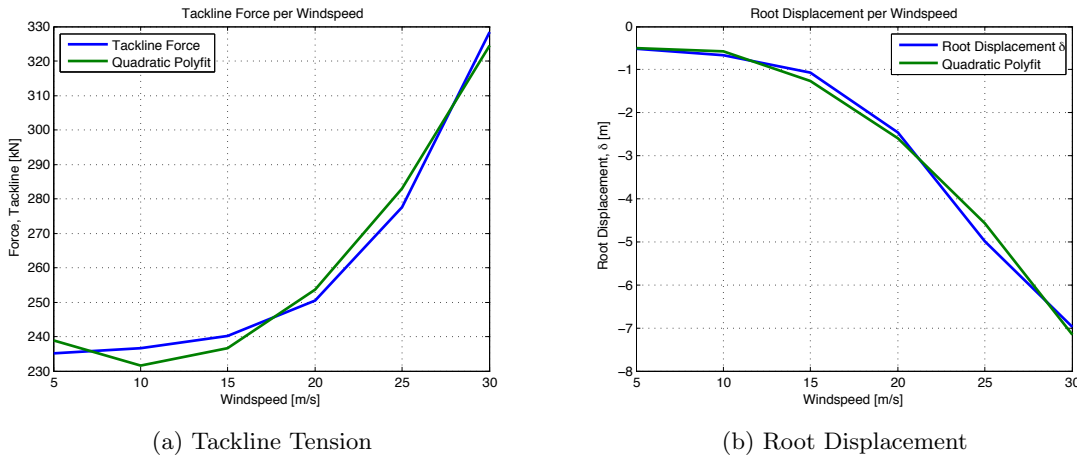


Figure 6.7: Quadratic Scaling of the Tackline Force and the Root Displacement δ

6.4 Validity Check

The initial reason of developing the previous discussed CFD model is providing a means of accurate comparison to test the crossflow principle. It can now be discussed what the validity is of the aeroelastic model created. This is relevant in order to answer the second research question: **2. what are the critical parameters affecting the blade response?**. The comparison between the CFD model and the aerodynamic model shows, in Figure 5.8, that the crossflow principle fails in accurately predicting the mean lift, lift distribution, the spanwise force and rolling moment. However there are three reasons why the aeroelastic model still proves to be a valuable model.

The first considers the enormous weight of the blade yoke combination, as the weight of the blade is approx. 43,000 kg and the yoke minimum mass is 57,000 kg, it totals over 100 tons of mass. This applies to all different pitch and yaw angles, wind conditions and hoisting configurations. From Figure 5.8 it is computed that the maximum error by

HAWC2 from all yaw angle and two pitch angles is 2 kN compared to the CFD results. It is argued that this error in the lift force is mitigated by the +1,000 kN gravitational force and thus can be neglected. The same thing holds for the rolling moments of the blade. On the contrary, the spanwise force is less affected by the gravitational force, however the loading in the x -direction is very small according to the *CFD model*, e.g. 0.5 kN, and therefore assumed it does not affect the system greatly.

Secondly, the *aeroelastic model* will be used to see the influences from several important parameters, i.e. checking how they affect the system, instead of determining absolute values. For example, it is investigate if the yoke mass increases or decreases the overall movement of the blade-cable system.

Thirdly, HAWC2 provides a very simple and computational inexpensive method of determining installation dynamics in contrast to CFD. These key arguments justify the usage of the model for investigation of certain crucial parameters by means of sensitivity check. Moreover these provide a reasonable judgement of validity.

6.5 Summary

The previous chapter presents the *aerodynamic model* which provides the answer to the last part of the first research question: **1.** *how to model the aerodynamic forces and dynamic behaviour of a hoisted wind turbine blade in different inflow angles?*. The aerodynamic forces computed in the *aeroelastic model* are based on the crossflow principle, of which the validity has been checked by the comparison of the *aerodynamic model* and *CFD model*.

This *aeroelastic model* takes the step further to determine the dynamic behaviour of the blade as a result of the aerodynamic forces by simulating the movement of the complete blade over time and analysing the root displacement. The cables are modelled as series of ultimately stiff and light weight Timoshenko beam elements interconnected with spherical joints.

The *aeroelastic model* demonstrates that the structural forces on the blade increase, similar as the aerodynamic, with higher windspeed. Analogously, the root displacement becomes larger with higher wind velocity. For zero yaw and pitch the blade rotates with the root into the wind and downwards.

Finally, the validity of the model is discussed and it is argued that under the large mass of the complete system (i.e. yoke plus blade) the error of the forces, due to the use of the crossflow principle, can be neglected. This leads to the judgement that the *aeroelastic model* is valid for the purpose of performing a parameter study. This is relevant in order to answer the second research question: **2.** *what are the critical parameters affecting the blade response?*, as is done in Chapter 7.

Chapter 7

Parameter Study

In Chapter 4, 5 and 6 the aerodynamic, CFD and aeroelastic models are presented and discussed, respectively. In this chapter the results from these models will be discussed and tested to see the influence on the blade hoisting system, in order to answer the second research question: **2.** *what are the critical parameters affecting the blade response?*. Many variables exist in a complex system such as horizontal single blade lifting and various constraints limit the situations in which the installation can be done. This chapter will discuss the conducted *parameter study* and perform task four "conduct a parameter study to determine the crucial variables of the system based on the motion of the blade".

In order to determine when the lifting can or cannot be done certain criteria must be set, which is done in Section 7.1, afterwards the many variables are divided into three main categories and its influence on the system is tested and discussed in the Sections 7.2, 7.3 and 7.4. Finally, in Section 7.5 all the obtained knowledge is used to answer the last research question: **3.** *how can single blade mounting be improved for higher wind speeds?*.

7.1 Hoisting Criteria

The main variables and parameters influencing the behaviour of a wind turbine blade in offshore installation can be categorised in: blade orientation & geometry, wind conditions and hoisting method. These three categories include, amongst others, incoming wind speed, chord length, twist, thickness and airfoil distribution as well as, cable tension, cable angles, crane geometry. Additionally, atmospheric or site specific parameters are required such as roughness length and turbulence intensity. Due to time constraints, not all of them can be tested.

The installation criteria to which the installation will be studied and optimised are: mean forces and moments, standard deviation of the loads and displacement of the root. The mean loading on the system is interesting to know since it is necessary to determine if the cables, crane, vessel and other tools are capable of handling the maximum forces and moments. The standard deviation of the loads is relevant to understand the force

fluctuations and thus the stability of the system. Finally, the root displacement is crucial to ensure safe and correct alignment for joining the bolts of the blade with the hub.

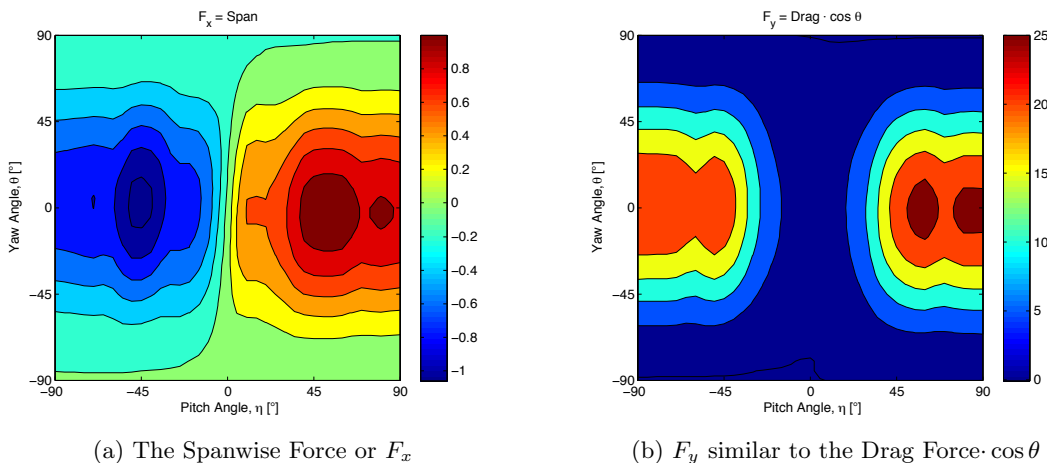
Expected modifications for optimising the blade installation are, increasing or decreasing the length of the cables, changing the yaw and/or pitch angle with respect to the incoming wind and even decreasing or altering the wind loading on the blade by improving its geometry. Such options will be tested with the developed models according to the previously set criteria.

7.2 Influence of Blade Orientation & Geometry

Throughout this research document the effect of pitched and yawed inflow on the blade has been presented. In the following part these results will be summarised and discussed, in order to provide the reader with a concise verdict on what might be unbearable situations for the system and what might be the favourable orientations of the blade with respect to, mean forces, standard deviations and root displacements.

7.2.1 Pitch, Yaw & Forces

As the wind direction is varied in the horizontal plane the model predicts that the mean load level scales with the square cosine of the yaw angle, whereas the standard deviation of the aerodynamic loads varies linearly with cosine θ . The largest loads, and the highest load variations are hence reported for wind directions perpendicular to the blade, hence $\theta = 0$.



(a) The Spanwise Force or F_x

(b) F_y similar to the Drag Force $\cdot \cos \theta$

Figure 7.1: Contour plot of F_x and F_y for $-90 < \theta < 90$ and $-90 < \eta < 90$

In Figure 7.1, 7.2 and 7.3 the forces and moments are presented in a contour plot in order to intuitively see in which orientation the blade experiences the largest and smallest forces. In Figure 7.1 the spanwise forces are largest for $\eta = \pm 45$ and $\theta = 0$, drag forces are strongest for $45 < \eta < 90$ and $\theta = 0$ and lift forces are also largest for $\eta = \pm 45$ and $\theta = 0$. In Figure 7.2 the pitching moment is highest for $\eta = \pm 90$ and $\theta = 0$, the rolling

moment is maximum for $\eta = \pm 45$ and $\theta = 0$ and finally the yawing moment is largest for $45 < \eta < 90$ and $\theta = 0$. All forces and moments are lowest for $\theta = \pm 90$.

In order to comprehend the loading on the blade, the previous observations are briefly explained and compared to expectations. The generally declining loading when yawing the flow corresponds with the expectations as the blade will generate lower lift- and drag forces. The maximum lift force and rolling moments for $\eta = \pm 45$ are expected due to the fact that in this orientation the largest part of the blade has an angle of attack corresponding to the highest lift coefficient. Finally, the maximum drag force and yawing moment for $\eta = \pm 45$ are explained by the fact that in this orientation the blade has the largest frontal area and generates the largest wake.

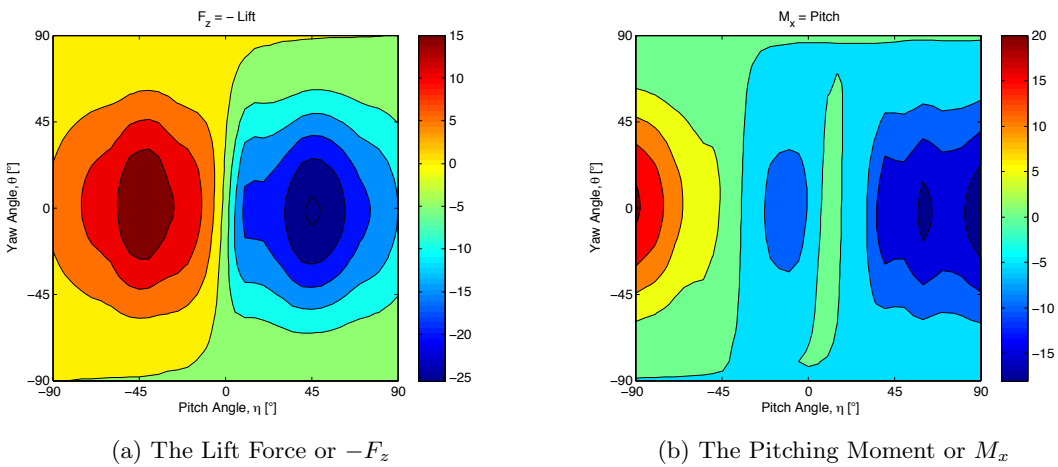
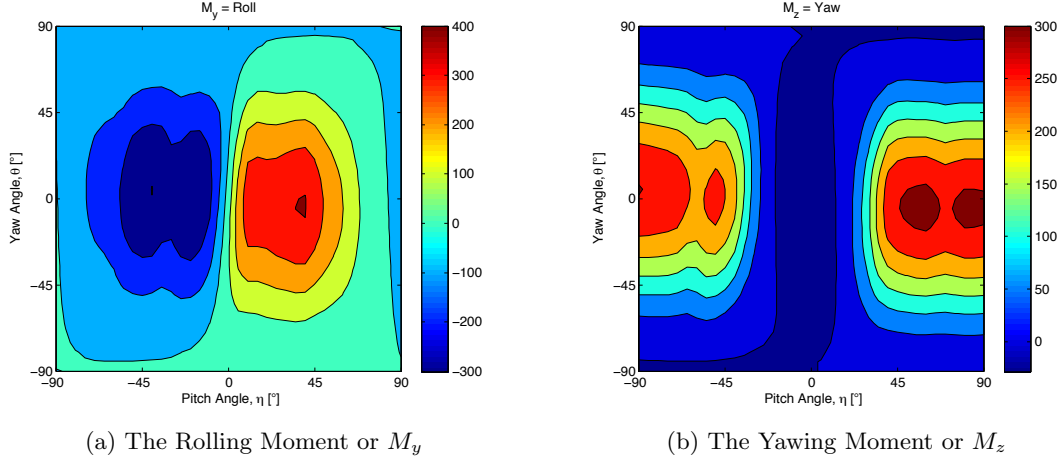


Figure 7.2: Contour plot of F_z and M_x for $-90 < \theta < 90$ and $-90 < \eta < 90$

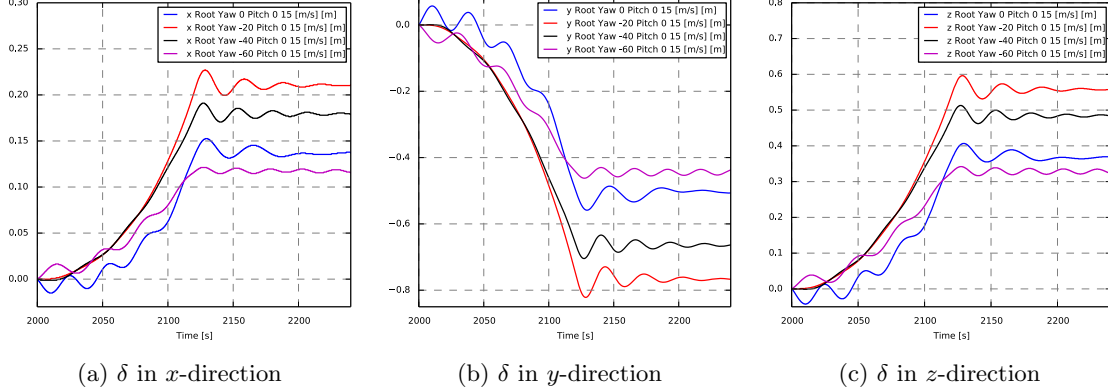
From the figures in Section 4.5.1 it can be concluded that the absolute standard deviation increases for increasing pitch angle, due to the increasing main loading on the blade. The std decreases when increasing the yaw angle. Considering only the mean and standard deviation of all the forces and moments, the most favourable pitch angle to hoist the blade would be $\eta = 0$, due to the minimum loading. Most unfavourable seems to be $\eta = \pm 45$, since the highest forces and moments are expected in this orientation. Finally, solely based on the mean loading, $\theta = \pm 90$ seems to be most favourable, as it endures the smallest forces. Unfortunately changes in the wind direction are inevitable and the vessel locations are limited with respect the tower, such that the yaw angle θ is usually not controllable.

7.2.2 Pitch, Yaw & Root Displacement

The influence of pitch and yaw will be identified by determining the root displacement, δ , over time in a wind velocity of 15 [m/s], 1% TI and with a 57 [ton] yoke. Figure 7.4 shows the movement of the root in different negative yaw orientations, hence $\theta < 0$ is rotation of the inflow towards the tip, as defined in Section 2.4.2. The blue line represents zero yaw and angles up to -60° are chosen since beyond this point the uncertainty of the crossflow principle becomes too high. It is identified that with increasing yaw the root displacement

(a) The Rolling Moment or M_y (b) The Yawing Moment or M_z **Figure 7.3:** Contour plot M_y and M_z for $-90 < \theta < 90$ and $-90 < \eta < 90$

first increases for -20° and -40° yaw and decreases when yaw increases towards -60° . This corresponds to the expectations and results in Section 7.2.1 that show that the forces decrease with larger θ . Note that the blade displacement in y -direction remains negative implying that the root moves into the wind, i.e. positive around the z -axis.

(a) δ in x -direction(b) δ in y -direction(c) δ in z -direction**Figure 7.4:** δ for $\theta < 0$, with $\eta = 0$, 15 [m/s] Wind, 57 [ton] Yoke & 1% TI

Noteworthy is the increasing fluctuating movement of the blade with positive yawing, as seen in Figure 7.5. Moreover, increasing the yaw angle positive, hence rotated towards the root, changes the sign of the displacement. In other words, the root moves out of the wind and upwards, since $\delta_y > 0$ and $\delta_z < 0$, which agrees with what is intuitively expected. The event that the blade rotates negative around the z -axis for $\theta \leq 0$ and positive for $\theta > 0$ indicates that the point where the forces and moments act shifts in direction of the root when yawing the flow towards the root.

Figure 7.6 visualises the effect of the pitch angle on the blade-cable system with 15 [m/s] wind velocity, 1% TI and zero yaw. Zero degree pitch angle is defined when the airfoil chord line is horizontal as seen in Figure 2.5. The blue line represents 0° pitch and shows the least movement, larger displacements are seen with 90° (cyan) and 45° (magenta)

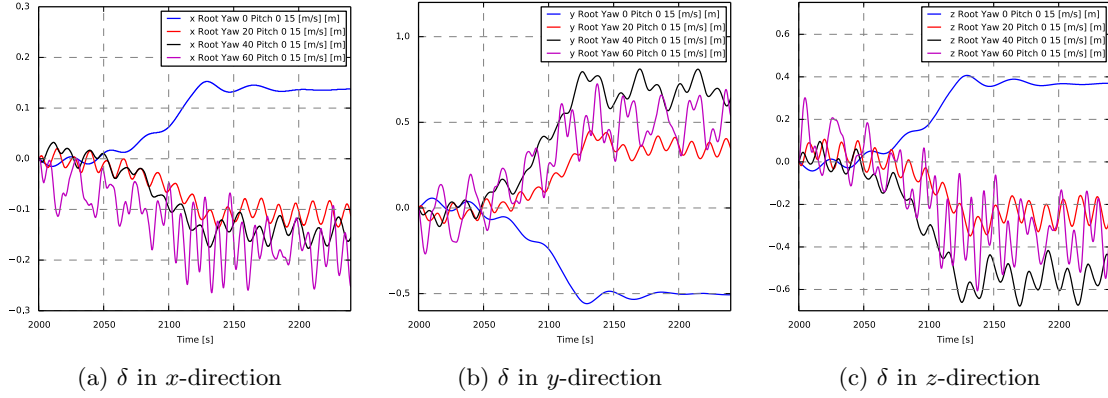


Figure 7.5: δ for $\theta > 0$, with $\eta = 0, 15 \text{ [m/s]}$ Wind, 57 [ton] Yoke & 1% TI

pitch. This agrees with intuitive aerodynamic knowledge since large pitch angles increase the drag force due to frontal area and flow separation as well as with the forces seen in the previous Section 7.2.1. Increasing the pitch angle does not change the direction of the rotation, as in all cases the blade rotates with the root into the wind, hence positive around the z -axis. Remarkable is the slightly unsteady root displacement, δ , for $\eta = -90^\circ$ (red) and strongly unsteady for $\eta = -45^\circ$ (black). This could be appointed to the fact that in this pitch angle the movement of the blade causes the angle of attack to change around the region where the force coefficient slope is steepest and thus strongly changes the loading. Due to the violent swinging of the blade up to 2 meters it is not recommended to perform blade installation with a -45° pitched blade.

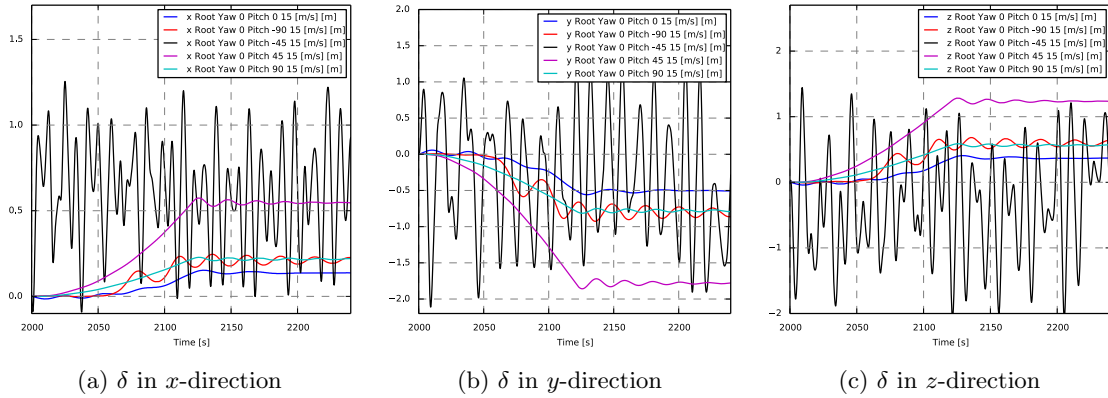


Figure 7.6: δ for different η , with $\theta = 0, 15 \text{ [m/s]}$ Wind, 57 [ton] Yoke & 1% TI

Previously it is seen that the yaw and pitch angle have a significant effect on the behaviour of the blade during installation. Siemens WP is currently performing the blade hoisting with a -90° pitched blade, ergo simulations are done for different yaw angles with $\eta = -90$. Figure 7.7 demonstrates the root displacement, δ , for positive yaw angles. Again, the rotation of the blade remains such that the root moves into the wind for all yaw cases. Distinguishable is the lower variations of the root position for positive yaw in $\eta = -90$ than for $\eta = 0$ as seen in Figure 7.5. Furthermore, yawing the flow from

zero to 20 degrees does not seem to change δ , however further increasing the yaw angle reduces the displacement. As a result, the least movement is seen for 60° yaw and thus is recommended as far as the vessel and crane allow.

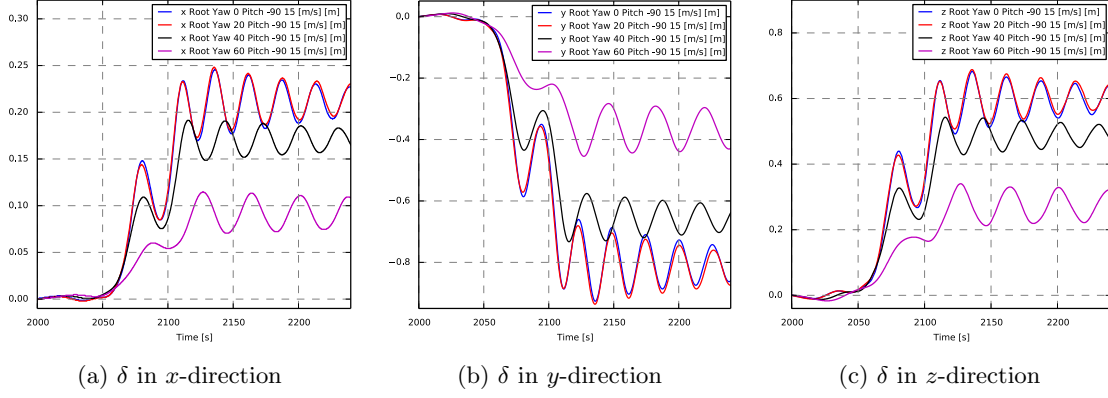


Figure 7.7: δ for $\theta > 0$, with $\eta = -90, 15 \text{ [m/s]}$ Wind, 57 [ton] Yoke & 1% TI

Finally, negative yawing in $\eta = -90$ is assessed in Figure 7.8 where it is simply seen that increasing yaw decreases the root displacement. This is different from $\eta = 0$, where the root displacement first increases and decreases after a yaw angle of -40° , as seen in Figure 7.4. However, it leads to the similar recommendation; installation in larger yaw angles seems to be preferable.

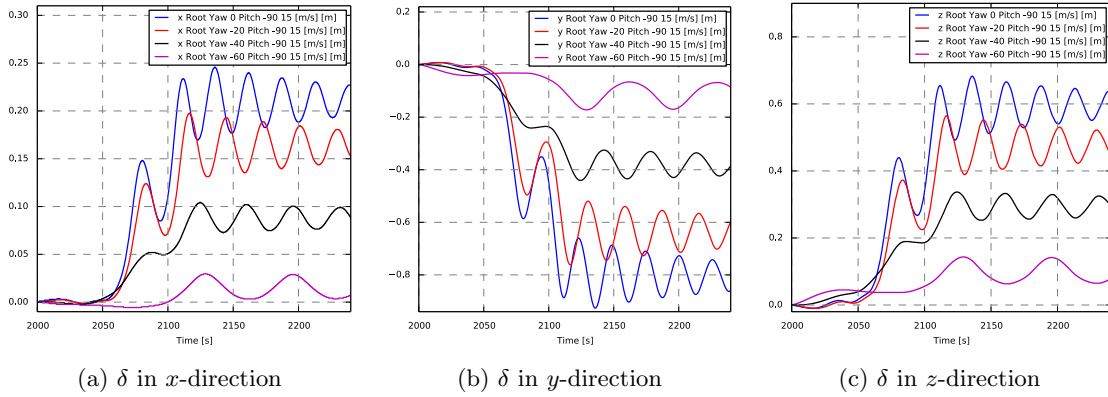


Figure 7.8: δ for $\theta < 0$, with $\eta = -90, 15 \text{ [m/s]}$ Wind, 57 [ton] Yoke & 1% TI

7.2.3 Blade Geometry & Mean Forces

The Gurney flap added on the DTU 10MW reference blade changes the geometry in such a way that the flow behaves differently. The influence of such changes in the blade geometry need to be investigated since the geometry of the Siemens B75 is significantly different.

In Section 5.4.6 the effect of the Gurney flap has been tested. Results show that the trailing edge device unmistakably increases the wake structure behind the blade leading

to higher loading and presumably also higher standard deviation of the loading. This leads to the interpretation that the effect of the blade geometry is of great influence on the forces and moments on the blade. These results imply that a slender blade is most favourable.

7.3 Influence of Wind Condition

Not only the blade orientation but also the wind conditions are of great importance for the stability of the blade. Both the CFD model as well as the aerodynamic model have proven the effects of windspeed and turbulence on the blade. The effect on the dynamic system is investigated with the aeroelastic model in this section. Besides velocity and turbulence intensity, TI, also the influence of gusts on the system is tested.

7.3.1 Windspeed & Tackline Forces

From the developed models as well as from an analytical point of view it is proven that the mean loading scales quadratically with the windspeed. The tackline tension also scales with U_∞^2 , as seen Section 6.2.1, which is a direct result of the loading, and also holds in turbulent conditions, as presented in Figure 7.9. The maximum tackline forces increase significantly with higher TI hence, the maximum tackline tension thus scales with the square of the maximum expected wind speed. Obviously, it should be favourable to install the blade in low windspeed conditions, however since the importance lies in decreasing the weather downtime of the installation, higher wind velocities are inevitable and solutions are required by changing either the blade orientation or hoisting method.

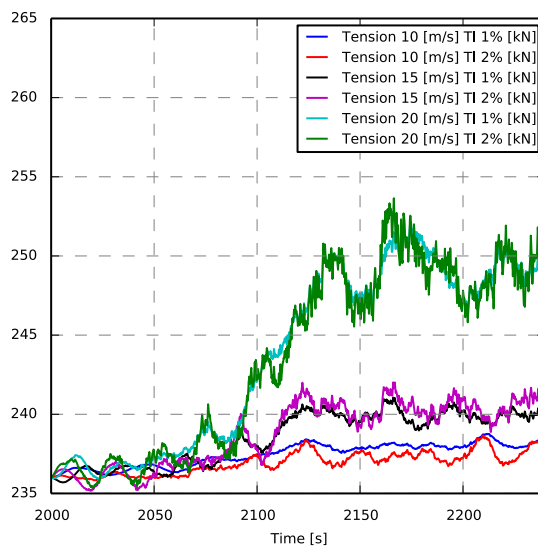


Figure 7.9: Influence of TI on the Tackline Tension for different Wind velocities at $\eta = \theta = 0$

7.3.2 Turbulence Intensity & Root Displacement

As seen from Section 5.4.5, when the wind speed variation caused by atmospheric turbulence is taken into account, the reported maximum aerodynamic loads are significantly larger than what would result by considering only a constant wind flow. Furthermore from Section 4.5.3 it is understood that the standard deviation of the forces scale linear with TI. The introduction of turbulence will lead to a stochastic movement of the blade and no equilibrium state of the blade is reached, as displayed in Figure 7.10, where five different turbulence intensities are tested from 1% up to 10 %.

The blue line represents the lowest TI and indicates that the root clearly moves from its initial position, i.e. zero, to a final position, due to the velocity ramp up. However when increasing the TI above 5% the stochastic movement of the root is so large that the initial movement due to the windspeed is not seen anymore and all movement is caused by the turbulence. A common TI during offshore installation would be 5%, which will make the blade root vibrate with approximately 20 [cm]. Note, all calculations are done with a yoke mass of 57 tons. The effect of increasing this weight will be discussed in Section 7.4.

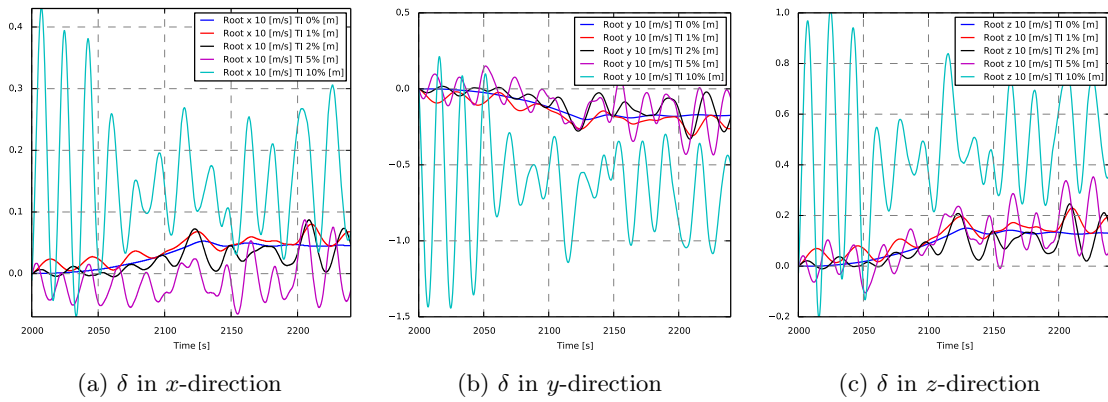


Figure 7.10: Influence of TI on δ at $\eta = \theta = 0$ for 10 [m/s] Wind

For the blade pitched -90° , as done by Siemens WP, the root displacement varies with 40 [cm] at TI 5% and a windspeed of 15 [m/s].

7.3.3 Gusts & Root Displacement

In offshore sites, gusts are a common phenomenon and thus the effect on the installation should be investigated. According to IEC 61400-1 wind turbine design standards[15], an extreme operating gust is simulated with the following expression,

$$u(z, t) = u(z, t) - 0.37A \sin\left(\frac{3\pi(t - t_0)}{T}\right) \left(1 - \cos\frac{2\pi(t - t_0)}{T}\right) \quad (7.1)$$

where, T [s] is the time duration, t_0 [s] the starting time and A [m/s] the amplitude of the gust. Figure 7.12(a) shows the two different gusts: $A = 2$ (blue) and $A = 5$ (red) as well as the aerodynamic force F_y (drag) and F_z (lift). It is immediately recognised

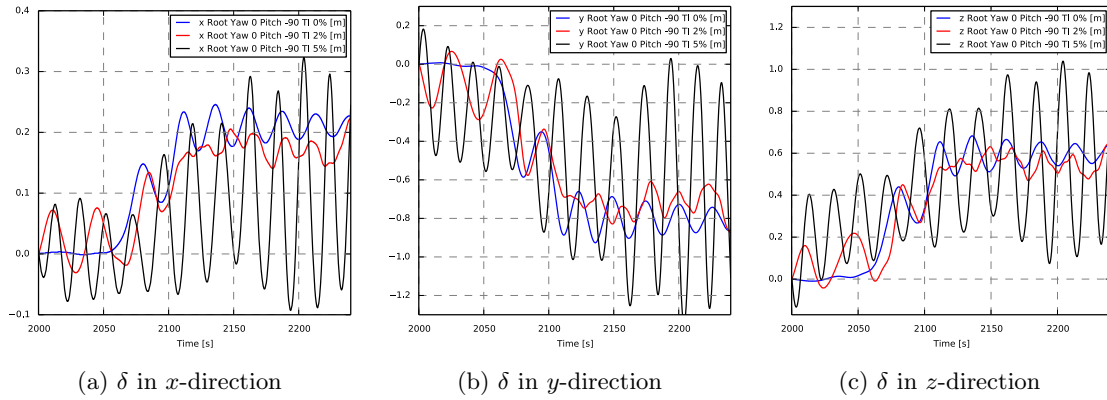


Figure 7.11: Influence of TI on δ at $\eta = 0$ and $\theta = -90$ for 15 [m/s] Wind

that the resulting aerodynamic forces behave with an identical trend as the windspeed. From Figure 7.12(b) it is observed that the root undergoes a displacement up to 20 [cm] for $A = 2$ and [70] cm for $A = 5$. As the occurrence of gusts can not be affected it is recommended to increase the blade installation stability by means of blade orientation and hoisting method.

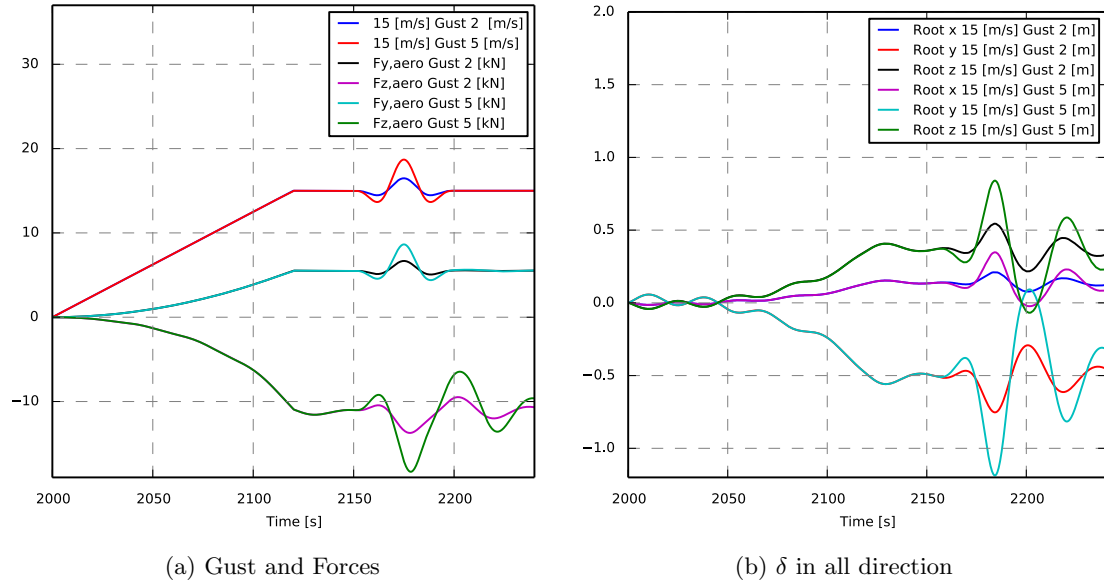


Figure 7.12: Forces & Root Displacement for Gusts $A = 2$ and 5 at $\eta = \theta = 0$

7.4 Influence of Hoisting Method

The effects of certain installation specific parameters are studied with the aeroelastic model. A generally much discussed topic is the influence of the point where the vertical hoisting wire splits into two, in this document defined as the Δ point. This will be

assessed as well as the influence of the yoke mass.

7.4.1 \triangle Point & Root Displacement

The configuration of the cable system is of great importance for the stability of the system. The vertical wire from the crane runs down and splits into two wires. This point is defined as the \triangle point and is illustrated in Figure 7.13. The location of this point, h , is an important parameter in the stability of the single blade installation. The angle ξ is defined as the angle at which the two wires split and its influence is also analysed. Furthermore, l is the length of the diagonal cable and b is the distance of the attachment of the cable to the CoG. The first mode of this system is the side to side swinging in spanwise direction where no rotation of the \triangle point exists and therefore similar to a simple pendulum. The second mode is essence similar to a double pendulum, where the \triangle point acts as a hinge. This second mode is much affected by the location of the \triangle point.

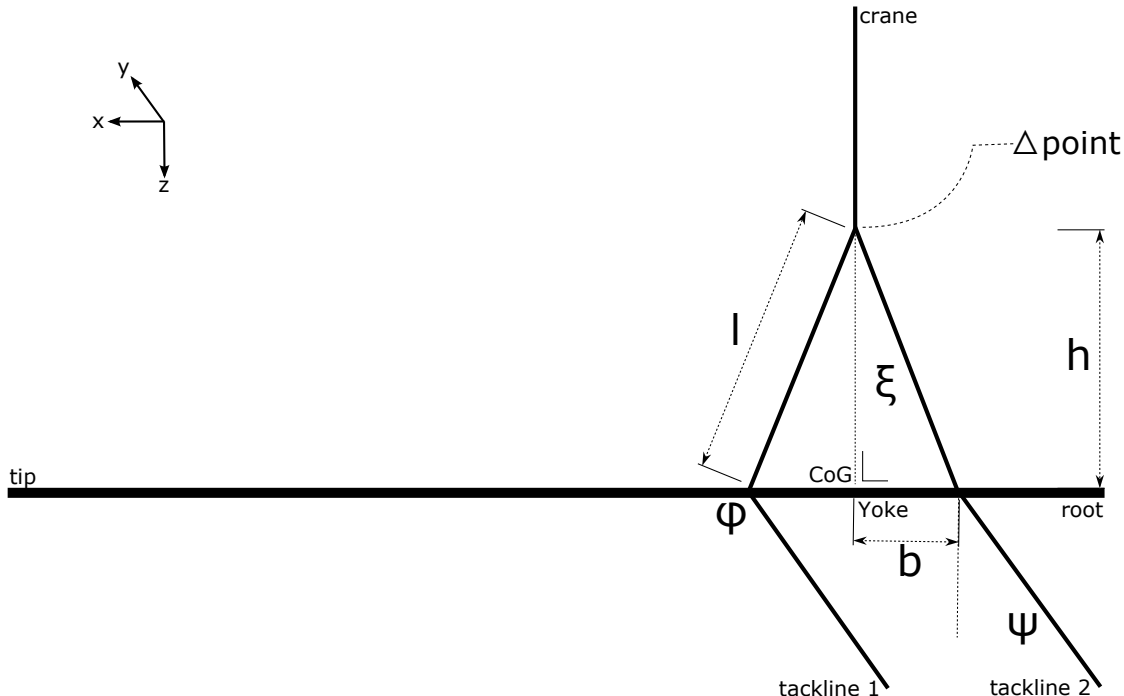


Figure 7.13: Definition of \triangle point, Cable Lengths & Angles

The system becomes uncontrollable when their is no tension is one of the cable. Therefore this is considered the most important criterium. When looking at the steady-state situation of the system it can be stated that the body below the \triangle point acts like one solid body, such that the \triangle point behaves as a hinge and cannot transfer any moment. From the force equilibrium, due to a constant external aerodynamic moment applied on the CoG, in Figure 7.14, the equations of motion can be derived.

Figure 7.14(a) is the part of the system above the \triangle point and Figure 7.14(b) is the part below the \triangle point. δ_z is the root displacement in z -direction and mg is the blade

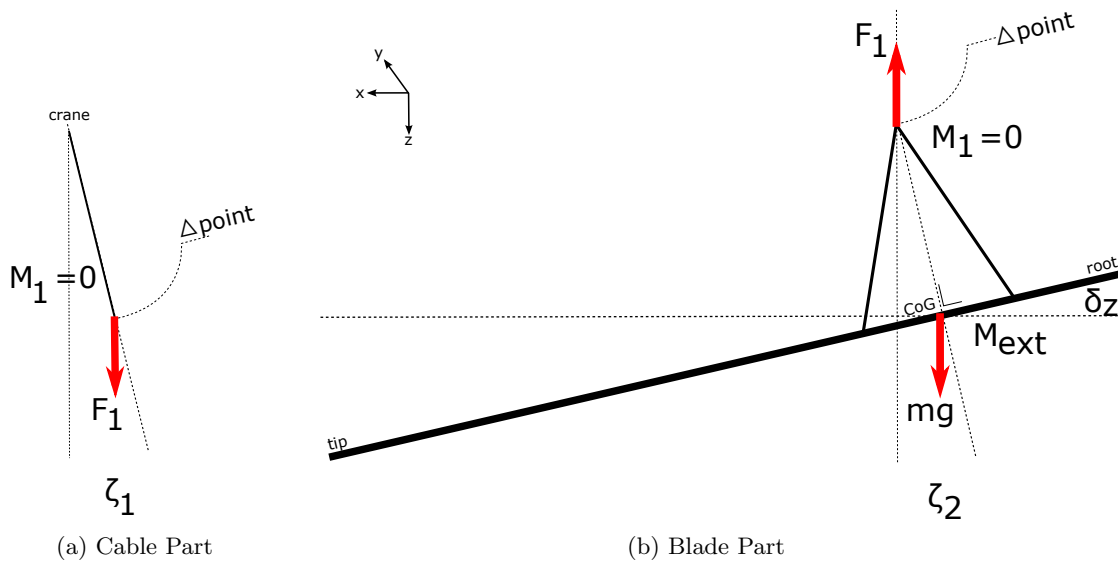


Figure 7.14: Force Equilibrium of the Blade-Cable System

mass times the gravitation. From Figure 7.14(a) the equations of motion and equilibrium state can be derived as follows. The hinge (i.e. Δ point) can not hold any moment such that, $M_1 = 0$ and the equilibrium is $\zeta_1 = 0$. Furthermore, the force equilibrium in Figure 7.14(b), around the Δ point leads to, $M_{ext} - mg \cdot h \cdot \sin \zeta_2 = 0$, with a small angle approximation this yields, $M_{ext} - mg \cdot h \cdot \zeta_2 = 0$. Rewriting the previous equation leads to, $\zeta_2 = \frac{M_{ext}}{mg \cdot h}$. Finally, from the angles ζ_1 and ζ_2 the root displacement δ_z can be determined. Therefore it can be concluded that the steady root displacement scales with h^{-1} for a constant external aerodynamic moment applied in the CoG. As a result the system becomes stiffer for larger h (i.e. higher Δ point).

This conclusion will be verified with the *aeroelastic model* by changing the parameters of the blade-cable system that determine the location of the Δ point. Five different configurations are tested and listed in Table 7.1. Configuration A is the system which has been used in all previous simulations. The height h is increased by decreasing the angle ξ and base length b (B and C) or by increasing the cable length l (D and E).

Table 7.1: Different Configurations of the Single Blade Hoisting System

Config.	ξ [°]	l [m]	b [m]	h [m]
A	60	9	7.79	4.50
B	30	9	4.50	7.79
C	10	9	1.56	8.86
D	60	15	12.99	7.50
E	30	15	7.50	12.99

Figure 7.15 displays the displacement of the root for the different configurations. Configuration A (blue) is the system which is used in previous studies and shows the largest δ in all directions. Moving the Δ point upwards by increasing h , decreasing the angle ξ and reducing b leads to lower root displacement, as represented by the red curve and configu-

ration B. Increasing h even further while maintaining the same length l , does not decrease δ , on the contrary, it increases the fluctuations of the root, represented by configuration C and the black curve. Configuration D (purple) with a longer cable length l and $\xi = 60$ does not lower the root displacement, but does decrease the root fluctuations. Finally, configuration E (cyan) with $l = 15$, $\xi = 30$ and increased h compared to D, introduces more root fluctuations although lowers the mean displacement. From this analysis it can be argued that moving the Δ point up lowers the mean root displacement and increasing the angle ξ makes the system more stable due to reduction of the root fluctuations. This is caused by the fact that the tacklines are further apart from the CoG and thus have a bigger arm to compensate the moments. These results are as expected since it agrees with the previous conclusion drawn from the equilibrium derivation in Figure 7.14.

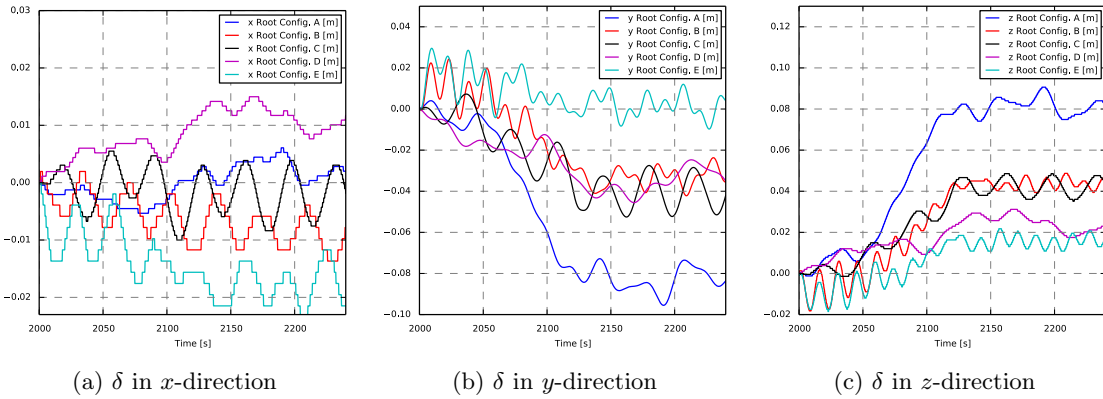


Figure 7.15: Influence of Δ , ξ and h on δ , for 10 [m/s] and 57 [ton] Yoke

7.4.2 Yoke Mass & Root Displacement

The yoke supporting the blade and holding it in position needs to be able to withstand the large mass of the blade and thus is built out of industrial steel, hence the blade yoke has a tremendous weight. The effect of this weight is much discussed and needs to be designed accordingly. Therefore the influence on the root displacement, δ , is simulated and displayed in Figure 7.16. Note that the location of the yoke mass is not varied and is simply added as a concentrated mass in the centre of gravity (CoG) of the blade as seen in Figure 7.13.

The addition of mass to the yoke stabilises the blade installation, as observed from Figure 7.16, since the root displacement seems to fluctuate less with a yoke mass of 57 (red) and 77 (black) tons. Consequently, it could be argued that increasing the yoke mass is favourable, provided that it does not surpass the limits of the crane and cables. This observation agrees with the conclusion drawn from the equilibrium derivation in Figure 7.14, since $\zeta_2 = \frac{M_{ext}}{mg \cdot h}$, meaning that increasing mg (i.e. the mass of the blade) leads to smaller ζ_2 and thus also lower root displacement δ .

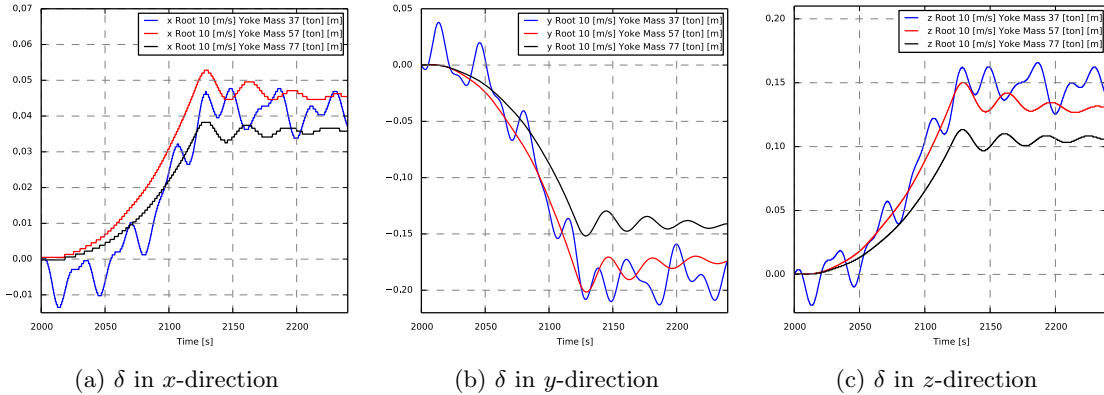


Figure 7.16: Influence of Yoke Mass on Root Displacement for 10 [m/s] Wind & 1% TI

7.5 Hoisting Recommendations

The *aeroelastic model* is used as an answer to the first research question. Previously in this chapter the answer to the second research question, **2. what are the critical parameters affecting the blade response?** is provided. This section will discuss the *hoisting recommendation* and perform task five "test the system to indicate the influence of key parameters using a sensitivity study".

The mean forces, standard deviation of the loading and root displacement are used to demonstrate the influence of key parameters in the single blade installation procedure.

Firstly, it is displayed that the aerodynamic forces are lowest for zero pitch and $\pm 90^\circ$ yaw. Furthermore, the root displacement seems to be more stable and minimum for a flow yawed towards the tip and high pitch angles of -90° .

Secondly, for the influence of the wind condition, it was seen that higher windspeed increase the aerodynamic forces, cable tension and root displacement. Moreover, when increasing the turbulence intensity to 10% the displacement of the root becomes chaotic and fully dominated by the turbulence. Gusts temporarily disturb the displacement of the root and aerodynamic forces with a similar trend as the distribution of the gust.

Finally, the influence of the hoisting method are investigated by studying the effect of the yoke mass and cable configuration on the root displacement. Increasing the yoke mass seems to stabilise the movement of the blade and reduce the displacement of the root due to higher correcting gravitational force. Furthermore, increasing the distance between the point where the wires split and the CoG lessens the mean root displacement, however increases the fluctuations of the root. Subsequently, increasing the angle between the two wires makes the system more stable by reduction of the root fluctuations. Both of these observations are expected and agree with the derivation of the force equilibrium in Figure 7.14.

The sensitivity and influence of the previous summarised parameters gives the ability to answer the third and final research question, **3. how can single blade mounting be improved for higher wind speeds?**. It must be understood that several of the previous parameters cannot be altered during the installation, e.g. yaw angle, windspeed and turbulence, due

to the orientation of the vessel with respect to the wind and the fact that reduction of the weather downtime is required and thus installation needs to be done in higher windspeed and turbulence. Therefore, only hoisting recommendation are done on the parameters which can be altered: pitch angle, cable configuration and yoke mass.

First, for the pitch angle it is recommended to avoid the blade orientation of -45° pitch, since this subjects the largest forces in the tacklines and causes chaotic displacement of the root. It is recommended to hoist the blade with $\pm 90^\circ$ pitch as it is judged that installation would be most predictable in these orientations, since the wind can come from all yaw angles (e.g. $\theta = 180$). Although it does not experience the lowest mean loading, it does seem to be the most controllable, since the rotation of the blade for different yaw remains the same and root fluctuations are lower during turbulence compared to -45° pitch. Furthermore, the loading for 0° pitch is more unpredictable due to the three-dimensional effects over the blade, which also leads to the recommendation of installing in -90° pitch.

Second, for the cable configuration it is recommended to increase the distance between the yoke plus blade CoG and the point where the vertical hoisting wire split into two, in order to decrease the mean root displacement. Furthermore, it is recommended to increase the angle between the two wires such that the distance between the points of attachment on the blade is largest, in order to lower the fluctuations of the root. The system is least damped in the side to side spanwise movement due to the fact that it is not constrained in this direction. It is recommended to have the tacklines attach to the blade as wide apart as possible to slightly constrain this movement.

Last, a heavier yoke indicates lower root movement and thus a more stable blade, caused by the larger gravitational force. It is recommended to increase the yoke mass to the point where its weight does not exceed the maximum allowable tension in the wires and maximum loading of the crane including the safety margin.

Chapter 8

Conclusions & Recommendations

This document discusses the master thesis for the Technical University of Delft and Denmark Technical University. The research subject based on wind turbine rotor blade installation in high wind speeds incorporates several academic elements that make it suitable for a MSc thesis. It contributes to the current knowledge within wind energy, as it is of great relevance to reduce the Levelised Cost of Energy of offshore wind. Research in the field of wind turbine blade hoisting has been conducted, but lacks investigation of dynamics on the blade and its response. The associated literature provides a good estimate of the order of magnitude and is used to verify the results obtained in this study. Furthermore, literature research lead to valuable knowledge and understanding of the aerodynamic effects on the blade in order to predict the accuracy of results from numerical modelling. Good understanding has been achieved in the field of aeroelastic tools, such that the appropriate software is chosen to tackle the presented problem. This thesis study has been conducted in order to answer the following research questions:

1. How to model the aerodynamic forces and dynamic behaviour of a hoisted wind turbine blade in different inflow angles?
2. What are the critical parameters affecting the blade response e.g. orientation, turbulence and gusts?
3. How can single blade mounting be improved for higher wind speeds?

The first question can be considered the most important and time consuming, therefore most of the literature reviewed covers the field of aerodynamic theory and analysis. The developed simulation models will be used to answer the second and third question in order to find possible ways of improving the future installations methods for operation in high wind speeds.

8.1 Conclusions

In order to achieve the aforementioned goals, it is necessary to model all aerodynamic dependencies in an aeroelastic simulation. The aeroelastic model used is the multibody dynamic code HAWC2 [19], which is developed at DTU Wind Energy. The code uses lift- and drag coefficient look-up tables and has corrections for small yaw misalignment, nonetheless these corrections do not hold for large yaw angles, proven in the research conducted. HAWC2 is based on the *crossflow principle* which states that mean aerodynamic forces and moments scale with $\cos^2 \theta$, where θ is the wind yaw angle. The conclusions drawn in this thesis study are embedded in the answers to the three research questions. In this section the research questions will be discussed and answered.

1. How to model the aerodynamic forces and dynamic behaviour of a hoisted wind turbine blade in different inflow angles?

The developed *aerodynamic model* in the HAWC2 code, is used to find an answer to the first research question. The model based on the simple crossflow principle is validated using computational fluid dynamic analysis. From the *CFD model* the following conclusions are drawn:

- Verification of the results by a means of a computational fluid dynamic analysis indicates that the crossflow principle at the basis of HAWC2 is not sufficient in determining the mean forces on the blade. This is mainly caused by the fact that the crossflow principle does not hold for non-straight blades with large twist, which leads to a highly three-dimensional flow.
- From the computational fluid dynamic analysis it is observed that in the cases of a yawed inflow of 20° to 60° the vortex structure behind the blade is remarkably larger for blade stations close to the root than for the un-yawed case.
- It is assessed that in increasing yawed inflow the streamlines are strongly bended in spanwise direction instead of chordwise direction.
- Moreover, the region of negative wall shear stress, hence flow reversal, increases with larger yaw angles, however reaches a saturation point and decreases when the yawed inflow becomes larger than 40° .
- The growing spanwise crossflow over the blade when increasing the yaw angle leads to destabilisation of the chordwise flow and ultimately earlier flow separation.
- The basis of HAWC2 lies in the computation of the force based on 2D force coefficients and limits the model to predict the rising drag force induced by earlier flow separation and thus leads to the underprediction of the forces.
- Changing the blade geometry by adding a Gurney flap substantially increases the size of the wake in zero pitch and inevitably leads to large loading on the blade.

The *aeroelastic model* takes a step further to determine the dynamic behaviour of the blade as a result of the aerodynamic forces by simulating the movement of the complete blade over time and analysing the root displacement. The validity of the model is sufficient for performing a parameter study and to answer the second research question.

2. What are the critical parameters affecting the blade response?

The *aeroelastic model* is used to answer to the first research question. The mean forces, standard deviation of the loading and root displacement are used to demonstrate the influence of key parameters in the single blade installation procedure, to answer the second research question. It is assessed that when considering the dynamic blade-cable system the aerodynamic forces, tackline tension and root displacement scale quadratically with the windspeed. The parameter study in the aeroelastic model leads to the following conclusions:

- It is identified that with increasing yaw, the root displacement initially increases, however decreases when yaw increases towards a yaw angle of 60° .
- It is noted that yawing the inflow towards the root there exists higher fluctuating movement of the root and the blade is rotated with the root out of the wind. While for zero yaw and yawing towards the tip the blade rotates with the root into the wind.
- Pitching the blade -45° leads to strong unsteady displacement of the root.
- The impact of the turbulence intensity on the displacement of the root grows to such an extent that beyond 10% the displacement of the root is completely dominated by the turbulence intensity and not the windspeed.
- Adding mass to the yoke stabilises the blade installation, since the root displacement fluctuates less.
- Raising the point where the hoisting wire splits decreases the mean root displacement. Increasing the angle between these two wires reduces the root fluctuations.

3. How can single blade mounting be improved for higher wind speeds?

The sensitivity and influence of the previous summarised parameters gives the ability to answer the third research question. This is done for the following parameters: pitch, yoke mass and cable configuration, since these parameters can be defined in the design of the blade lifting procedure.

- It is recommended to avoid the blade orientation of 45° pitch, since this subjects the largest forces in the tacklines and causes chaotic displacement of the root. It is recommended to hoist the blade with 90° pitch as it is judged that installation would be most predictable in this orientation.

- It is recommended to increase the yoke mass to the point where its weight does not exceed the maximum allowable tension in the wires and maximum loading of the crane including the safety margin.
- It is recommended to increase the distance between the CoG and the point where the vertical hoisting wire split into two as well as the angle between the two wires, in order to decrease the root displacement.
- Maximising the distance between the attachment point of the tacklines on the yoke to the centre of gravity is recommended as it increases the arm and thus improves the stability by better constraining the yawing moment.

The next Section 8.2 will give recommendations for further research in the line with the research conducted for this thesis.

8.2 Recommendations

The recommendation regarding future research will be discussed and subdivided into aerodynamic and dynamic modelling improvements. For recommendation on blade installation see Section 7.5.

Aerodynamic Modelling

Firstly, the recommendations for better modelling of the aerodynamic complexity are reviewed. In this thesis study the *aerodynamic* and *aeroelastic* model, developed with HAWC2, are restricted to a first order steady representation of the single blade installation system, and hence the aerodynamic loading and movement it experiences. For that reason the *CFD model* is created to test the validity of the aerodynamic crossflow principle, which underlies the HAWC2 models. This comparison has indicated the complexity of the flow over the blade and the presence of strong three-dimensional effects, which HAWC2 is unable to simulate.

This complexity is mainly caused by the large twist, prebend, taper and airfoil distribution of the blade together with the extremely yawed and pitched inflow. For future research it is therefore recommended to reduce the complexity of the flow problem and start from modelling a straight non-tapered blade in yawed flow and investigate the effects on transition, flow separation and force fluctuations. From there increase the complexity step by step by introducing pitch, twist, taper, different airfoils and turbulence.

Analogously, it was seen that the Gurney flap had tremendous effect on the flow, therefore CFD analysis of the actual Siemens B75 blade is recommended if the aerodynamic forces and consequently the blade behaviour want to be known accurately.

The results obtained from the *aerodynamic model* indicated that the DTU blade pitched $\pm 45^\circ$ are significantly higher than for $\eta = \pm 90^\circ$ especially for the lift force, as a result is recommended to do a 3D CFD analysis of the blade in this orientation.

The high-fidelity CFD analysis done in this study proves to be more accurate in modelling the complex flow, than HAWC2, however it is limited to a steady-state solution, leading to

the incapability of modelling the time-varying three-dimensional effects and determining the importance of vortex shedding. The current research only considered the magnitude of the fluctuations, however the frequency of these fluctuations is at least of equal importance. Hence, it is recommended to conduct large eddy simulations in order to investigate the difference between standard deviations due to TI and vortex shedding. However, the reader should be aware that such analysis are extremely computational expensive.

From the steady CFD results it is seen that large wakes are generated, presumably including strong unsteadiness, with certain yaw angles, e.g. $\theta = 30$. It is recommended to do transient unsteady analysis for these cases in order to better understand the flow phenomenon present. Additionally, these simulations are recommended to be done with computational fluid dynamics since the highly yawed flow does not 'see' an ordinary airfoil but a rather arbitrary shape; making the flow complicated to such a degree that simple engineering models might be incapable of simulating the problem. These CFD simulations could make use of an adjoint solver[7] in order to perform a sensitivity study to investigate the effect of yaw on the flow phenomena such as transition and separation.

This research concluded the inadequate performance of the crossflow principle by comparison of the forces and moments between HAWC2 and CFD and discussed the discrepancies by analysing the streamline pattern. For more thorough understanding of the source of the error in the crossflow principle a transient 2D CFD airfoil analysis is recommended to compare with the HAWC2 results.

Dynamic Modelling

Second, recommendations considering the dynamic system of single blade installation are pointed out. The *aeroelastic model* is based upon the crossflow principle thus holding similar recommendations as mentioned earlier. Despite the contrary, this model was used to model blade movement and can be improved with the following recommendations.

All cables are modelled using 1 meter long massless Timoshenko beams interconnected with spherical joints. This is not the ideal representation of a cable and it is recommended to investigate the non-linear effects of the cables due to their own weight and the reaction on the complete system. It is recommended to investigate the influence of the cable properties (e.g. stiffness and weight) on the system and study different types of modelling the cable dynamics. Also, the tacklines in this study are modelled massless such that the influence of the cable sagging is not taken into account. Sagging of the cable is assumed to have an essential effect on the dynamic behaviour of the system in the sense of damping. This could be investigated in HAWC2 by testing the model for different cable properties.

Certain blade hoisting orientations show strong fluctuations of the root location. It is recommended to investigate the source of these fluctuations and in which modes the blade is dangling. This could be done by performing simulations for a long period of time (e.g. 5000 seconds) with constant velocity in order to determine what the frequencies of the fluctuations are and whether they damp out over time. The source of this chaotic movement might come from dynamic stall effects on the blade, however thorough research should accurately determine this by studying the angle of attack over time.

As blades become heavier and towers taller eventually there comes the need for active device control strategies and design modifications in order to counteract the large fluctua-

tions due to unsteady aerodynamics. Equivalently, with the increasing length and higher flexibility of future blades it is recommended to further study the importance of blade deformation and dynamic stall on the behaviour of the blade.

Finally, it is recommended to validate the model with actually measurements from an offshore installation. These measurements should include the wind direction and turbulence intensity over a period of time. The forces in the cable should be measured used strain gauges and the blade should be equipped with an accelerometer in order to measure the acceleration and rotation of the blade. The wind conditions and cable properties should be matched with the measurement situation such that the model can be validated. The aerodynamic and structural forces can be verified with the cable tension and the behaviour of the blade compared with the data from the accelerometers.

References

- [1] *A Dictionary Of Physics*. Oxford University Press, 6th edition, 2009.
- [2] A2SEA. Sea Installer Technical specifications, April 2013. URL <http://www.a2sea.com/fleet/sea-installer/>.
- [3] I H Abbott and A E Von Doenhoff. *Theory of Wing Sections: Including a Summary of Airfoil data*, volume 11. 1959. ISBN 0486605868. URL http://www.amazon.com/Theory-Wing-Sections-Including-Summary/dp/0486605868/ref=pd_sim_b_90.
- [4] J D Anderson. *Fundamentals of Aerodynamics*, volume 1984. 1991. ISBN 0072373350. doi: 10.1371/journal.pcbi.1000716.
- [5] Christian Bak, Frederik Zahle, Robert Bitsche, Anders Yde, Lars Christian Henriksen, Anand Nata, and Morten Hartvig Hansen. Description of the DTU 10 MW Reference Wind Turbine. Technical Report July, DTU Department of Wind Energy Report I-0092, 2013.
- [6] R. M. Barron and Ali A. Salehi Neyshabouri. Effects of under-relaxation factors on turbulent flow simulations. *International Journal for Numerical Methods in Fluids*, 42(8):923–928, July 2003. ISSN 0271-2091. doi: 10.1002/fld.563. URL <http://doi.wiley.com/10.1002/fld.563>.
- [7] Dan G. Cacuci. Second-order adjoint sensitivity analysis methodology (2nd-ASAM) for computing exactly and efficiently first- and second-order sensitivities in large-scale linear systems: I. Computational methodology. *Journal of Computational Physics*, 284:687–699, March 2015. ISSN 00219991. doi: 10.1016/j.jcp.2014.12.042. URL <http://www.sciencedirect.com/science/article/pii/S0021999114008596>.
- [8] M S Campobasso, A Zanon, M Foerster, F Fraysse, and A Bonfiglioli. CFD modelling of wind turbine airfoil aerodynamics. In *63 CONGRESSO NAZIONALE ATI ASSOCIAZIONE TERMOTECNICA ITALIANA*, pages 23–26, 2008. URL <http://eprints.gla.ac.uk/5216/>.

- [9] Tim Chartier and Anne Greenbaum. Richardson's Extrapolation, 2008. URL http://www.math.washington.edu/~greenbau/Math_498/lecture04_richardson.pdf.
- [10] Ph Devinant, T. Laverne, and J. Hureau. Experimental study of wind-turbine airfoil aerodynamics in high turbulence. *Journal of Wind Engineering and Industrial Aerodynamics*, 90:689–707, 2002. ISSN 01676105. doi: 10.1016/S0167-6105(02)00162-9.
- [11] Mark Drela. XFOIL: An Analysis and Design System for Low Reynolds Number Airfoils. In *Low Reynolds Number Aerodynamics*, pages 1–12. 1989. ISBN 978-3-540-51884-6. doi: 10.1007/978-3-642-84010-4\1.
- [12] M Gaunaa, L Bergami, S Guntur, and F Zahle. First-order aerodynamic and aeroelastic behavior of a single-blade installation setup. *Journal of Physics: Conference Series*, 524:012073, June 2014. ISSN 1742-6596. doi: 10.1088/1742-6596/524/1/012073. URL <http://stacks.iop.org/1742-6596/524/i=1/a=012073?key=crossref.c6c0b3dbe54fd00102c401add6829490>.
- [13] Sighard. F. Hoerner. *Fluid Dynamic Drag: Theoretical, Experimental and Statistical Information*. 1965. URL <http://scholar.google.com/scholar?hl=en&btnG=Search&q=intitle:Fluid-Dynamic+Drag,+Theoretical,+Experimental+and+Statistical+Information#4>.
- [14] Sighard. F. Hoerner and Henry V. Borst. *Fluid Dynamic Lift: Practical Information on Aerodynamic and Hydrodynamic Lift*. 1985. URL http://books.google.nl/books/about/Fluid_dynamic_lift.html?id=jD1HAQAAIAAJ&pgis=1.
- [15] IEC. *IEC 61400-1 Wind Turbines - Part 1: Design requirements*, volume 2005. 2005. doi: 10.1055/s-2007-985912.
- [16] Taeseong Kim, Anders M. Hansen, and Kim Branner. Development of an anisotropic beam finite element for composite wind turbine blades in multibody system. *Renewable Energy*, 59:172–183, November 2013. ISSN 09601481. doi: 10.1016/j.renene.2013.03.033. URL <http://linkinghub.elsevier.com/retrieve/pii/S0960148113001894>.
- [17] Lukas Kuijken. Optimisation of Single Blade Mounting for Wind Turbines. Technical report, Denmark Technical University & Technical University of Delft, 2014.
- [18] TJ J Larsen, HA A Madsen, GC C Larsen, and KS S Hansen. Validation of the dynamic wake meander model for loads and power production in the Egmond aan Zee wind farm. *Wind Energy*, 16(October 2012):605–624, 2013. doi: 10.1002/we. URL <http://onlinelibrary.wiley.com/doi/10.1002/we.1563/full>.
- [19] Torben Juul Larsen and Anders M Hansen. *How 2 HAWC2, the user's manual*. Risø National Laboratory, Roskilde, Denmark, 2013.
- [20] LEAP Australia & New Zealand. Computational Fluid Dynamics (CFD) Blog — Tips & Tricks: Turbulence Part 2 Wall Functions and Y+ requirements, . URL <http://www.computationalfluidynamics.com.au/tips-tricks-turbulence-wall-functions-and-y-requirements/>.

- [21] LEAP Australia & New Zealand. Computational Fluid Dynamics (CFD) Blog — Tips & Tricks: Inflation Layer Meshing in ANSYS, . URL <http://www.computationalfluidynamics.com.au/tips-tricks-inflation-layer-meshing-in-ansys/>.
- [22] Ehl Liu. Fundamental methods of numerical extrapolation with applications. *Mitopencourseware, Massachusetts Institute Of Technology*, pages 1–18, 2006. URL http://ocw.seeu.edu.mk/NR/rdonlyres/Mathematics/18-304Spring-2006/D69D4111-2100-443D-A75D-5D5BE7B4FAA2/0/xtrpltn_liu_xpnd.pdf.
- [23] Jakob Mann. Wind field simulation. *Probabilistic Engineering Mechanics*, 13(4): 269–282, October 1998. ISSN 02668920. doi: 10.1016/S0266-8920(97)00036-2. URL <http://linkinghub.elsevier.com/retrieve/pii/S0266892097000362>.
- [24] Jakob Mann. The spectral velocity tensor in moderately complex terrain. *Journal of Wind Engineering and Industrial Aerodynamics*, 88(2-3):153–169, December 2000. ISSN 01676105. doi: 10.1016/S0167-6105(00)00046-5. URL <http://www.sciencedirect.com/science/article/pii/S0167610500000465>.
- [25] National Renewable Energy Laboratory. NREL Wind Turbine Airfoil Data, 2014. URL <http://wind.nrel.gov/airfoils/Coefficients/>.
- [26] Örebro University. AASS Learning Systems Lab, 2015. URL http://www.aass.oru.se/Research/Learning/driv_dir/bMSd.html.
- [27] Justin Petrilli, Ryan Paul, Ashok Gopalarathnam, and NT T Frink. A CFD Database for Airfoils and Wings at Post-Stall Angles of Attack. *AIAA Paper*, (919), 2013. URL <http://arc.aiaa.org/doi/pdf/10.2514/6.2013-2916>.
- [28] Stephen B Pope. Turbulent flows. *Cambridge university press*, 2000.
- [29] Renew Indians Campaign. Siemens to Supply 1GW Offshore Wind Turbines to Dong, 2015. URL <http://www.renewindians.com/2013/04/siemens-to-supply-1gw-offshore-wind-Turbines-to-Dong.html>.
- [30] A Subcontract Report, C Ostowari, and D Naik. Post-Stall Wind Tunnel Data for NACA 44XX Series Airfoil Sections. Technical Report 4807, Texas A and M Univ., College Station (USA). Dept. of Aerospace Engineering, 1985.
- [31] Christopher Rumsey. Turbulence Modeling Resource, 2013. URL <http://turbmodels.larc.nasa.gov/sst.html>.
- [32] William S. Saric, Helen L. Reed, and Edward B. White. Stability and Transition of Three -Dimensional Boundary Layers. *Annual Review of Fluid Mechanics*, 35:413–440, 2003. ISSN 0066-4189. doi: 10.1146/annurev.fluid.35.101101.161045. URL <http://www.annualreviews.org/doi/abs/10.1146/annurev.fluid.35.101101.161045>.
- [33] Mohamed a. Sayed, Hamdy a. Kandil, and Ahmed Shaltot. Aerodynamic analysis of different wind-turbine-blade profiles using finite-volume method. *Energy Conversion and Management*, 64:541–550, December 2012. ISSN 01968904. doi: 10.1016/

- j.enconman.2012.05.030. URL <http://linkinghub.elsevier.com/retrieve/pii/S0196890412002634>.
- [34] Ahmed A. Shabana. *Dynamics of Multibody Systems*. Cambridge University Press., 2005. ISBN 9780521850117. URL <http://web.b.ebscohost.com/ehost/detail?sid=32dc2c9d-80be-4faa-bb70-58c4c5155707@sessionmgr112&vid=3#db=nlebk&AN=138999>.
- [35] Robert E Sheldahl and Paul C Klimas. Aerodynamic characteristics of seven symmetrical airfoil sections through 180-degree angle of attack for use in aerodynamic analysis of vertical axis wind turbines. Technical report, 1981. URL [\delimitert026E30F\\\$nhttp://www.osti.gov/energycitations/product.biblio.jsp?osti_id=6548367](http://onlinelibrary.wiley.com/doi/10.1002/cbdv.200490137/abstract).
- [36] Siemens. Siemens to build major offshore wind manufacturing site in the UK, 2015. URL http://www.siemens.co.uk/en/news_press/index/news_archive/2014/major-uk-offshore-wind-manufacturing-site-to-be-built-by-siemens.htm.
- [37] Siemens Wind Power. Inhouse Document. Technical report, 2012.
- [38] Siemens Wind Power. Inhouse Document. Technical report, 2014.
- [39] N. N. Sørensen and J. A. Michelsen. Drag Prediction for Blades at High Angle of Attack Using CFD. *Journal of Solar Energy Engineering*, 126(4):1011, 2004. ISSN 01996231. doi: 10.1115/1.1807854. URL <http://solarenergyengineering.asmedigitalcollection.asme.org/article.aspx?articleid=1457137>.
- [40] State of Green. Liftra Blade Dragon, 2015. URL <http://stateofgreen.com/en/Profiles/Liftra/Products/Blade-Dragon>.
- [41] James L Tangler. Insight into wind turbine stall and post-stall aerodynamics. *Wind Energy*, 7:247–260, 2004. ISSN 1099-1824. doi: 10.1002/we.122. URL <http://dx.doi.org/10.1002/we.122>.
- [42] The Aeronautical Research Institute of Sweden and Aerodynamics Department. Coordinates and Calculations for the FFA-W1-xxx, FFA-W2-xxx, FFA-W2-xxx and FFA-W3-xxx Series of Airfoils for Horizontal Axis Wind Turbines. Technical report, 1990.
- [43] W A Timmer. Aerodynamic characteristics of wind turbine blade airfoils at high angles-of-attack. In *TORQUE 2010: The Science of Making Torque from Wind*, pages 71–78, 2010.
- [44] Stephen P Timoshenko. On the transverse vibrations of bars of uniform cross-section. *Philosophical Magazine Series 6*, 43:125–131, 1922. ISSN 1941-5982. doi: 10.1080/14786442208633855.
- [45] A Uranga, PO Persson, M Drela, and J Peraire. Preliminary Investigation Into the Effects of Cross-Flow on Low Reynolds Number Transition. *20th AIAA Computational Fluid Dynamics Conference*, (June):1–23, 2011. URL <http://arc.aiaa.org/doi/pdf/10.2514/6.2011-3558>.

- [46] Yong Wang, Wei He, and De Tian. Calculation of hoisting forces of the wind turbine rotor based on wind conditions. *Renewable Energy*, 39(1):323–328, March 2012. ISSN 09601481. doi: 10.1016/j.renene.2011.08.045. URL <http://linkinghub.elsevier.com/retrieve/pii/S0960148111005040>.
- [47] Yong Wang, De Tian, and Wei He. Computation of Hoisting Forces on Wind Turbine Blades Using Computation Fluid Dynamics. *Applied Mechanics and Materials*, 446-447:452–457, November 2013. ISSN 1662-7482. doi: 10.4028/www.scientific.net/AMM.446-447.452. URL <http://www.scientific.net/AMM.446-447.452>.
- [48] Ji Yao, Weibin Yuan, Jianliang Wang, Jianbin Xie, Haipeng Zhou, Mingjun Peng, and Yong Sun. Numerical simulation of aerodynamic performance for two dimensional wind turbine airfoils. In *Procedia Engineering*, volume 31, pages 80–86, 2012. doi: 10.1016/j.proeng.2012.01.994.

Appendix A

HAWC2 Input Files

```

; HAWC2 Model to Simulate the Behaviour of a Lifted Wind Turbine Blade
;
; European Wind Energy Master - Rotor Design
; Lukas Kuijken 1382381 s122629
;
; Friday 9 May 2014
;
; Pitch 90 deg, Yaw 0 deg
; Model uses rigid beam elements to model the cables
;
; Planned improvements:
; - Correct cable properties
; - Correct alignment of c.g.
; - Add aerodrag to blade
; - Test dynamic stall model
;
begin simulation;
    time_stop      250; set the simulation time
    solvertype     1 ; (newmark)
    on_no_convergence continue ;
    convergence_limits 1E3 1.0 0.7 ;
    logfile ./log/w20_p90_y0_noturb.log;
    animation ./animation/w20_p90_y0_noturb.dat;
;
begin newmark;
    deltat     0.1;
end newmark;
end simulation;
;
-----
begin new_htc_structure;
;
begin main_body;
    name          craneboom ;      tip of the crane boom, fixed point
    type         timoschenko ;
    nbodies      1 ;
    node_distribution   c2_def ;
    damping_posdef  0.0 0.0 0.0 4.65E-04  4.65E-04  3.983E-03 ; high stiffness
    concentrated_mass  1.0 0.0 0.0 0.0 0.0 0.0 0.0 3.751E+06 ;
    concentrated_mass  5.0 0.0 0.0 0.0 1.0552E+05 0.0 0.0 3.257E+05 ;
    begin timoschenko_input;
        filename ./data/craneboom.dat ;
        set 1 1 ;
    end timoschenko_input;
    begin c2_def;           Definition of centerline (main_body coordinates)
        nsec 2;
        sec 1 0.0 0.0 0.0 0.0 ; x,y,z,twist
        sec 2 0.0 0.0 1.0 0.0 ;
    end c2_def ;
end main_body;
;

```

Figure A.1: Simulation and Craneboom main_body Module

```

begin main_body;
  name      cable1 ;      cable piece 1, length 30 meters
  type      timoschenko ;
  nbodies   1 ;
  node_distribution c2_def ; cable properties yet to be modelled correctly
  damping_posdef  0.0 0.0 0.0 4.65E-04  4.65E-04  3.983E-03 ;
  concentrated_mass 1.0 0.0 0.0 0.0 0.0 0.0 0.0 0.0 3.751E+06 ;
  concentrated_mass 5.0 0.0 0.0 0.0 1.0552E+05 0.0 0.0 3.257E+05 ;
  begin timoschenko_input;
    filename ./data/cable.dat ;
    set 1 1 ;
  end timoschenko_input;
  begin c2_def;           Definition of centerline (main_body coordinates)
    nsec 2;
    sec 1 0.0 0.0 0.0 0.0 ; x,y,z,twist
    sec 2 0.0 0.0 30 0.0 ;
  end c2_def ;
end main_body;
;
begin main_body;
  name      cable2 ;      cable piece 2, length 7.8 meters
  type      timoschenko ;
  nbodies   1 ;
  node_distribution c2_def ; cable properties yet to be modelled correctly
  damping_posdef 0.0 0.0 0.0 4.65E-04  4.65E-04  3.983E-03 ;
  concentrated_mass 1.0 0.0 0.0 0.0 0.0 0.0 0.0 0.0 3.751E+06 ;
  concentrated_mass 5.0 0.0 0.0 0.0 1.0552E+05 0.0 0.0 3.257E+05 ;
  begin timoschenko_input;
    filename ./data/cable.dat ;
    set 1 1 ;
  end timoschenko_input;
  begin c2_def;           Definition of centerline (main_body coordinates)
    nsec 2;
    sec 1 0.0 0.0 0.0 0.0 ; x,y,z,twist
    sec 2 0.0 0.0 7.8 0.0 ;
  end c2_def ;
end main_body;
;
begin main_body;
  name      cable3 ; cable piece 3, length 7.8 meters
  copy_main_body cable2;
end main_body;
;

```

Figure A.2: Cable 1 and 2 main_body Module

```

begin main_body;
  name      blade ;      blade 86.36 meters
  type      timoschenko ;
  nbodies   1 ;
  node_distribution c2_def; " 3% damping tuned by tkim 23/03/13 unable to fit 3rd and higher mode"
  damping_posdef  0.0 0.0 0.0 1.53e-3 2.55e-3 3.3e-4 ;
begin timoschenko_input ;
  filename ./data/blade.dat;
  set 1 1 ;           set subset
end timoschenko_input;
begin c2_def;          Definition of centerline (main_body coordinates)
  nsec 27 ;
  sec 1  0.00000E+00  7.00600E-05  4.44089E-16  -1.45000E+01 ;
  sec 2  -2.06477E-05 -1.22119E-02  3.00000E+00  -1.45000E+01 ;
  sec 3  -7.28810E-03 -2.49251E-02  6.00000E+00  -1.44851E+01 ;
  sec 4  -1.89235E-02 -2.73351E-02  7.00004E+00  -1.44610E+01 ;
  sec 5  -5.41282E-02 -2.82163E-02  8.70051E+00  -1.43388E+01 ;
  sec 6  -1.26633E-01 -2.13210E-02  1.04020E+01  -1.40201E+01 ;
  sec 7  -2.25666E-01 -1.28378E-02  1.22046E+01  -1.33904E+01 ;
  sec 8  -2.88563E-01 -7.70659E-03  1.35140E+01  -1.29371E+01 ;
  sec 9  -3.99194E-01 -4.88317E-03  1.70140E+01  -1.19445E+01 ;
  sec 10 -5.76634E-01 -1.80296E-02  1.95001E+01  -9.98243E+00 ;
  sec 11 -7.07136E-01 -5.01772E-02  2.14178E+01  -8.45147E+00 ;
  sec 12 -7.91081E-01 -9.41228E-02  2.46189E+01  -7.46417E+00 ;
  sec 13 -8.37195E-01 -1.48880E-01  2.80240E+01  -6.72916E+00 ;
  sec 14 -8.53948E-01 -2.14514E-01  3.30101E+01  -6.08842E+00 ;
  sec 15 -8.49367E-01 -2.90618E-01  3.42197E+01  -5.49322E+00 ;
  sec 16 -7.93920E-01 -4.62574E-01  4.02204E+01  -4.39222E+00 ;
  sec 17 -7.16284E-01 -6.88437E-01  4.66217E+01  -3.09315E+00 ;
  sec 18 -6.34358E-01 -9.60017E-01  5.30232E+01  -1.75629E+00 ;
  sec 19 -5.53179E-01 -1.28424E+00  5.94245E+01  -5.00650E-01 ;
  sec 20 -4.75422E-01 -1.66402E+00  6.58255E+01  6.01964E-01 ;
  sec 21 -4.03180E-01 -2.10743E+00  7.22261E+01  1.55560E+00 ;
  sec 22 -3.30085E-01 -2.65630E+00  7.90266E+01  2.51935E+00 ;
  sec 23 -3.10140E-01 -2.78882E+00  8.05267E+01  2.72950E+00 ;
  sec 24 -2.86719E-01 -2.92517E+00  8.20271E+01  2.93201E+00 ;
  sec 25 -2.55823E-01 -3.06577E+00  8.35274E+01  3.11874E+00 ;
  sec 26 -2.07891E-01 -3.20952E+00  8.50277E+01  3.28847E+00 ;
  sec 27 -8.98940E-02 -3.33685E+00  8.63655E+01  3.42796E+00 ;
end c2_def ;
end main_body;
;

```

Figure A.3: Blade main_body Module

```
begin orientation;
;
begin base;
  body  craneboom;
  inipos    0.0 0.0 0.0;      crane boom fixed to global reference frame
  body_eulerang 0.0 0.0 0.0;
end base;
;
begin relative;
  body1  craneboom last;
  body2  cable1 1;
  body2_eulerang 0.0 0.0 0;
end relative;
;
begin relative;
  body1  cable1 last;
  body2  cable2 1;
  body2_eulerang 0.0 60.0 0;   angle between cable 1 and 2: 60 deg
end relative;
;
begin relative;
  body1  cable2 last;          blade position horizontal
  body2  blade 14;            angle between cable 2 and the blade: 30 deg
  body2_eulerang 0.0 30.0 0;   zero rotation around pitch axis, thus 90 deg pitch
end relative;
;
begin relative;
  body1  cable1 last;
  body2  cable3 1;
  body2_eulerang 0.0 -60.0 0;  angle between cable 1 and 3: -60 deg
end relative;
;
end orientation;
;-----
```

Figure A.4: Orientation Module

```

begin constraint;
;
begin fix0; fixed to ground in translation and rotation
| body craneboom;
end fix0;
;
begin bearing1;
| name crane1;
body1 craneboom last; crane boom - cable 1 connection
body2 cable1 1;
bearing_vector 2 1.0 1.0 1.0; spherical joint
end bearing1;
;
begin bearing1;
| name cable1;
body1 cable1 last; cable 1 - cable 2 connection
body2 cable2 1;
bearing_vector 2 1.0 1.0 1.0; spherical joint
end bearing1;
;
begin bearing1;
| name cable2;
body1 cable1 last; cable 2 - cable 3 connection
body2 cable3 1;
bearing_vector 2 1.0 1.0 1.0; spherical joint
end bearing1;
;
begin bearing1;
| name hinge1;
body1 cable2 last; cable 2 - blade connection
body2 blade 14;
bearing_vector 2 1.0 1.0 1.0; spherical joint
end bearing1;
;
begin bearing1;
| name hinge2;
body1 cable3 last; cable 3 - blade connection
body2 blade 10;
bearing_vector 2 1.0 1.0 1.0; spherical joint
end bearing1;
;
end constraint;
;
end new_htc_structure;
;
-----
;

```

Figure A.5: Constraint Module

```

begin wind ;
  density          1.225 ;
  wsp              20 ;           mean wind speed
  tint              0.14 ;        turbulence intensity
  horizontal_input 1 ;          0=false, 1=true
  windfield_rotations 0 0.0 0.0 ; yaw, tilt, rotation
  center_pos0      0.0 0.0 -119 ; hub height
  shear_format     1 0.14 ;      0=none,1=constant,2=log,3=power,4=linear
  turb_format       0 ;          0=none, 1=mann,2=flex
  tower_shadow_method 0 ;        0=none, 1=potential flow, 2=jet
; scale_time_start 0 ;
; wind_ramp_factor 0.0 [t0] [wsp factor] 1.0 ;                     possibility to include gusts
; [gust] iec_gust [gust_type] [gust_A] [gust_phi0] [gust_t0] [gust_T] ;
;

begin mann;
  create_turb_parameters 29.4 1.0 3.9 1001 1.0;
  filename_u   ./turb/seed_1001_u.bin ; location of the turbulence files
  filename_v   ./turb/seed_1001_v.bin ;
  filename_w   ./turb/seed_1001_w.bin ;
;
  box_dim_u    8192 2.0508 ;           dimensions of the turbulence domain
  box_dim_v    32 5.6;
  box_dim_w    32 5.6;
  std_scaling  1.0 0.8 0.5 ;
end mann;
;
end wind;
;
;
;
```

Figure A.6: Wind Module

```

begin aero ;
  nblades 1;
  hub_vec blade -3 ;           rotor rotation vector
  link 1 mbdy_c2_def blade;   aerodynamic link to structural model
;
  ae_filename     ./data/DTU_10MW_RWT_ae.dat ; location of the aerodynamic layout file
  pc_filename     ./data/DTU_10MW_RWT_pc.dat ; location of the profile coefficient file
  induction_method 0 ;           0=none, 1=normal
  aerocalc_method 1 ;           0=ingen aerodynamic, 1=maw aerodynamic
  aerosections    50 ;          number of aerodynamic sections
  ae_sets         1 1 1;
  tiploss_method 0 ;           0=none, 1=prandtl
  dynstall_method 0 ;          0=none, 1=stall method,2=mhh method
end aero ;
;
;
begin output;
  filename ./res/w20_p90_y0_noturb; output file
; time 50.0 650.0 ;
  data_format hawc_binary;      data type
  buffer 1 ;
;
  general time;
  mbdy state pos blade 26 1.0 global # blade tip; ; x, y and z position of the blade tip
  mbdy state pos blade 1 1.0 global # blade root; ; x, y and z position of the blade root
  wind free_wind_hor 1 0.0 0.0 -119;             wind speed in horizontal direction
end output;
;
exit;
;
```

Figure A.7: Aero and Output Module

Appendix B

Aerodynamic Layout

1				
1	40			
0.0000E+00	5.3800E+00	1.0000E+02	1	;
2.0000E+00	5.3800E+00	1.0000E+02	1	;
4.7120E+00	5.3800E+00	9.6915E+01	1	;
5.3960E+00	5.3800E+00	9.5291E+01	1	;
6.3190E+00	5.3886E+00	9.2664E+01	1	;
7.4750E+00	5.4212E+00	8.8775E+01	1	;
8.8580E+00	5.4865E+00	8.3448E+01	1	;
1.0458E+01	5.5887E+00	7.6689E+01	1	;
1.2268E+01	5.7247E+00	6.8754E+01	1	;
1.4275E+01	5.8817E+00	6.0273E+01	1	;
1.6467E+01	6.0346E+00	5.2291E+01	1	;
1.8833E+01	6.1478E+00	4.5826E+01	1	;
2.1356E+01	6.2020E+00	4.0950E+01	1	;
2.4023E+01	6.1950E+00	3.7343E+01	1	;
2.6817E+01	6.1292E+00	3.4518E+01	1	;
2.9721E+01	6.0096E+00	3.2270E+01	1	;
3.2719E+01	5.8432E+00	3.0488E+01	1	;
3.5791E+01	5.6400E+00	2.9020E+01	1	;
3.8920E+01	5.4107E+00	2.7756E+01	1	;
4.2086E+01	5.1613E+00	2.6693E+01	1	;
4.5272E+01	4.8974E+00	2.5829E+01	1	;
4.8457E+01	4.6255E+00	2.5157E+01	1	;
5.1623E+01	4.3519E+00	2.4665E+01	1	;
5.4750E+01	4.0827E+00	2.4338E+01	1	;
5.7820E+01	3.8220E+00	2.4156E+01	1	;
6.0815E+01	3.5724E+00	2.4100E+01	1	;
6.3716E+01	3.3364E+00	2.4100E+01	1	;
6.6506E+01	3.1161E+00	2.4100E+01	1	;

6.9168E+01	2.9130E+00	2.4100E+01	1	;
7.1687E+01	2.7275E+00	2.4100E+01	1	;
7.4047E+01	2.5595E+00	2.4100E+01	1	;
7.6234E+01	2.4087E+00	2.4100E+01	1	;
7.8234E+01	2.2660E+00	2.4100E+01	1	;
8.0037E+01	2.1175E+00	2.4100E+01	1	;
8.1631E+01	1.9588E+00	2.4100E+01	1	;
8.3006E+01	1.7913E+00	2.4100E+01	1	;
8.4155E+01	1.6013E+00	2.4100E+01	1	;
8.5070E+01	1.3858E+00	2.4100E+01	1	;
8.5746E+01	1.1384E+00	2.4100E+01	1	;
8.6366E+01	8.3354E-01	2.4100E+01	1	;

Appendix C

Profile Coefficients

1 DTU 10MW RWT, DTU Wind Energy.

Data generated using EllipSys2D with free transition TI=0.1
and 3D corrected using the model by Bak et al.

6

1	105	24.10000	FFA-W3-241 (Re=12x10 ⁶)
-180.00000	0.00000	0.00000	0.00000
-175.00000	0.17360	0.01140	0.02180
-170.00000	0.34200	0.04520	0.04340
-165.00000	0.50000	0.10050	0.06470
-160.00000	0.64280	0.17550	0.08550
-155.00000	0.76600	0.26790	0.10570
-150.00000	0.86600	0.37500	0.12500
-145.00000	0.93970	0.49350	0.14340
-140.00000	0.98480	0.61970	0.16070
-135.00000	1.00000	0.75000	0.17680
-130.00000	0.98480	0.88030	0.19150
-125.00000	0.93970	1.00650	0.20480
-120.00000	0.86600	1.12500	0.21650
-115.00000	0.76600	1.23210	0.22660
-110.00000	0.64280	1.32450	0.23490
-105.00000	0.50000	1.39950	0.24150
-100.00000	0.34200	1.45480	0.24620
-95.00000	0.17360	1.48860	0.24900
-90.00000	0.00000	1.50000	0.25000
-85.00000	-0.17360	1.48860	0.24900
-80.00000	-0.34200	1.45480	0.24620
-75.00000	-0.50000	1.39950	0.24150
-70.00000	-0.64280	1.32450	0.23490
-65.00000	-0.76600	1.23210	0.22660
-60.00000	-0.86600	1.12500	0.21650

-55.00000	-0.93970	1.00650	0.20480
-50.00000	-0.98480	0.86030	0.19150
-45.00000	-1.01200	0.71200	0.17080
-40.00000	-1.03760	0.54750	0.14160
-39.00000	-1.04190	0.51650	0.13460
-38.00000	-1.04620	0.48160	0.12760
-37.00000	-1.05250	0.44870	0.11850
-36.00000	-1.05680	0.41770	0.10950
-35.00000	-1.06110	0.38480	0.10050
-34.00000	-1.06540	0.35580	0.08940
-33.00000	-1.07170	0.32890	0.08240
-32.00000	-1.07650	0.30310	0.06780
-30.00000	-1.08890	0.25600	0.05080
-28.00000	-1.09930	0.20900	0.03370
-26.00000	-1.11680	0.17560	0.02060
-24.00000	-1.12820	0.14230	0.00750
-22.00000	-1.12150	0.11830	-0.00080
-20.00000	-1.11480	0.09430	-0.00910
-18.00000	-1.09190	0.07650	-0.01230
-16.00000	-1.06910	0.05870	-0.01560
-14.00000	-1.03790	0.04540	-0.01560
-12.00000	-1.00670	0.03210	-0.01550
-10.00000	-0.84790	0.02300	-0.03180
-8.00000	-0.68920	0.01380	-0.04800
-6.00000	-0.42780	0.01180	-0.06110
-4.00000	-0.16650	0.00980	-0.07420
-2.00000	0.08630	0.00950	-0.08110
0.00000	0.33910	0.00920	-0.08800
2.00000	0.58670	0.00940	-0.09330
4.00000	0.83010	0.00990	-0.09770
6.00000	1.06560	0.01090	-0.10080
8.00000	1.29140	0.01240	-0.10260
10.00000	1.50120	0.01440	-0.10240
12.00000	1.68860	0.01730	-0.09980
14.00000	1.81030	0.02260	-0.09410
16.00000	1.81390	0.03540	-0.08740
18.00000	1.75450	0.06470	-0.08500
20.00000	1.60710	0.10350	-0.09130
22.00000	1.52570	0.14370	-0.10260
24.00000	1.44280	0.18410	-0.11400
26.00000	1.38260	0.22900	-0.12820
28.00000	1.32180	0.27380	-0.14230
30.00000	1.25830	0.32780	-0.15820
32.00000	1.19440	0.38160	-0.17390
33.00000	1.17340	0.42090	-0.17900
34.00000	1.15680	0.45040	-0.18310
35.00000	1.13790	0.48150	-0.18730

36.00000	1.12480	0.51050	-0.19140
37.00000	1.11770	0.54500	-0.19530
38.00000	1.10240	0.57370	-0.19930
39.00000	1.08910	0.59990	-0.20320
40.00000	1.07550	0.62800	-0.20710
45.00000	1.01750	0.75780	-0.21610
50.00000	0.97160	0.88200	-0.21840
55.00000	0.92680	1.01040	-0.22140
60.00000	0.86600	1.12500	-0.22550
65.00000	0.76600	1.23210	-0.23060
70.00000	0.64280	1.32450	-0.23490
75.00000	0.50000	1.39950	-0.24150
80.00000	0.34200	1.45480	-0.24620
85.00000	0.17360	1.48860	-0.24900
90.00000	0.00000	1.50000	-0.25000
95.00000	-0.17360	1.48860	-0.24900
100.00000	-0.34200	1.45480	-0.24620
105.00000	-0.50000	1.39950	-0.24150
110.00000	-0.64280	1.32450	-0.23490
115.00000	-0.76600	1.23210	-0.22660
120.00000	-0.86600	1.12500	-0.21650
125.00000	-0.93970	1.00650	-0.20480
130.00000	-0.98480	0.88030	-0.19150
135.00000	-1.00000	0.75000	-0.17680
140.00000	-0.98480	0.61970	-0.16070
145.00000	-0.93970	0.49350	-0.14340
150.00000	-0.86600	0.37500	-0.12500
155.00000	-0.76600	0.26790	-0.10570
160.00000	-0.64280	0.17550	-0.08550
165.00000	-0.50000	0.10050	-0.06470
170.00000	-0.34200	0.04520	-0.04340
175.00000	-0.17360	0.01140	-0.02180
180.00000	0.00000	0.00000	0.00000

